UNIVERSITY OF SOUTHAMPTON

FACULTY OF ENGINEERING AND PHYSICAL SCIENCES

Optoelectronics Research Centre

Spatio-Temporal Beam Tailored Fibre Lasers

by

Neda Baktash

Thesis for the degree of Doctor of Philosophy

September 2020

UNIVERSITY OF SOUTHAMPTON

ABSTRACT

FACULTY OF ENGINEERING AND PHYSICAL SCIENCES

Optoelectronics Research Centre

Doctor of Philosophy

SPATIO-TEMPORAL BEAM TAILORED FIBRE LASERS

by Neda Baktash

This thesis reports the development of an important class of next generation fibre laser system offering unprecedented levels of simultaneous control of the spatial, temporal and polarisation properties of the output beam in the nanosecond and picosecond pulse regimes. This work is predominately assigned to the EPSRC funded Energy Resilient Manufacturing (ERM) project in collaboration with the Institute for Manufacturing (IfM) of the University of Cambridge and SPI Lasers (UK) Ltd.

In the nanosecond regime, an Yb-doped fibre master oscillator power amplifier (MOPA) system with the capability of selectively generating doughnut-shaped radially and azimuthally polarised beams with user-defined temporal pulse shapes is investigated. The system is seeded by a directly modulated super-luminescent diode (SLD) using a computer controlled arbitrary waveform generator (AWG) to generate nanosecond pulses with user-defined temporal pulse shapes. Using the SLD substantially increases the robustness of the system by raising the threshold for stimulated Brillouin scattering (SBS) induced damage. The spatial mode shaping is achieved by using a nanograting spatially variant half-waveplate (S-waveplate) to convert the linearly-polarised fundamental (LP_{01}) mode from the pre-amplification stages into a doughnut-shaped radially-polarised beam prior to the power amplifier. A maximum output pulse energy of ~860 μJ was achieved for ~100 nanosecond pulses at 25 kHz repetition rate with user defined pulse shape for both radial and azimuthal polarisation states. The packed laser system was delivered to University of Cambridge for materials processing experiments to investigate its performance and capabilities.

Next, the generation of high average output power, high peak power, and high pulse energy radially polarised picosecond pulses from a compact gain-switched laser diode seeded Yb-doped fibre MOPA system was investigated. A 1030 nm Fabry-Pérot laser diode was gain-switched using a train of sinusoidal RF pulses at a repetition rate of 87.5 MHz and self-seeded to produce ~150 ps, ~4 pJ pulses at 1034.5 nm with a 3-dB spectral bandwidth of ~0.03 nm. A fibre pigtailed electro-optic modulator (EOM) used as a pulse picker and a fibre pigtailed acoustic-optic modulator (AOM), synchronised to the EOM, was used to remove inter-pulse amplified spontaneous emission (ASE) prior to second pre-amplifier stage. A ***q***-plate was employed as a mode converter prior to the final power amplifier to efficiently convert the linearly polarised Gaussian-shaped beam into a doughnut-shaped radially polarised beam. The desired vector beam was efficiently amplified yielding ~110 ps pulses with a maximum output pulse energy of 30.7 μJ and a peak power of ~280 kW at a repetition rate of 1.367 MHz. The average power was scaled up to 106 W by increasing the repetition rate to 5.468 MHz, which is

being used in materials processing trails at the University of Cambridge.

Investigation of picosecond temporal pulse shaping in a femtosecond mode-locked laser oscillator based MOPA system is carried out for 10 W average output power. A ∼23 MHz repetition rate mode-locked laser source is built and followed by a length of fibre as stretcher to implement picosecond temporal pulse shaping principle via far-field frequency-to-time mapping (FF-FTM) using a WaveShaper and then amplified up to 10W average output power. Verification of temporal pulse profiles scrutinised using a house-built cross-correlator. Then, the laser performance extended and improved by replacing the laser source with a commercial laser has smoother input spectra and higher repetition rate of 100 MHz, resulting in lower peak power through the entire MOPA system. Final novel high average power spatial and temporal beam tailored data demonstrated radially polarised beam in any desired temporal pulse shapes such as square, single, double, triple pulse peaks, and Gaussian shapes were obtained for ∼70 ps at an average power level exceeding 50 W, after repetition rate doubling. The shapes were verified by using a cross-correlator. Further power scaling was limited by the peak power increase and introduction of higher nonlinear phase shifts, producing distorted temporal profiles. These results represent the highest optical power demonstrated from a fibre MOPA for spatio-temporal beam tailoring in tens of picosecond optical pulses.

Contents

List of Figures

Declaration of authorship

I, Neda Baktash, declare that the thesis entitled **"Spatio-Temporal Beam Tailored Fibre Lasers"** and the work presented in it are my own and has been generated by me as the result of my own original research. I confirm that:

- This work was done wholly or mainly while in candidature for a research degree at this University;
- Where any part of this thesis has previously been submitted for a degree or any other qualification at this University or any other institution, this has been clearly stated;
- Where I have consulted the published work of others, this is always clearly attributed;
- Where I have quoted from the work of others, the source is always given. With the exception of such quotations, this thesis is entirely my own work;
- I have acknowledged all main sources of help;
- Where the thesis is based on work done by myself jointly with others, I have made clear exactly what was done by others and what I have contributed myself;
- Parts of this work have been published as the journal papers and conference contributions listed in List of Publications.

Signed: .....

Date: .....

To my beloved Parents, sisters, brother, nephew and niece,
Fatemeh, Rahmatollah, Sara, Maryam, Masoud,
Radvin, and Venus.

Acknowledgements

I would like to express my utmost gratitude to my supervisor, Prof. David Richardson, for taking me on board his dynamic research group, Advanced Fibre Technologies and Applications group. I am thankful to him for his endless guidance and support throughout this dissertation.

I am particularly thankful to my co-supervisor, Dr. Shaif-ul Alam for his advice and assistance in keeping my progress on track even when he was outside of ORC in the last year of study.

I am grateful from my other co-supervisor Dr. Yongmin Jung for his valuable discussion and teachings.

I would like to profoundly thanks Dr. Jonathan Price for his great guides especially in the two last years of my PhD.

My special thank to Dr. Di Lin for his great helps, guidance and patience in almost four years of working together on the project.

I am fortunate to work among the dedicated current and former group members that are always helpful and supportive. Hereby, I extend my thanks in particularly to Dr. Lin Xu, Dr. Saurabh Jain, Dr. Hans Christian Mulvad, Dr. Sijing Liang, Qiang Fu, Krzysztof Herdzik, Zhengqi Ren and Dr. Martin Berendt for their useful advices and contributions.

I wish to acknowledge the former ORC member Dr. Betty Meng Zhang for her countless helps in learning the picosecond pulse shaping algorithm and her great friendship through her presence in my office.

In addition, a thank you to Prof. Johan Nilsson, Prof. Gilberto Brambilla, Dr. Morten Ibsen and Dr. Paulo Dos Santos Almeida for their directly and indirectly help throughout these 4 years.

I would like to offer my thanks to the Optics and Photonics Society of ORC for trust in me and accepting me as the academic officer for three years.

I also wish to thank past and present colleagues at the University of Southampton for making me feel a part of a vibrant professional community.

Most importantly, not of this could have happen without my family members supports during my PhD journey.

List of Abbreviations

AOM	Accousto-Optics Modulator
ASE	Amplified Spontaneous Emission
AWG	Arbitrary Waveform Generator
BDO	Beam Deliver Optics
BPF	Bandpass Filter
BPP	Beam Parameter Product
CCD	Charge-Coupled Device
CFBG	Chirped Fibre Bragg Grating
CPA	Chirped Pulse Amplification
CSA	Communications Signal Analyzer
CVB	Cylindrical Vector Beam
CW	Continuous Wave
DC	Direct Current
DCA	Digital Communication Analyzer
DFB	Distributed Feedback laser
EDFA	Erbium Doped Fibre Amplifier
EOM	Electro-Optics Modulator
ERM	Energy Resilient Manufacturing
ESA	Excited State Absorption
EUV	Extreme Ultraviolet
FBG	Fibre Bragg Grating
FF	Far Field
FMF	Few-Mode Fibre
FROG	Frequency Resolved Optical Gating
FTM	Frequency Time Mapping
FWHM	Full Width at Half Maximum
GVD	Group Velocity Delay
HE/EH	Hybrid Modes
IR	Infrared
LCoS	Liquid Crystal on Silicon
LD	Diode Laser
LMA	Large-Mode-Area
LP	Linear Polarization Mode
M^2	Beam Quality Factor
MEMS	Microelectromechanical System
MMF	Multi Mode Fibre
MOPA	Master Oscillator Power Amplifier
NA	Numerical Aperture
ORC	Optoelectronics Research Centre

OSA	Optical Spectrum Analyser
OSNR	Optical Signal to Noise Ratio
PCB	Printed Circuit Board
PCF	Phtonics Crystal Fibre
PER	Polarization Extinction Ratio
PM-YDF	Polarized Maintenance - Ytterbium Doped Fibre
RE	Rare-Earth
RF	Radio Frequency
SESAM	Semiconductor Saturable Absorber Mirror
SBS	Stimulated Brillouin Scattering
SEM	Scanning Electron Microscope
SFG	Sum Frequency Generation
SHG	Second Harmonic Generation
SLD	Super Luminescent Diode
SLM	Spatial Light Modulator
SMF	Single Mode Fibre
SPI	Southampton Photonics Inc.
SPM	Self-Phase Modulation
SRS	Stimulated Raman Scattering
SVR	Spatially Variant Retardation plate
S-Waveplate	Space-Variant Waveplate
TBP	Time-Bandwidth Product
TE	Transverse Electric Field Mode
TEC	Thermoelectric Cooler/ Controller
TEM	Transverse Electro-Magnetic Mode
TM	Transverse Magnetic Field Mode
UPC	Ultra Physical Contact
UV	Ultraviolet
WDM	Wavelength Division Multiplexing
YDFA	Ytterbium Doped Fibre Amplifier

Chapter 1

Introduction

Overview

Advanced high power pulsed fibre laser systems have paved the way for enormous improvements in a number of laser-based application fields. In terms of performance, there is still much room for development, particularly in the optimisation of light:matter interactions and in maximising the efficiency of each pulse in materials processing. Simultaneous control of the spatial, polarisation and temporal properties of the output beam allows high quality machining procedures with low energy consumption. This thesis reports the development of nanosecond and picosecond optical pulse fibre lasers suitable for this challenging goal with spatio-temporal beam tailoring, relatively high energies, high average powers and high peak powers. This chapter gives a brief overview of high power pulsed fibre master oscillator power amplifier (MOPA) laser systems. The general motivation and a review of the fundamental science and techniques used are introduced in section 1.1. Then an outline of the thesis structure is given in section 1.2.

1.1 Review of the State of the Art and an Introduction to Technical Work Performed

The invention of the laser in 1960 revolutionized many of the technology areas including manufacturing industry, optical communications, medical field, military defense and scientific research. This extensive contribution of lasers to the modern world is due to the emission of coherent light at a very wide range of frequencies from ultraviolet to infrared regions with the possibility of high optical power in many applications[1–5]. Requirement of high laser beam output power with an increased brightness, conserving the high beam quality, is considered as an important goal in a laser i.e. "laser power scaling" research.

Several different ways have been worked on over the years to power scale laser outputs, among them power scaling by thin-disk lasers [5–9], slab lasers [10, 11] and beam combination of laser arrays [12–14]. Although these techniques have demonstrated achievement of high output powers, they generally include complex free-space configuration and require alignment maintenance.

Master oscillator power amplifier (MOPA) approach is the most efficient way of scaling output power whilst retaining specific properties of the low power seed source,

which is difficult to attain directly from a high power laser source. All fibre MOPA allows significant scaling of both the peak and average power levels [15, 16]. In Particular, ytterbium (Yb)-doped fibre amplifiers have shown that they can offer high output power (∼20 kW from a single MOPA [17] and >100 kW by spatial combination of low power laser modules in IPG Photonics [18, 19]) and excellent power conversion efficiency (∼89%, recorded by Nufern). Thereby, Yb-doped MOPA systems attracted increased interest as compared to other rare-earth dopants for power scaling [20].

Among the wide range of application areas, laser materials processing is one of the largest fields for short pulsed lasers [4, 21]. The processing quality depends on many laser beam parameters such as wavelength (λ), pulse duration (τ), beam quality factor (M^2) and pulse shape. The latter one has recently attained significant attention in laser micro-machining due to yielding increased flexibility during operation besides quality improvements with the fabrication of high precision microholes in metals without post processing [22, 23], which are critically important factors for industrial scale production [24]. Many researchers are exploring the use of different pulse shapes [25]. For example, laser ablation by double pulses with tunable temporal spacing and amplitude ratio on steel, aluminum and copper exhibited significant quality improvements in metal micro-structuring in terms of smoother surfaces, less re-cast matter, deeper ablation depth, burr height reduction, etc [26]. Reports of ablation with ultrashort laser pulses, have demonstrated that the amount of material removed and the heat-affected-zone were in direct proportion to the pulse duration and that picosecond pulses resulted in less unwanted surface damage particularly in surface treatments such as polishing [27–30].

Impacts of different pulse shapes including square, single and double peak high power temporal profiles on the micro-machining have been scrutinised through nanosecond active pulse shaping techniques [31–34] in MOPAs and resulted in high quality laser micro-machining of silicon [25, 35] and TiN coatings ablation [24, 36]. Similar improvements have been observed in laser drilling efficiency of steel by applying double pulses in comparison with the conventional single-pulse, reported in [37, 38]. These results well demonstrated the enhancement of materials processing procedures using nanosecond temporal pulse shapes that can be incorporated in new laser source designs with sub-nanosecond temporal features.

Less appearance of heat-affected-zones in picosecond laser processing due to the interaction mechanism of bulk material with such short pulses [30, 39–41] and improved ablation efficiencies by applying burst mode pulses [42–44], prompted the picosecond temporal pulse shaping as the preferred choice for high precision materials processing. However, the implementation of the pulse shaping in this pulse regime is much more difficult to achieve because the modulators used in nanosecond pulse shaping are not fast enough for direct modulation of the laser diode in picosecond pulse scale shaping. Besides, spectral bandwidth is usually very narrow in picosecond pulses for spectral-domain shaping unlike the femtosecond pulse shaping, so the ability to use dispersion is limited. Fixed pulse shaping of spectrally narrow picosecond pulses has been demonstrated by applying superstructured fibre Bragg gratings for rectangular pulse generation [45], long-period fibre grating devices for optical pulse shaping, particularly flat-top pulse shapes [46], using the concept of temporal coherence synthesis for efficient optical pulse re-shaper [47], spatially patterned amplitude and phase masks for Fourier spectrum modification [48, 49]. However, each of them faced

limitations imposed by narrow available bandwidth and spectral resolution since the pulse shaping of short pulses in the picosecond range requires fine adjustment of the phase and amplitude of the optical signal with high spectral resolution. Requirements of specified new designed masks for each desired pulse shape and above all, the major hindrance of having no potential for arbitrary waveform generations presents the necessity for new pulse shaping techniques such as the closed-loop controlling algorithm reported in [50] using a dispersive Fourier transform based technique to generate arbitrary complex temporal profiles in a Yb-fibre MOPA with ∼10 W average power.

Besides temporal pulse shaping, the vector nature of laser beams have been exploited in numerous applications as well. Radially and azimuthally polarised beams, having cylindrical symmetry in polarisation state, are two particular examples, which have provided some interesting performance improvements in laser:matter interactions. Due to cylindrically symmetric polarisation states the material surface is processed with the same spatially and temporally invariant polarisation state, independent of process movement. In addition, the doughnut-shaped intensity profile has a steeper intensity gradient leading to a more flat-top like distribution compared with traditional Gaussian-shaped beams [22, 51–53]. Since the vector TM_{01} and TE_{01} modes in circular core fibres have radial and azimuthal polarisation states respectively, it is possible to generate these unique beams from a fibre MOPA system whilst maintaining the capability of controlling the temporal pulse shape and hence to potentially enable improved materials processing.

In that regard, my supervisor was awarded an EPSRC funded project known as Energy Resilient Manufacturing (ERM) seeking a ten-fold increase in the energy efficiency and speed of laser based manufacturing by exploiting a new generation of fibre laser offering unprecedented levels of simultaneous control of the spatial, temporal and polarisation properties of the output beam in both nanosecond and picosecond pulse regimes with an expectation of increasing precision in micro-machining. This was a joint project combining laser development at the Optoelectronics Research Centre (ORC) with processing trials at the Institute for Manufacturing (IfM) of the University of Cambridge and SPI Lasers (UK) Ltd. providing guidance as and when necessary.

I was principally involved in this project supported by Dr. Di Lin to investigate the design and implementation of Yb-doped fibre (YDF) MOPA systems for efficient generation of high-energy radially and azimuthally polarised temporally shaped nanosecond and picosecond pulses. For the first time to the best of our knowledge, an Yb-doped fibre MOPA system seeded by a directly modulated super-luminescent diode (SLD) was built to generate 100 ns pulses with user-defined temporal pulse profiles at 25 kHz repetition rate. The spatial mode shaping is achieved by using an S-waveplate to convert the linearly-polarised fundamental (LP_{01}) mode from the pre-amplification stages into a doughnut-shaped radially-polarised beam prior to the power amplifier. In the next step, a picosecond spatial and temporal pulse shaped laser system was developed using a mode-locked seed laser in a MOPA system with an average power level beyond 50 W. Finally, the highest reported average output power above 100 W was demonstrated for radially polarised beam generation in a picosecond Yb-doped fibre MOPA system. These accomplishments with such exquisite control of the beam parameters at high peak and average powers offer the potential to be disruptive in industrial and any relevant materials processing applications. The compact, stable and simpler laser configurations were all created using commercial off-the-shelf components.

1.2 Structure of the Thesis

A review of the state-of-the-art of laser materials processing is presented in Chapter 2. It inlcudes the latest market status regarding some main laser parameters of the applied laser technologies such as beam quality, pulse duration and polarisation.

Chapter 3 introduces the relevant background information on principles of lasers and optical fibre technology with the emphasis on Yb-doped fibre amplifiers. An overview of master oscillator power amplifier (MOPA) system is described and the concept of spatio-temporal pulse shaping is introduced. Temporal pulse shaping parameters and techniques are explained. Transverse modes in fibre waveguides are discussed with techniques of exciting doughnut-shaped beams at the output of amplifier stage. The spatially variant half waveplate and quarter waveplate fabricated via the femtosecond writing technique as well as the idea of liquid crystal based *q*-plate are described afterwards.

The focus of Chapter 4 is on high power generation of doughnut-shaped beams with radial and azimuthal polarisation in Yb-doped fibre lasers in nanosecond pulse regime. Full temporal and spectral analysis of the implemented MOPA setup are described. Using a polarisation converter in an Yb-doped fibre laser system for efficient excitation of doughnut-shaped TM_{01} mode with radial polarisation and TE_{01} mode with azimuthal polarisation are presented. Finally, the overall performance of this fibre laser system for materials processing is demonstrated via a collaboration with our project partner, University of Cambridge.

Picosecond pulse generation through self-seeded gain-switched laser diode is the topic of the Chapter 5. Experimental setup and performance of the developed MOPA system are presented. Spatial beam shaping of the picosecond laser pulses are demonstrated via a *q*-plate exciting doughnut-shaped beam in the active fibre resulting in a high average power beyond 100 W for radially polarised output beam.

Investigation of picosecond temporal pulse shaping in a mode-locked laser oscillator based MOPA system including the full details of the setup for an average power below 10 W are explained in Chapter 6. Limitations of temporal pulse shaping in further power scaling attempts and improvements incorporated in a more refined experimental results are explained.

Final novel high average power spatial and temporal beam tailored data by taking the advantage of using a laser source with smoother spectra are described in Chapter 7. Demonstration of radially polarised beam in any desired temporal pulse shapes such as square, single, double and triple pulse peaks, Gaussian shapes at an average power level exceeding 50 W with the shape verifications using a cross-correlator alongside the reasons limiting the temporal pulse shaping at any further increase of power are discussed subsequently.

Chapter 8 provides a brief summary. Future prospects in order to continue the project with improvements are also summarised in second section of the chapter focusing mainly on ways to satisfy the user demand for temporal and spatial shaped pulses in the picosecond pulse regime.

Chapter 2

Review of Laser Materials Processing

A review of the state-of-the-art of laser materials processing, including the latest market status with respect to average output power, beam quality, pulse width and polarisation properties are discussed in this chapter.

2.1 Laser Materials Processing Market

Since the inception of laser in early sixties, it has found diverse applications ranging from pure scientific purposes in laboratories to the most sophisticated commercial ones in manufacturing operations, materials processing in engineering applications, metrology, biomedical technology, spectroscopy and more [2,21]. The high precision and excellent finish quality of laser materials processing and their extensive use in the automotive, aerospace, medical, military, electronics, semiconductor and even jewelry industries resulted in an intensive research in this field compare to other competing technologies and turned out to be the second largest segment in laser applications, after communications [4,28,54,55].

According to laser market data from Optech Consulting (`www.optech-consulting.com`), the global market for laser systems for materials processing reached a value of $\sim$ \$20 billion ($\sim$ £16 billion) at the end of 2018, showing more than two times growth in industrial laser systems market in almost 10 years. Similar market volume is estimated for 2020 based on the data from the first three quarters of 2019 (Figure 2.1 with 9% down in comparison to 2018). Among the laser systems by applications, high power processing (>1 kW) has the highest market capitalisation (45% reported in 2017 global market).

Diode lasers, carbon-dioxide (CO2) lasers, excimer lasers, bulk solid-state lasers and fibre lasers are the common high power laser sources, which are in use for materials processing around the world [4, 56–58] with increasing reported market segments in 2017, respectively (Figure 2.2 (a)). However, the industrial laser revenues has been significantly reduced for most of the laser technologies, except fibre lasers, which will set to continue in 2020. There is a huge competition between research institutes and laser system producers to improve the parameters of different laser types, particularly those intended for laser materials processing applications. Recent published reports highlights that the fibre laser sources has experienced the largest rate of growth in

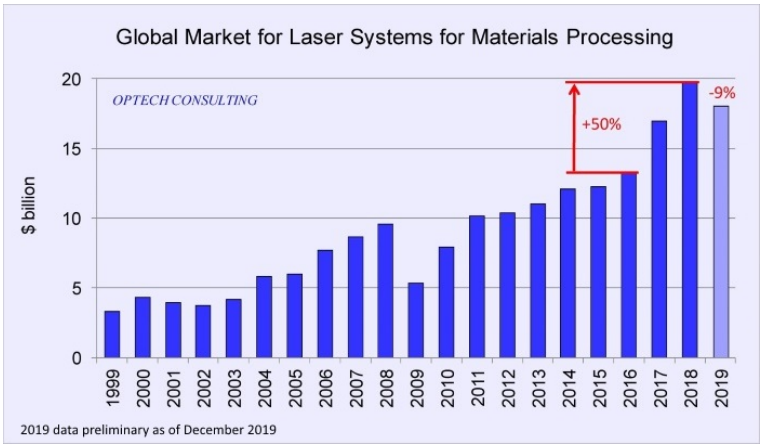

Figure 2.1: Global market for laser system for materials processing up to 2019 (`www.optech-consulting.com`).

demand with about half of the total industrial laser revenues in 2019 (Figure 2.2 (b)). The high flexibility, compactness, powerful output, high beam quality, cost-effectiveness and ultimate precision are some of the main advantages raised the interest of the market demand for fibre laser technologies. Fibre lasers hold the market share in variety of application areas, including materials processing, instrumentation, measurement and sensing, medical therapy, defense, and basic research. The pie diagram of world market for fibre lasers in Figure 2.2 (c) illustrates how the major part of the market share has been dedicated to the materials processing application from the steep increase of total market from $520 million in 2011 to $2,2 billion in 2017 with an estimate of $4,4 billion in 2025.

Referring to the latest annual market review at the beginning of 2020 (`www.industrial-lasers.com`), high power laser metal cutting in association with fibre laser revenues, has been the majority of the industrial laser revenues in 2019 of about 42%. Introduction of fibre lasers with the capability of producing some tens of kilowatt output powers and their flexibility in the work environment, has promoted the laser welding and brazing to the second in number of units sales in laser processing systems. Laser marking/engraving, precision-drilling and metal surfacing sectors with the aid of new generation of cost-effective ultrashort laser pulses are respectively the other dominant revenue segments as reported in 2019 and projected for 2020.

2.2 Laser Parameters for Materials Processing

Laser beam diameter, beam interaction time at the workpiece (pulse duration in the pulsed lasers), optical beam quality, wavelength, power distribution or mode, and polarisation are some of the other key properties apart from laser power to determine which laser technology can be selected for a given laser process, e.g. welding, cutting, drilling or polishing. Type of beam delivery, reliability, level of maintenance and safety requirements, and installation cost are the additional dominant parameters [2,4,21,56,59–61]. The effect of some the main laser properties for different type of laser technologies are explained in the following.

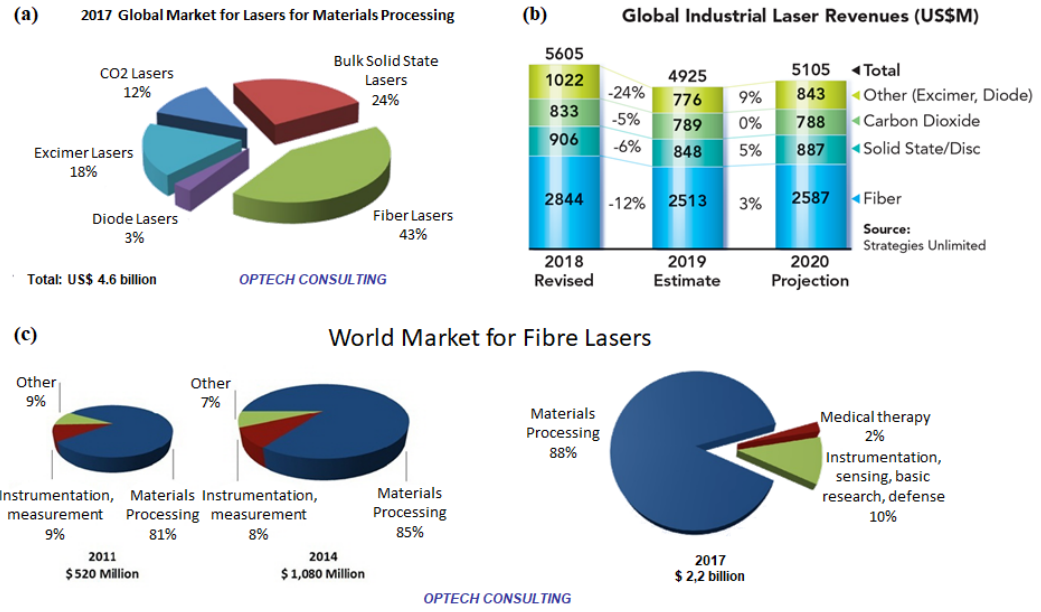

Figure 2.2: a) Global market of lasers for materials processing, b) industrial laser revenues by laser type (US$M) (`www.industrial-lasers.com`) c) world market for fibre lasers in 2011, 2014 and 2017 (`www.optech-consulting.com`).

2.2.1 Beam Quality Factor of Different Laser Types

The beam parameter product (BPP) and laser beam quality factor (M^2=BPP.π/λ) are the most popular ways to describe how a laser beam is close to "perfect-Gaussian" shape, $M^2 \geq 1$. This factor is equal to 1 for a diffraction-limited Gaussian-shaped beam profile. A high beam quality (M^2 closer to 1) is important since it defines not only the depth of focus but how tight a laser beam can be focused, which reduces the beam diameter on beam-handling optics and thus provide the possibility of using cheaper optical elements, like mirrors and lenses. Usually a high laser beam quality is required in various laser materials processing applications such as printing, marking, cutting, remote welding and drilling, which results in higher intensities in the stronger focused beam. Nevertheless, larger spot sizes are preferable in some other applications, for instance in the welding or some kinds of surface treatment areas, where higher laser output powers can be applied with comparatively lower beam qualities. However, it is essential to consider that the significant degradation of the beam quality factor, from diffraction-limited value, is one of the technical challenges to consider as many laser systems can generate higher average output powers beyond a few hundred watts [2, 4, 62].

2.2.1.1 CO2 Lasers

A wide range of average output power, from some watts to multi-kilowatt can be produced by CO2 lasers, operating at 9-11 μm wavelength range with the maximum reported power of 40 kW for pulsed CO2 laser developed by Trumpf for new extreme ultraviolet (EUV)-lithography generation (`https://www.laserfocusworld.com`). Due to the good beam absorption, the lower power laser are applied in cutting non-metallic materials, while the multi-kilowatt versions are often used for cutting, welding and laser marking of metal sheets. However, CO2 lasers are in competition with fibre lasers and bulk solid-state lasers (thin-disk lasers [5,63,64]), operating in 1 μm wavelength regime, even though these

lasers are still not able to provide high beam quality at higher average output powers to work with thick metal workpieces [65]. Therefore, CO2 lasers continue to occupy a large market share because of the relatively lower running and installation cost as well as less safety requirements even though it suffers from lack of flexible beam deliver options [2, 4, 21, 56, 57, 66]. Demonstration of remote welding systems, based on CO2 slab laser at a very high beam quality of $M^2 \approx 1.1$ with an average output power up to 6 kW, and optimised beam shape to reduce the welding penetration and increase of the weld width is reported in [67]. It is worth mentioning that CO2 lasers provide the possibility of CW and pulsed operations [68,69]. However, these lasers are typically applied in CW operational mode, even though they are excited by an RF source and are not exactly CW CO2 lasers [70].

2.2.1.2 Diode Lasers

The low beam quality of the high power diode lasers for many years was limiting their application into laser welding, soldering and brazing, cladding and heat treatment despite generation of kilowatt average output power levels. However, with technology advancements, companies can now offer more than 4 kW high power diode lasers operating at much better beam quality factors (<20 or BPP of ~5 mm mrad) [71, 72]. Therefore, it enables the users to focus laser light to a small point, which evolves the direct diode lasers as a tool for more processing applications where relatively high precision and deep penetration are not required. In that sense, diode lasers are now in competition with fibre lasers for power levels below 1 kW by offering a comparatively simple, compact, cost-effective and energy-efficient solution (fibre lasers are pumped via diode lasers or diode bars), besides the feasibility of beam transmission through optical fibres and their very long life time [4,56].

It is known that both optical energy absorption by materials and the ability of beam focusing are wavelength dependent. In that respect, particularly, the new kilowatt generation of blue diode lasers, launched by Laserline [73], can take the advantage of good laser beam absorption rate by metals in comparison to 1 micron infrared radiation by most industrial laser systems such as fibre laser technologies. Therefore, they are capable to be used to cut, weld or foil joining the metals with faster speed since more energy is converted to heat [74]. [65] is reported a comparison of direct diode lasers performance with conventional fibre and CO2 technologies for carrying out industrial laser cutting of steel and aluminium samples where they have observed acceptable cutting quality at industrially relevant cutting speeds for a 2 kW diode laser source.

2.2.1.3 Solid-State Lasers

As it has been illustrated in Figure 2.2 (b), solid-state lasers, including the disk lasers, experienced market share declines in recent years, similar to CO2 lasers. However, the latest trends in kW-class disk laser technologies with fundamental mode beam quality (M^2 factor very close to 1) show that these diode-pumped solid-state lasers may in future overshadow the market share of other high power solid-state lasers such as slab lasers [10,75] and fibre lasers [16,76] in many industrial materials processing applications [5,58, 63,64,77,78]. The laser systems operating based on the disk/ thin-disk laser technologies [6,7,79] have demonstrated high average output powers (more than 1 kW), providing pulse energies of 200 mJ at less than 10 kHz repetition rates in ultrashort picosecond pulse duration, while the beam quality factor is not so far from the diffraction-limited value

[5, 64, 77, 78]. A comparison of pulse energy of representative state-of-the-art of ultrafast thin-disk, slab and fibre laser systems at different repetition rates is been illustrated in Figure 2.3 in the perspective of average output power levels from below 10 W to more than 1 kW. It can be observed that fibre and thin-disk lasers are in a relatively close competition to obtain higher pulse energies far better than slab lasers.

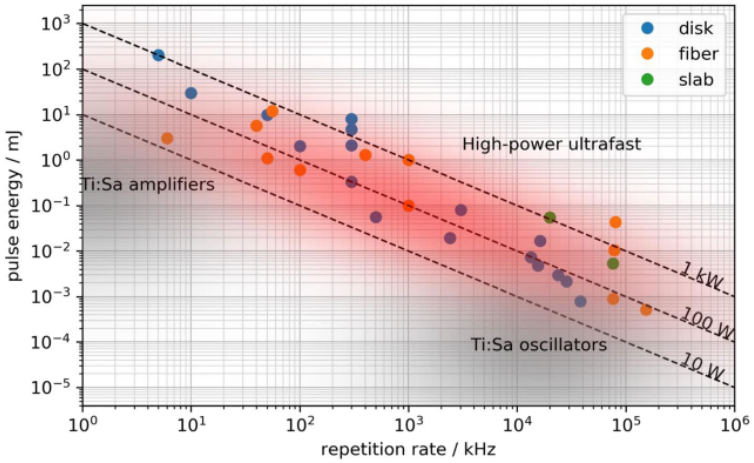

Figure 2.3: Comparison of pulse energy of representative state-of-the-art of ultrafast thin-disk, slab and fibre laser systems at different repetition rates in both amplifier and oscillator geometries [5].

Also, it has been demonstrated that higher fibre-deliverable average output powers up to 32 kW (consisting of two 16 kW Trumpf laser units) are achievable by coupling more disks in a common resonator, offering good beam quality and power efficiency [63].

2.2.1.4 Fibre Lasers

The association of high average power fibre lasers with very high beam qualities since their first commercialaisation in 90's has made and still makes a remarkable impact on a wide range of applications including industry, defense and academia [15, 16, 76]. The average output power of the fibre lasers has shown a very rapid increase in the last decade with the demand of the heavy industrial applications that need higher level of output powers. Based on the recent investigations, a highest CW average output power of 101.3 kW at 1070 nm wavelength range (BPP≈20 mm mrad) has been achieved by IPG Photonics [18, 19] by spatially combining a number of low power (2-5 kW) laser modules.

The unique properties of excellent heat dissipation, high beam quality and the possibility to build monolithic, alignment free, high power ultrafast fibre laser sources in many respect outperform the conventional laser technologies including disc and CO2 lasers [54]. Besides, the typical smaller size and lighter weigh, fibre lasers are often more rugged and capable of working in variable environments at a lower cost of ownership make them ideal candidate in demanding industries.

The high performance of short-pulse laser systems have already provided wider range of interaction parameters to chose from and enhance the materials processing outcomes, particularly in terms of miniaturisation of the components and devices with

finer structures [54]. In that regard, fibre lasers have been used widely alongside some of solid-state lasers and have proven how successfully they can be applied to improve the laser micro-machining qualities [24,28,35,36,80–83]. However, the world is still pushing for the development of ultrafast fibre lasers operating at high repetition rate, high beam quality, high average power. For instance, a recent achievement of an ultrafast fibre laser system delivering 10.4 kW average output power at an 80 MHz repetition rate and high beam quality of $M^2 \leq 1.2$ is been reported [84]. A brief review of the laser pulse duration as another vital laser property for the pulsed version of discussed fibre and solid-state laser types, is elucidated in the next section.

It is worth mentioning that although excimer lasers offer the highest peak power with ultrashort ultraviolet pulses, their high installation and maintenance costs make them less appealing as a contender. However, because of the good beam absorption for both metallic and non-metallic materials and possibility of cold machining, they are still in use for micro-machining, surface cleaning and ablation [4,56].

2.2.2 Pulse Duration

Pulse duration or in other word the laser:matter interaction time is one important parameter of the pulsed lasers. It determines when the dissipation of absorbed laser energy by the bulk material occurs and the rate of material removal during laser ablation [2,29,41]. In general, it is categorised as long pulses (ms, μs), short pulses (ns), and ultrashort pulses (ps, fs). There are large differences between materials ablation with long pulse duration in nanosecond regime and ultrashort with picosecond or femtosecond duration are shown in Figure 2.4.

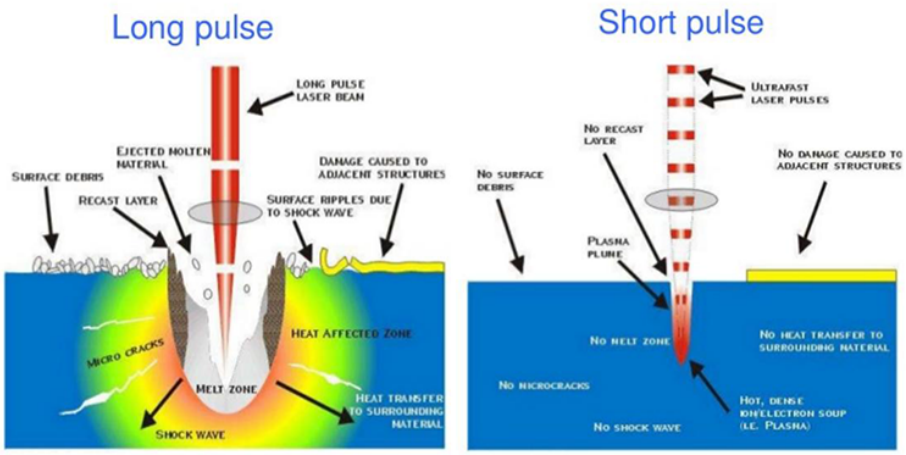

Figure 2.4: Long-pulse and ultrafast-pulse laser interaction with target material [29, 41].

More heat-affected-zones and shock waves appear in long pulse lasers in comparison to the ablation with shorter lasers due to the variety of interaction mechanisims a bulk material undergoes, before the production of the final outcome (Figure 2.5). Hence, it is critical to select/design a laser such that the output characteristics of it match with the dynamics of the materials response [21,30,40,54].

After the incident of the laser pulse, the pulse energy absorbs into the material and afterwards thermalisation process within the electronic subsystemis starts within

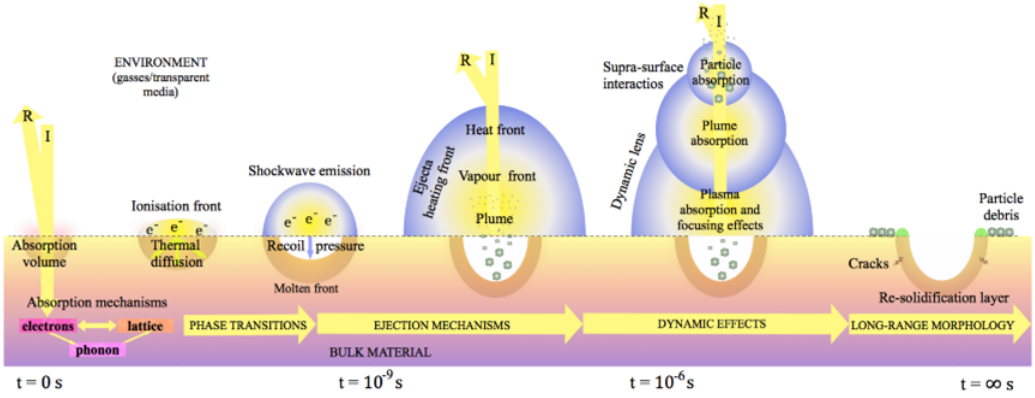

Figure 2.5: Material response mechanisms during laser processing as a function of laser pulse duration [30, 40].

femtosecond (10^{-15}s) time scales. Then, energy exchange process of electrons-lattice (or the ions) takes several picosecond to tens of picosecond, depending on the material properties such as reflectivity and absorptivity and the experimental conditions. Laser ablation process may start soon after the energy deposition, in material ejection via vaporisation in just few hundred picoseconds after pulse impact or be delayed for melt ejection from the bulk, and lasts up to some microsecond regime. The domination of thermal and structural changes and their effects in the nanosecond regime can continue up to some microseconds, which can often include the subsequent pulses, depending on the repetition rate of the laser. In consequence, some dynamic effects, affect on the final morphology of the processing zone, emerging subsequently. The common defects of heat-affected-zones, dross and recast appear, because of temperature gradients within the bulk material by heat diffusion, causing vaporisation or melting of different material fractions [21, 24, 30, 36, 40, 41, 54, 85].

In that regard, the micro-machining using ultrashort pulses take the advantage of sufficiently short interaction time of the material and the incident of the laser pulse to prevent electron-lattice coupling [24, 39, 85]. Therefore, they have attracted much interest in recent years by providing precise, fast, contactless and practically melting free processing of nearly all kind of materials, meeting the expected machining quality requirements of industrial and academical demands in high extent [2, 24, 54].

Femtosecond fibre lasers have been used to optimise the fabrication protocol for obtaining silver nanostructures on glass for surface enhanced Raman spectroscopy [86], high speed ablation-cooled material removal [87] or trends for miniaturised electronic goods [54, 88]. Commercial solid-state femtosecond laser sources, mainly based on Ti:sapphire active medium, have demonstrated their application in surface structuring of silica [42], micro-structuring with smoother surface and better roughness of steel, aluminum and copper [26] as well as silicon polishing [29] and more [27]. These lasers have also helped to study the influence of pretreatment of surface modification of dental hard tissues [89].

Picosecond laser sources have also played an important role in various materials processing applications such as polishing [28], laser ablation of steel [82], and processing of advanced electronics and semiconductor manufacturing materials [81] using high

power fibre lasers [80, 90]. The picosecond laser sources based on disc technology have also been used to fabricate enclosed 3D micro-structures in glass for glass-based microfluidic prototyping via rapid laser micro-machining and micro-welding processes [91–93]. The breakthrough micro-welding of highly dissimilar materials, like glass and metals together, using ultrashort picosecond range solid-state laser was one of the most recent reported application in materials processing field [94–97]. Nanoparticle production in ice water [98], and high speed mimicking of bio-inspired functional surfaces [99] by picosecond solid-state laser ablation are the other investigations in that area.

Although the final processed zone is usually suffering from surface defects by applying nanosecond laser machining, the high power nanosecond laser systems running at high repetition rates are in wide use in industries to gain faster machining. For instance, [100] reported a comparative investigation of laser surface hardening using pulsed lasers with ms, ns, ps and fs pulse duration and CW laser, where longer pulse lasers in ns and ms could result in effective surface modification and improving micro-hardness rather than expensive high power ultrashort lasers. Moreover, the recent growth in tunable temporal pulse shaping methods, enabling efficient extraction of stored energy of nanosecond lasers [31–34, 101], has made these lasers more attractive for different materials processing applications [24, 25, 35–38, 55].

It is worth mentioning that even though femtosecond laser pulses have demonstrated high quality hole drilling and thermal damage-free ablation, their processing speed is low (usually less than 1 MHz), which limits their industrial applications. Furthermore, applying more powerful lasers to speed up the ablation process, results in heat accumulation and plasma/particle shielding effects, while they are not present in lower pulse repetition rates [39, 42, 43, 54]. To overcome these restrictions, ultrafast successions (bursts) of laser pulses applied to ablate the target material in a timing scale before the residual thermal effects of the previous pulses emerging unwanted surface effects on the processing zone. Hence, a so-called ablation cooling at very high repetition rates will be possible, which increases the efficiency of the material removal process by concentrating the total energy of the pulses in groups of micro-pulses with moderate peak power than in a relatively longer single pulse [39, 42–44, 87].

The application of burst modes has been proven in surface structuring of silica [42], removal of brain tissue and dentine without any thermal damage to the bulk [43], and copper milling ablation [44]. Improvement of ablation efficiency by implementing burst modes in laser materials processing and the almost cold material removal effect of picosecond lasers with minimum heat-affected-zones [39], has attracted the laser designers to work on picosecond temporal pulse shaping techniques to benefit the high precision laser materials processing with more cost-effective lasers.

2.2.3 Polarisation

Developments in high power laser sources creates new options to optimise different laser materials processes. Optimisation of parameters such as wavelength, polarisation and beams shape can significantly increase process efficiency [60]. Therefore, cylindrical vector beams with radial and azimuthal (tangential) polarisation states have been used in variety of materials processing applications, including cutting, microhole drilling and

welding with [53]. The main advantage of these cylindrically symmetric polarisation states is that they process the material surface with spatially and temporally invariant polarisation state, independent of process movement. Furthermore, the doughnut-shaped intensity profile of cylindrically polarised beams, has a steeper intensity slope in comparison to Gaussian beam distributions and thereby has a more flat-top like distribution, well suited for materials processing [53].

In laser material processing, structures such as cutting kerf, microhole or an ablated surface created as the targeted material absorbs the energy of the incident laser beam. A typical laser-material interaction geometry is sketched in Figure 2.6(a).The polarisation of the beam parallel with the plane of interaction and the orthogonal one, are called p-polarisation, and s-polarisation, respectively. The incident angle is the angle between the beam propagation direction and the surface normal, which in Figure 2.6(a) is very close to 90°. An example of absorptivity calculation coefficient as a function of the incident angle for both p and s-polarisation based on the Fresnel law is shown in Figure 2.6(b). It can be seen that the p-polarisation has a significantly greater absorption coefficient than s-polarisation at incident angles exceeding 80°, which means p-polarisation state dominantly maximises the processing speed. Calculation of the beam polarisation influence on laser cutting efficiency has depicted that in case of radially polarised beam, this efficiency increases by 1.5-2 larger magnitude compared with the application of plane p-polarised and circularly polarised beams [51]. It has been experimentally verified by a CO2 laser with radial polarised beam to cut a 2 mm thick stainless steel sheet at IFSW institute and an increase of 40% in cutting velocity was measured due to the increased absorption coefficient at the cutting channel [53].

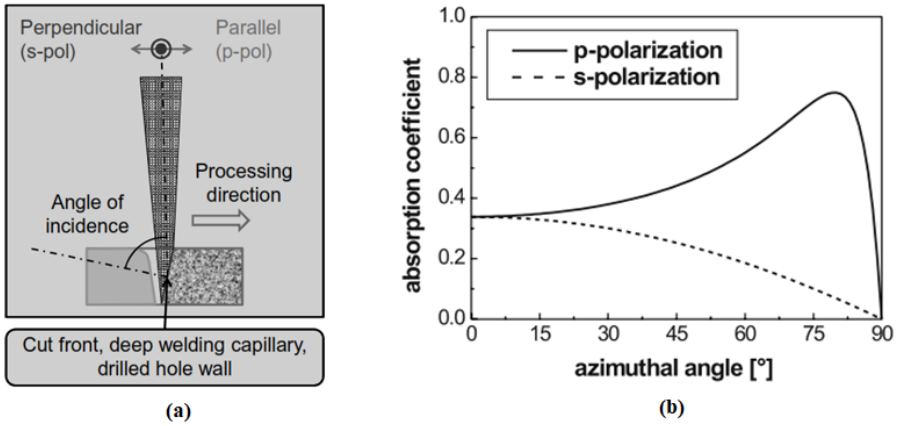

Figure 2.6: a) Schematic of a typical laser-material interaction geometry [53], b) calculated absorption coefficient of for p-polarised and s-polarised beams for mild steel [22].

Figure 2.7 shows transverse sections of drilling two microholes with nanosecond and picosecond radially and azimuthally polarised radiation on 1 mm thickness steel sheet [22,52]. The results show that depending on the optical properties of the metal, either radially or azimuthally polarised beam have the best efficiency. Moreover, it has been investigated that radial polarisation is suitable rather for the fabrication of boreholes with relatively large diameters in thin sheets with thickness less than 500 μm, while azimuthal polarisation can be used for drilling holes with high aspect ratios in thick sheets >1 mm or extraordinarily small holes with diameter less than 50 μm [53].

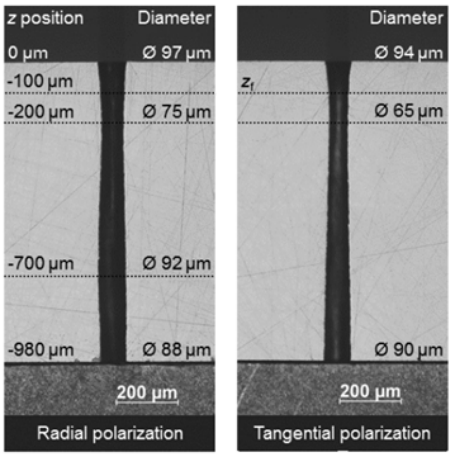

Figure 2.7: Transverse sections of microholes in 1 mm CrNi steel, drilled with radially (left) and azimuthally (right) polarised radiation [22, 53].

Also, the investigation of deep welding with high power densities showed a significant reduction of spattering (below 40%) for azimuthal polarisation at low welding speeds compared to welding with random polarisation [53]. In conclusion, the potential of improvements in process efficiency and quality for laser materials processing with cylindrical-polarised beams is leading their applications more in research and industry.

2.3 Conclusion

A brief review of the laser technologies applied in laser materials processing, including the various laser parameters and their relative market share is presented in this chapter. It has been shown that in recent years fibre lasers have taken over the market share from other high power laser systems with more than 50% of the annual total industrial laser revenues, particularly in laser materials processing applications. This upward trend of market demand stimulated many fibre laser manufacturers and research institutes to focus on new generation of fiberised laser systems in an attempt to increase market share even further. Therefore, this thesis focuses on the improvements in materials processing through simultaneous control of the spatial, temporal and polarisation properties of the output beam of a fibre MOPA system to ten-fold increase in the energy efficiency with an expectation of increasing precision in micro-machining.

Chapter 3

Fundamentals

Overview

The principles and characteristics of Ytterbium-doped fibre as well as spatial and temporal pulse shaping are presented in this chapter. Rare-earth doped fibre technology with the focus on Ytterbium-doped fibre amplifiers and lasers are presented in the first section. Developments in fibre technologies that enabled the power scaling of fibre devices are briefly discussed in the next part along with the master oscillator power amplifier (MOPA) configuration extensively used in this thesis. Nonlinearities and other detrimental effects occurring in high power fibre devices are explained in section 3. Finally, the concepts of spatial and temporal pulse shaping are discussed and the available methods for doing this are reviewed.

3.1 Ytterbium Doped Fibre Amplifiers

In the early 1960s, use of rare-earth (RE) ions as dopants in various host media gained interest and very soon these ions were embedded in glass fibres and the first experimental demonstrations of rare-earth-doped fibre laser and amplifier was reported in [102]. Among various rare-earth ions, Ytterbium (Yb^{3+}) is one of the most versatile laser media when embedded in a silica-based host [103]. It provides several very attractive features, particularly an unusually broad absorption band and emission band (Figure 3.1). Absorption band stretches from below 850 nm to above 1070 nm associated with the $^2F_{7/2} \rightarrow {}^2F_{5/2}$ transition. The broad emission bandwidth make Yb-doped fibre amplifiers ideal for the amplification of ultra-short pulses [20]. The Yb-doped fibre laser and amplifier also moved to a new stage when appropriate high power semiconductor pump diodes become available to exponentially grow the output power of the systems.

The energy level structure of the Yb^{3+}ion is simple compared to other rare-earth ions, consisting of only two relevant manifolds: the ground state $^2F_{7/2}$ (with 4 Stark levels) and a metastable state $^2F_{5/2}$ spaced by approximately 10000 cm^{-1}. The radiative lifetime of the $^2F_{5/2}$ state is typically in the range 700-1400 μs, depending on the host. The transitions between sub-levels are not fully resolved for Yb^{3+}ions in a glass at room temperature due to strong homogeneous broadening although weaker inhomogeneous broadening is also observed as the emission spectra vary to some extent with pump wavelength. The cross sections of Yb-doped germanosilicate fibres is shown in Figure 3.1. A higher content of germanium tends to decrease the lifetime of the

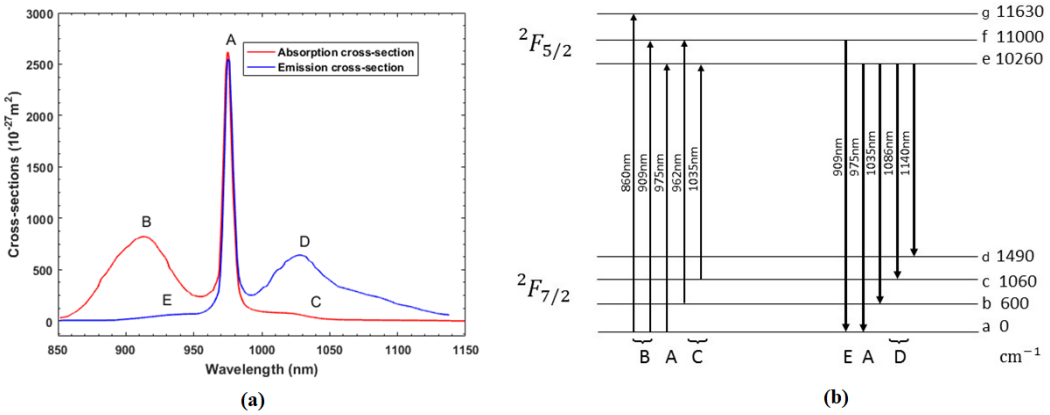

Figure 3.1: a) Ground-state absorption spectrum (red line), emission spectrum (blue line) and b) energy level diagram of Yb^{3+} in silica [20, 103].

excited state. The value of the lifetime is important for tens of kHz repetition rate MOPA system as it directly influences the level of amplified spontaneous emission (ASE).

Yb-doped silica fibres can offer high output power and excellent power conversion efficiency (besides their broad-gain bandwidth). The absence of higher energy levels greatly reduces the effect of excited state absorption (ESA). Hence, Yb-doped fibre lasers have been demonstrated to be the best choice in the 1 μm wavelength range for power scaling. Multi-kW have been reported and with fibre lengths of 1-20 meters rather than 50 to 100 meters applied for Er-fibres [15, 20].

3.2 Power Scaling in Yb Fibre Lasers

Though the use of single-cladding fibre devices one can achieve a very high gain, however, the maximum output power is limited due to the power available from single-mode pump sources. High power pump sources typically have a multimode output and hence cannot be used effectively to pump single-cladding fibres. Therefore, various alternative fibre designs and architectures were investigated, enabling power-scaling [15]. Double-clad and large-mode-area fibres are discussed in the following subsections.

3.2.1 Double-clad Fibres

Beam quality is an important parameter in fibre laser and in order to maintain that, the core of the active fibre has to be single mode. Pumping the single mode core with single mode laser diodes would provide ideal overlap but such laser diodes are limited in power. On the other hand, pumping a single clad fibre with a high power but multimode diode laser is extremely inefficient.

Developments in fibre design led to double-clad fibre structure in which the high power multimode pump laser is coupled into a large inner cladding (ic) with refractive index lower than the core but higher than the outer cladding (oc) ($n_{core} > n_{ic} > n_{oc}$). The pump light is guided in the inner cladding by total internal reflection enabling pump light to overlap with the core and being absorbed by the active dopants in the core, which enables amplification of the seed light. Thus single mode beam quality can

be maintained despite the use of high power multimode laser diodes as pump sources. Such fibre systems are said to be cladding pumped. Schematic of a cladding pumped double-clad fibre amplifier is shown in Figure 3.2.

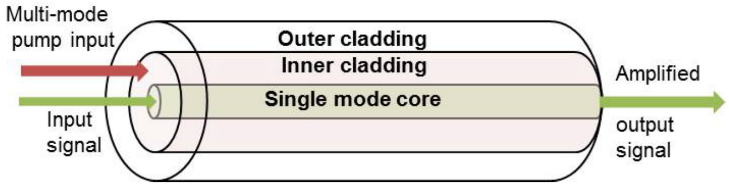

Figure 3.2: Schematic of a cladding pumped double-clad fibre amplifier.

High overlap of the pump modes with the doped area results in high efficiency of pump absorption in core, which in turn increases the gain and power efficiency of the active fibre. This approach is simply achievable through single-clad fibres while this overlap is lost in case of a double-clad fibre design. Depicted geometry of double-clad fibre in Figure 3.2 (with a centered circular core) is the simplest design and the easiest one to be fabricated and used.

Moreover, birefringence phenomenon in fibres splits the light propagation into two different paths as a result of different refraction indices in the fibre core. Therefore, polarisation maintaining (PM) fibres as the common employed method are used to maintain the state of polarisation of the fibres.

3.2.2 Large-Mode-Area Fibres

The invention of cladding pumped schemes resulted in a rapid rise in output powers. At such high powers nonlinear phenomena in the fibres become prominent. Reduction of nonlinear effects and the subsequent fibre damage can be addressed by increasing the core size. This led to the introduction of large-mode-area (LMA) fibres.

In general, increasing the mode area affects the single mode operation of the core and reduces the beam quality. There are two possible ways to maintain single mode operation while increasing the mode area: 1) the numerical aperture (NA) of the core should be kept small; 2) the guidance of the higher order modes must be kept weak. For conventional solid core fibre designs, a low NA core leads to a number of fabrication challenges and the weak guidance introduces significant losses to the fundamental mode. This limits the scalability of core area in conventional solid core fibres. In that regard, LMA fibres are designed to be used, which have relatively large mode areas but are optimised to propagate a single or small number of modes. They have a much larger core size and less refractive index difference between core and cladding than a conventional single-mode fibre. The low NA central core region and the design of the refractive index profile in the core helps to give maximum gain to the fundamental mode and the ability to still provide diffraction limited output beam quality light by managing the fibre launching and bending carefully. In addition to reducing the intensity in the fibre for a given power, the required fibre length can be reduced as the core-clad area ratio increases with larger core size, enhancing overlap of pump modes with the core, thus enabling further suppression of nonlinearities and scaling of the power [15]. However, thermal and nonlinear effects

can still cause significant pulse reshaping in spite of careful fibre design. Some important nonlinear effects in fibre devices are briefly described in the subsection 3.3.2.

3.2.3 Master Oscillator Power Amplifier (MOPA)

The term master oscillator power amplifier refers to a configuration consisting of a master oscillator (or seed laser) and an optical amplifier to boost the output power. Although a MOPA configuration is in principle more complex than a laser, which directly produces the required output power, it enables optical power scaling in comparison to a laser while maintaining required performance. Furthermore, the combination of an existing laser with an existing amplifier (or an amplifier chain) may be simpler to create than developing a new laser with higher output power.

Fibre based MOPA systems incorporate a seed laser that is amplified to the desired level with the use of single pass fibre amplifiers. The first amplifier known as the pre-amplifier provides sufficient gain to the signal to have adequate optical power to operate the power amplifier. According to the targeted output power from the power amplifier, a chain of pre-amplifier stages may be required if the output power from a single stage preamplifier is not high enough to properly seed the power amplifier.

Rare-earth doped fully-fiberised pulsed MOPAs have attracted high interest over the past decade due to their potential advantages in terms of efficiency, compactness, reliability, ease of thermal management and capability of significant scaling of both the peak and average power levels [15, 104]. Even so, ASE suppression and the nonlinear effects have to be addressed in fiberised MOPA systems. Also, LMA doped fibres are usually used in power amplifier stages, which may guide either one or several transverse modes enabling mode tailoring for applications.

CW pumped, pulsed output fibre MOPA architectures are represented as new class laser sources for advanced industrial applications including marking and materials processing (e.g. works of [105] and [35]) in which the final amplifier is used as a reservoir of energy. Nevertheless, if significant fraction of the stored energy is extracted by an optical pulse, the effect of gain saturation becomes relevant, which means that the amplifier gain drops during the pulse. This can lead to a deformation of the temporal pulse shape. Hence, by tailoring the pulse shape from the seed source, the desired pulse shape after amplification can be obtained, which is one of the many advantages of a MOPA system (more details in subsection 3.4.1).

However, the MOPA approach comes with some disadvantages too. One major drawback is the sensitivity of such amplifier to back-reflections, which can potentially cause damage to the master laser. The most widely used approach to safeguard seed laser from unwanted feedback is to introduce a Faraday isolator in between the seed and the amplifier.

Experimental setups reported in this thesis are based on the MOPA configuration with suitable semiconductor diode seeds generating nanosecond or picosecond pulses directly or by using femtosecond mode-locked laser sources and dispersive pulse stretching for spectrally shaped, tailored picosecond pulse generation. Each configuration is designed to enable power and energy scaling as will be detailed in the following chapters. Note that Yb-doped few-mode fibres (FMFs), which are multimode fibres supporting only a

relatively small number of guided modes are employed in power amplifier stages.

3.3 Pulse Propagation: Dispersion and Nonlinear Effects in Optical Fibres

Propagation of optical pulses inside a fibre influence their shapes and spectra by both nonlinear effects and dispersion. Strong nonlinear effects are expected for large amplitude pulses. Linear dispersion such as group velocity dispersion can also be important. The electric field **E** of a propagating optical pulse in nonlinear dispersive media in the slowly varying envelope approximation can be written as [106]

$$\mathbf{E} = \frac{1}{2}\boldsymbol{x}F(x,y)A(z,t)\exp[i(\beta_0 z - \omega_0 t)] + c.c. \tag{3.1}$$

where $\boldsymbol{x}$ is the polarisation unit vector, $A(z,t)$ is the slowly varying pulse envelope, $F(x,y)$ is the transverse distribution inside the fibre core and β_0 is the propagation constant at the carrier frequency ω_0.

3.3.1 Optical Fibre Dispersion

Dispersion is an important phenomena in pulse propagation in optical fibre due to different spectral components with in the pulse traveling at different speeds. Frequency dependency of the refractive index n(ω) manifests this dispersion. Effects of dispersion can be driven mathematically by expanding the mode propagation constant β using a Taylor series at ω_0, centre frequency of the pulse spectrum as [106]

$$\beta(\omega) = \beta_0 + \beta_1(\omega - \omega_0) + \frac{1}{2}\beta_2(\omega - \omega_0)^2 + ... \tag{3.2}$$

The parameters β_1 and β_2 are related to the refractive index n and its derivatives through the relations

$$\beta_1 = \frac{1}{v_g} = \frac{n_g}{c} = \frac{1}{c}(n + \omega\frac{dn}{d\omega}) \tag{3.3}$$

$$\beta_2 = \frac{1}{c}(2\frac{dn}{d\omega} + \omega\frac{d^2n}{d\omega^2}) \tag{3.4}$$

where n_g is the group index and v_g is the group velocity. Thus β_1 is the inverse of the group velocity, which refers to the speed of the envelope of an optical pulse propagating in the fibre. β_2 is the dispersion parameter of the group velocity dispersion and is responsible for pulse broadening. When $\beta_2 > 0$, the fibre exhibits normal dispersion and the high frequency (blue-shifted) components will travel slower than the low frequency (red-shifted) components of the same optical pulse. When $\beta_2 < 0$, anomalous dispersion occurs. The dispersion parameter D is usually used to represent β_2 and the relation between the two is given by [106].

$$D = -\frac{2\pi c}{\lambda^2}\beta_2 \tag{3.5}$$

In the frequency domain, the effect of dispersion on frequency components will cause each and every component to travel at a different velocity. In the temporal domain, the pulse will be either broadened or compressed depending on the dispersion parameter, however in the frequency domain no change will be observed as dispersion alone generates no new frequency components. It is worth mentioning that all the fibres used in this thesis are in normal dispersion region.

3.3.2 Optical Fibre Nonlinear Effects

Applying an intense electromagnetic field to any transparent dielectric medium causes nonlinearity due to the distortion of the electron-charge distributions in the medium. This will lead to an induced total polarisation **P** as a result of the applied electric field **E** and can be represented with this general relation [106],

$$\mathbf{P} = \epsilon_0(\chi^{(1)}.\mathbf{E} + \chi^{(2)} : \mathbf{EE} + \chi^{(3)}\vdots\mathbf{EEE} + ...) \tag{3.6}$$

where ϵ_0 is the vacuum permittivity and $\chi^{(j)}$ (j=1,2,...) is jth order susceptibility. The linear susceptibility $\chi^{(1)}$ makes the dominant contribution to **P**, which is related to the refractive index n and the attenuation constant α. The second order susceptibility $\chi^{(2)}$ is responsible for nonlinear effects such as second harmonic generation and sum frequency generation. This second order susceptibility will be zero for any material that has a centro-symmetric arrangement of atoms or an amorphous structure such as silica fibre. The third order susceptibility $\chi^{(3)}$ is the lowest order nonlinearity effect in silica fibres and is responsible for phenomena such as four wave mixing and third harmonic generation. It also causes nonlinear variation of the index of refraction, which in pulsed systems is important because it results in self phase modulation (SPM).

3.3.2.1 Self-Phase Modulation

Most of nonlinear effects in optical fibres are originated from nonlinear refraction through the intensity dependency of the refractive index expressed as

$$n = n_0 + n_2 I \tag{3.7}$$

where n_0 is the linear refractive index value and n_2 is the nonlinear index of refraction, which is related to the third order susceptibility $\chi^{(3)}$ [1]. This leads to self-induced phase shift of the optical field as its propagating in an optical fibre. This effect is known as self phase modulation (SPM) and results in the spectral broadening of optical pulses. The magnitude of the phase shift in a fibre can be obtained by its proportionality to intensity and the effective fibre length $L_{eff} = [1-\exp(-\alpha L)]/\alpha$ (L accounts for the length of fibre and α for fibre losses) as [107]

$$\phi(t) = k_0(n_0 + n_2 I)L_{eff} \quad , \qquad k_0 = \frac{2\pi}{\lambda_0} \tag{3.8}$$

k_0 is the wave number with an inverse relation to the wavelength and I is the signal intensity. The intensity-dependent nonlinear phase shift due to SPM is proportional to $\phi_{NL} \propto \gamma P L_{eff}$ when $\gamma = \frac{n_2 k_0}{A_{eff}}$ is the nonlinear Kerr coefficient and P is the instantaneous power for the effective fibre mode area A_{eff}. Also, the phase shift derivatives will be

$$-\frac{d\phi(t)}{dt} = -\frac{4\pi n_2 L_{eff}}{\lambda}\frac{dI}{dt} = -\frac{4\pi n_2 L_{eff}}{\lambda A_{eff}}\frac{dP}{dt} = \omega(t) \tag{3.9}$$

The instantaneous angular optical frequency of the pulse is related to the rate of change of phase $\delta\omega = -\frac{\partial\phi}{\partial t}$. Thus, the instantaneous frequency can be derived as

$$\omega(t) = \omega_0 - \frac{4\pi n_2 L_{eff}}{\lambda A_{eff}}\frac{dP}{dt} \tag{3.10}$$

From Equation 3.10, it can be deduced that the SPM induced spectral change, for a fixed length of fibre, is related to the rate of change of instantaneous power of the pulse. By considering a Gaussian pulse, the leading edge of the pulse will have positive $\frac{dP}{dt}$ value. Thus, the $\delta\omega$ will be negative; i.e the frequency is down-shifted. Similarly, at the trailing edge of the pulse, $\delta\omega$ will be positive and the frequency will be up-shifted and therefore the spectrum should be symmetrically broadened from the centre frequency due to SPM. If the pulse is asymmetric, the $\delta\omega$ will differ between the leading and trailing edges of the pulse and this influence of SPM induced spectral broadening creates an oscillatory structure covering the entire frequency range with the most intense outermost peaks. The number of peaks M depends on the maximum phase shift ϕ_{max} and increases linearly.

$$\phi_{max} \approx (M - \frac{1}{2})\pi \tag{3.11}$$

Therefore it provides an estimation of the SPM-induced spectral broadening and will result in an asymmetrically broadened spectrum.

In order to check the impact of the nonlinear phase shift change in the shaped pulses, the B-integral evolution in the entire laser system calculated, where $B = \int_0^L \gamma P_{peak}(z)dz$ (P_{peak} is the peak power of the laser pulse) in the temporally dependent nonlinear phase shift of the laser pulse in the fibre, which expressed as $\varphi_{NL}(t) = BI(t)$. Here $I(t)$ is considered as the normalized intensity ($\max[I(t)] = 1$) [108].

In high energy fibre MOPA systems, the amplified pulses can be affected by gain saturation within the fibre amplifiers that directly influences the output pulse shape. The pulse shape gets distorted with higher leading edge and an exponentially decreasing trailing edge.

3.3.2.2 Stimulated Raman Scattering

Passing the light through any molecular medium may result in losing some part of the energy due to energy transfer from the optical field to the dielectric medium or vice versa. As a result the frequency of the incident light will either be upshifted (known as anti-Stokes wave) or downshifted (Stokes wave) (Figure 3.3). The amount of frequency shift is determined by the vibrational modes of the medium. This interaction of light with optical phonons, which creates such scattering is stimulated Raman scattering (SRS). A rapid growth of the Stokes wave can be observed and a significant fraction of the incident light energy can be transferred to that Stokes wavelength.

In silica fibres, the Raman gain spectrum is very broad and extends up to 30 THz [109]. The measured peak gain at 1.06 μm is $g_R = 1 \times 10^{-13}$ m/W with a Stokes shift of $\Delta\nu = 13.2$ THz (440 cm^{-1}) (Figure 3.4). The peak gain varies with pump wavelength as $1/\lambda_p$. If the frequency difference between the pump and Stokes waves lies within the Raman gain bandwidth, the SRS power can be described by the following equations [106],

$$\frac{dI_s}{dz} = g_R I_p I_s - \alpha_s I_s \tag{3.12}$$

$$\frac{dI_p}{dz} = -\frac{\omega_p}{\omega_s} g_R I_p I_s - \alpha_p I_p \tag{3.13}$$

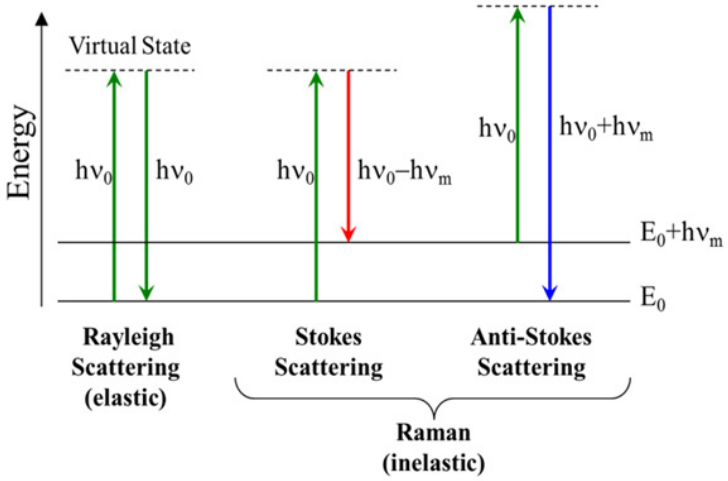

Figure 3.3: Jablonski diagram representing quantum energy transitions for Rayleigh and Raman scatterings (from `bwtek.com`).

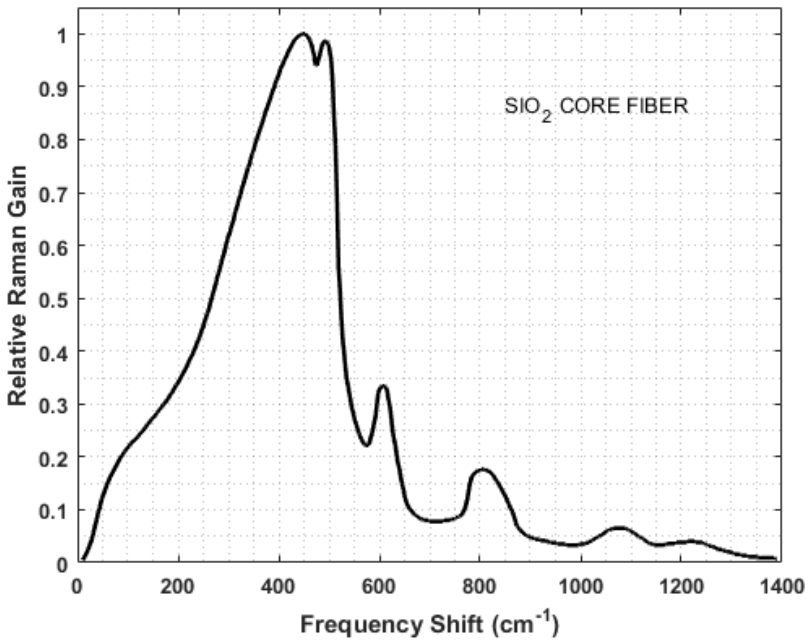

Figure 3.4: Raman gain coefficient curve of a silica core single mode fibre. This curve is normalized to 1.0 at the Stokes shift of 13.2 THz [109].

where g_R is the Raman gain coefficient, α_s and α_p are fibre loss at Stokes and pump frequencies, respectively. I_s is the Stokes intensity, and I_p is the pump light intensity. By neglecting the pump depletion in Equation 3.13, it is possible to solve the coupled equations analytically,

$$I_s(L) = I_s(0)\exp(g_R I_0 L_{eff} - \alpha_s L) \tag{3.14}$$

where I_0 is the incident pump intensity at z=0.

In practice, spontaneous Raman scattering initiates throughout the fibre length and builds up through the SRS process. The Raman threshold is defined as the input pump

power at which the Stokes power becomes equal to the residual pump power at the fibre output,

$$P_s(L) = P_p(L) \equiv P_0 \exp(-\alpha_p L) \tag{3.15}$$

where $P_0 = I_0 A_{eff}$ is the input pump power and A_{eff} is the effective core area. The critical pump power required to achieve the Raman threshold is given by [106]

$$P_0^{cr} \approx 16 \frac{A_{eff}}{g_R L_{eff}}. \tag{3.16}$$

Therefore, the maximum power that can be launched into the fibre without observation of any significant growth of Raman Stokes can be estimated from Equation 3.16. Usage of the fibres with larger core diameter such as LMA fibres and/or shortening the effective length of the fibre will effectively increase the Raman threshold power. If the power in the Stokes wave exceeds the Raman threshold, the Stokes can act as a pump for a second order Stokes wave initiating the cascaded SRS process.

3.3.2.3 Stimulated Brillouin Scattering

Stimulated Brillouin scattering (SBS), similar to SRS, can occur in optical fibre and originating from the backscattering of signal light by acoustic waves in the optical material. Acoustic waves generate from the pump field via the electrostriction process periodically modulating the refractive index, acting as a Bragg grating. The backscattered light is shifted to lower optical frequency (longer wavelength) due to the Doppler shift emerged by the speed of the grating as a result of the forward and backscattered waves optical frequency difference, which depends on the fibre material. The Brillouin-shift frequency is about 11 GHz in silica fibres and has a narrow gain bandwidth of ∼50 MHz (compared to SRS). The SBS effect in a fibre can stimulate more of the forward traveling light to be backscattered in an avalanche-like process. The backscattered light from SBS is in contrast with SRS that can occur in both directions [106, 110]. The power at which the Stokes wave at the input end becomes equal to the pump power at the output, is defined as SBS critical power and can be expressed as

$$P_0^{cr} \approx 21 \frac{A_{eff}}{g_B L_{eff}} \tag{3.17}$$

where A_{eff} and L_{eff} are the effective mode area and interaction length as defined in the previous section. The peak value of the Brillouin gain coefficient or $g_B = 5 \times 10^{-11}$ m/W, which is higher than the Raman gain by a factor of ∼500, leads to a low SBS threshold for narrow linewidth pump sources. SBS is a dominant nonlinear process in optical fibres for pump pulses with a width >1 ns but it nearly ceases to occur for shorter pulses due to the long time scale needed for acoustic phonons to build up.

3.4 Temporal Pulse Shaping

They are many techniques for temporal pulse shaping implementations. For the nanosecond pulse regime the method based on active pulse shaping has proven its capability in high energy (∼2 mJ) MOPA laser systems [31, 33, 34]. Temporal pulse shaping technique used in this thesis and some examples of pulse distortion and pulse

reshaping in high gain laser mediums are presented in the following (subsection 3.4.1).

In picosecond regimes, the Fourier-domain of a pulse or sequence of femtosecond pulses is manipulated to alter either amplitude or phase (or both) properties of the pulse attaining the desired temporal pulse profile [50]. The concept and technique of picosecond temporal pulse shaping applied in this thesis are explained in subsection 3.4.2.1.

3.4.1 Temporal Pulse Shaping Parameters in Nanosecond Pulse Regime

When low energy pulse propagates in a high gain laser medium, which has uniform inversion along its length, the pulse grows exponentially with distance in an unsaturated amplifier. However, if energy and gain lead to gain saturation, the tail of pulse experiences a different level of population inversion than the leading edge resulting in distorted pulse shapes [31, 32, 34, 104, 111]. In this case, the amplification process is more complicated and can be described by nonlinear time-dependent radiation transfer equation based on Siegman and Frantz-Nodvik analysis [1, 112].

By applying the Frantz-Nodvik equation [112], the output pulse shape can be estimated by the gain ($G(t)$) and the input pulse shape. Calculation of output pulse shape depends on the given input pulse shape and a given initial gain (i.e. small signal gain G_0), which must be calculated using fibre properties and pump power level (Equations 3.18 and 3.19) [1].

$$G(t) = 1 + (G_0 - 1)e^{-U_{out}(t)/U_{sat}} \tag{3.18}$$

$$I_{out}(t) = G(t)I_{in}(t) \tag{3.19}$$

where, $U_{out}(t)$ and U_{sat} are the output signal pulse energy and the saturation energy per unit area respectively. $I_{in}(t)$ is the input pulse intensity profile and $I_{out}(t)$ is the corresponding signal intensity profile at the output plane, both measured in the time coordinate t.

Adaptive shaping of optical pulses as reported in [31, 32] for a diode seeded nanosecond fibre MOPA system was demonstrated by controlling electrical pulses to the laser diode, which allows control of the pulse shape at the output of the system and provides compensation of pulse deformation due to the saturation effect in fibre amplifiers. Figure 3.5 shows the schematic of the active shaping process to produce customised output optical pulse shapes from a MOPA system. The directly modulated diode can be driven with an arbitrary waveform generator (AWG) to yield a specific desired pulse shape at the output. The output pulse shape is analysed by the computer and compares it with the desired pulse shape. The algorithm determines the fitness factor and decides a new pulse shape to feed to the AWG. This iterative method keeps searching until the final output pulse is as desired pulse shape. However, pre-analytical estimation followed by a few iterative feedback is enough to generate the expected temporal shapes.

The output pulse shape can alternatively be calculated using Equations 3.18 and 3.19, for instance in the case of a square input pulse shape. If the input pulse

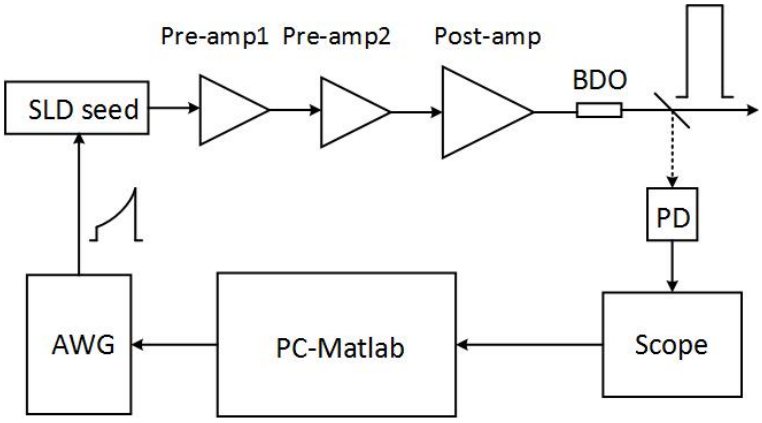

Figure 3.5: Schematic graph of active shaping process in fibre MOPA [32]. BDO: beam deliver optics, PD: photo diode.

experiences large gain, the output pulse will have a spike on the leading edge. As a result, the power level at the tailing edge of the pulse will significantly drop to a level that is much lower than the peak power of the leading edge. Consequently, the pulse duration at full width half maximum (FWHM) will be substantially reduced compared to the original width. The instantaneous gain $G(t)$ follows the exact shape of the output pulse in this case.

Figure 3.6 (a) illustrates an example of the square pulse implementation when the input power is large $G_0 U_{in} \gg U_{sat}$. Gaussian pulse or any other shaped pulses with a rounded leading and trailing edge depicts very little changes at the output even under significant saturation effects as shown in Figure 3.6 (b). Hence the pulse duration remains practically the same despite a slight advancement in peak position due to a significant reduction in population inversion during the peak and trailing edge of the pulse.

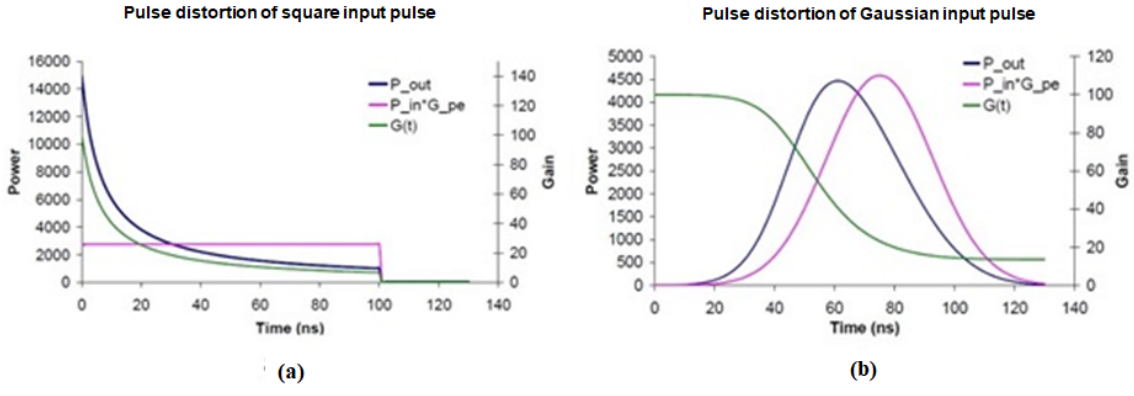

Figure 3.6: Reshaping of a) square pulse and b) Gaussian pulse input with $G_0 = 100 = 20$ dB, and $E_{sat} = 0.1$ mJ, energy gain a) $G_{pe} = 18.5 = 12.7$ dB and b) $G_{pe} = 30 = 14.8$ dB [32].

In practice, pulse reshaping in my research was realised with a Tektronix Arbitrary Waveform Generators (AWG 7000-series). In order to define the pulse shape with a small number of variables, a pulse consisting of several smooth curves is one of the best options to choose. Since gain saturation follows an exponential term, exponential curves are a

suitable choice. For example, each curve between the two points A(T_0, l) and B(T_f, l) (Figure 3.7) can be characterised by

$$y(t) = l + \frac{h - l}{e^{\alpha(T_f - T_0)}}(e^{\alpha(t - T_0)} - 1) \tag{3.20}$$

where T_0 is the starting time, T_f end time of the curve, $T = T_f - T_0$ the duration of

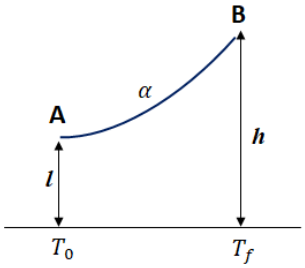

Figure 3.7: Element curves to characterise the AWG output.

the curve, t the time between T_0 and T_f and α an exponential factor. If α is positive, the curve takes a concave format, while a negative α depicts a convex format. Also, α cannot be equal to zero, yet it can approach a very small number to give a straight line between the two points A and B.

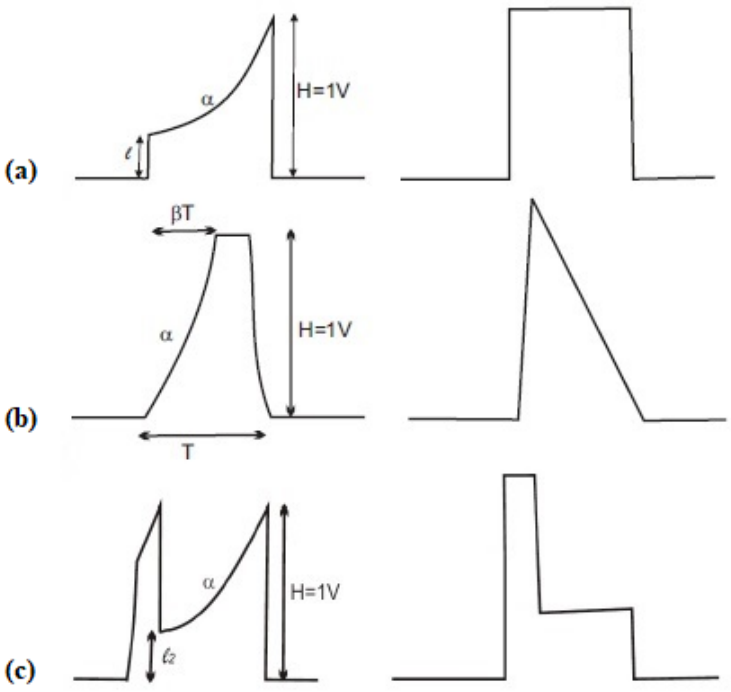

Figure 3.8: Estimation of the inputs pulses (on left) to give desired a) square, b) triangular and c) step pulses (on right) [32].

By choosing appropriate variables especially for the exponential term α in the Equation 3.20, different pulse shapes such as square, triangular or two-step pulses can be produced. Figure 3.8 shows examples of these inputs to achieve desired square, triangular and step pulses at the output. The work in this thesis used a PC-based

adaptive algorithm to find the required parameter values. The adaptive process is much quicker with the reduced number of parameters in Equation 3.20 compared to using individual co-ordinates for each point on the pulse [31,32,34].

3.4.2 Temporal Pulse Shaping in Picosecond Pulse Regime

Typically, peak power limitations in fibres mean that picosecond pulse energies are below the saturation fluence of the amplifier and hence the entire length of the pulse will experience uniform inversion and will be amplified uniformly. This may seem to simplify the challenge of generating desired temporal pulse shapes such as double or triple peaks pulses or step pulses in picosecond or femtosecond pulse regimes due to their known advantages in materials processing application. However, temporal pulse shaping cannot be implemented through direct modulation of the laser diode with an AWG as the current rise time of the laser diode drivers are still longer than the pulse width. WaveShapers operating in the spectral domain are able to do the shaping of such short optical pulses as explained below. Figure 3.9 illustrates a general schematic of the temporal pulse shaping system in a power scaling configuration when applying a WaveShaper. This approach achieves good results but, due to the response time of the phase-plate in the device, it applies uniform shaping to the pulse train rather than shaping in a pulse-on-demand basis.

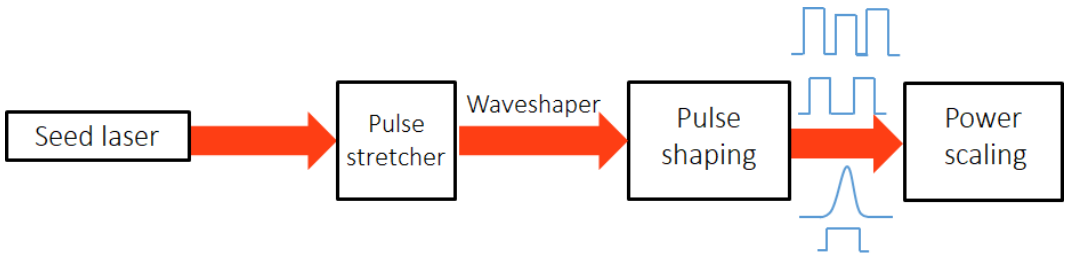

Figure 3.9: General picosecond MOPA laser system to implement the temporal pulse shaping.

3.4.2.1 WaveShaper Principle

Pulse shaping of short pulses in femto- or picosecond range requires fine adjustment of the phase and amplitude characteristics of the optical signal. A WaveShaper achieves this functionality based on Fourier-domain pulse shaping [113, 114]. Tailoring the amplitude and phase characteristics of the optical signals offers the possibility of defining arbitrary pulse shapes. Essentially, it can be explained by an input temporal waveform $E(t)$ with the ideal full characterisations in terms of phase and amplitude that can then be formulated to an expression for the desired output $A(t)$. Transforming of $E(t)$ into $A(t)$ in the spectral domain ($E^{'}(f)$ and $A^{'}(f)$, respectively) allows to have an intrinsically static transformation without requiring to apply rapidly varying operations on the time scale of the short pulses. A spectral filter $F(f)$ ($F(f) = A^{'}(f)/E^{'}(f)$) can then be easily calculated to investigate the linear transformation in the spectral domain to retrieve the Fourier-transform of the desired output pulse. To avoid the more complex calculations needed to achieve truly arbitrary pulse profiles, in this thesis, I used just spectral amplitude shaping by first stretching the femtosecond pulses using dispersion so the time profile becomes the Fourier transform of the transform-limited time profile. The WaveShaper benefits from the

dispersion-induced frequency-to-time mapping (FTM) means the output temporal intensity profile of the laser is expected to be closely similar to the shape of the desired input pulse spectrum shape for the chirped pulse, as illustrated in Figure 3.10 ([114, 115]). A nice feature is that seed pulse energy is retained, whereas it would have been removed in the case of a transform-limited pulse shaping methods that carve picosecond pulses by narrowing the spectra of femtosecond input pulses.

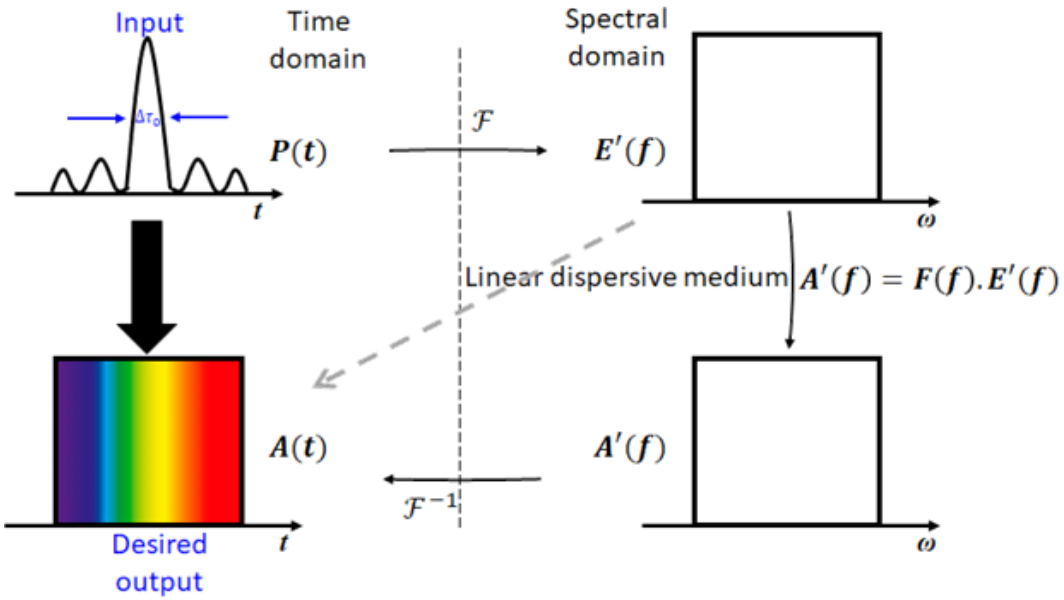

Figure 3.10: Dispersion-induced frequency-to-time mapping in a linear second-order dispersive medium. $P(t)$ is power of the input temporal waveform $E(t)$.

This occurs when the pulse meets the condition of the time-domain Fraunhofer diffraction in the far-field for an input signal energy is confined to a very small duration $\Delta\tau_0$ and a sufficiently large magnitude of the second-order dispersion coefficient $\ddot{\Phi}$ ($\partial^2\Phi/\partial\omega^2$), which is usually referred to as far-field FTM (FF-FTM) [116, 117]:

$$\ddot{\Phi} \gg \frac{\Delta\tau_0^2}{8\pi} \triangleq TBP^2 \frac{\pi}{2\Delta\omega^2} \tag{3.21}$$

Here $\Delta\omega = 2\pi\Delta\nu$ is the full spectral width of the input spectrum and $TBP = \Delta\tau_0\Delta\nu$ is the time-bandwidth product of the input waveform. Hence, the output pulse envelope is proportional to the Fourier transform of the input pulse envelope while the duration of the output pulse Δt_0 is determined by:

$$\Delta t_0 \approx \mid \ddot{\Phi} \mid \Delta\omega. \tag{3.22}$$

The output pulse width is proportional to both $\Delta\omega$, the spectral width of the shaped pulse and the second-order dispersion coefficient, $\ddot{\Phi}$.

In essence, if we consider a 100 fs Gaussian input pulse, after 1 m length of for example Nufern PM980 fibre (D≈-40 ps/nm.km dispersion @1040 nm), the second-order dispersion coefficient will be $\ddot{\Phi} = \beta_2 \cdot L \approx 2.3 \times 10^{-26} s^2$ and the right hand side (RHS) of the Equation 3.21 will be $\sim 0.04 \times 10^{-26} s^2$, so the pulse is not in the

time domain equivalent of the Fraunhofer regime with this short fibre length while for a 100 m fibre length the $\ddot{\Phi} \approx 2.3 \times 10^{-24} s^2$ satisfies the FF-FTM condition. Also, if the spectral bandwidth $\Delta\omega$ of the input pulse is reduced having longer pulse width of ∼1ps (transformed limited Gaussian pulse), the RHS of Equation 3.21 will be increased to $\sim 0.04 \times 10^{-24} s^2$ to marginally comply with far-field condition when for larger pulse widths such as ∼100 ps it clearly depicts that the FF-FTM requirement cannot be fulfilled with a reasonable length of fibre as the stretcher. Hence, a femtosecond laser source is required to implement the temporal pulse shaping rather than a picosecond one.

Note that the output pulse will be in the range of ∼1-100 picoseconds (Equation 3.22) by choosing stretcher length to enable the picosecond temporal shaping including picosecond features. Short stretching ratio results in the individual features within the shaped pulse having such a short duration that they cannot well satisfy the FF-FTM criteria, as discussed above. On the other hand, applying larger stretcher, leading to bigger stretching ratio, can restrict the smaller temporal features to the ranges beyond e.g. 100ps, out of the expected range for picosecond pulse shaping desire of the current reported ERM project in this thesis unless we apply a compressor, which would compromise stability and increase costs (Figure 3.9). Moreover, larger stretcher fibre results in higher signal power attenuation, so pre-amplification stages are inevitable. In terms of fiberised systems, increase of the SPM effects in the final amplifier should be considered along with desired dispersion.

The WaveShaper system (Finisar 1000/SP) used in this project fundamentally consists of four components, which are shown schematically in Figure 3.11. This schematic depicts how this type of WaveShaper is functioning by its core element, Liquid Crystal on Silicon (LCoS) Technology, to implement the principle of Fourier-domain pulse shaping.

In order to ensure stable polarisation states aligned with the principal axes of the optics for input/output ports, polarisation maintaining fibres are used. Conventional grating is applied to perform transformations from the time domain to the frequency domain and vice versa. Spatial divergence of the light in the vertical direction can be provided by using appropriate imaging optics.

Spectral filtering, which is needed before moving back into time domain, is implemented by LCoS chip. This chip consists of a reflective, two-dimensional array of pixels, which can apply a controllable phase shift (modulo 2π) to incident light. Input light is spectrally dispersed along the horizontal axis (spectral axis) of the LCoS array and spatially diverges along the vertical axis (deflection axis) as the imaging optics and grating are arranged in this configuration. Each column of pixels can be taken into account as an element that operates on two parameters, phase retardation and amplitude attenuation of a spectral component. In this case any type of pulse shape that is allowing the WaveShaper to function in its key specifications, can reliably and accurately yield in the femtosecond to picosecond pulse length regimes [114].

Recent application of this WaveShaper in a femtosecond fibre chirped pulse amplification (CPA) system was reported in [50], which formed the basis of operation for the picosecond temporal shaping in my laser systems in chapter 7. It is worth mentioning that since the maximum power rating of the used WaveShaper is less than

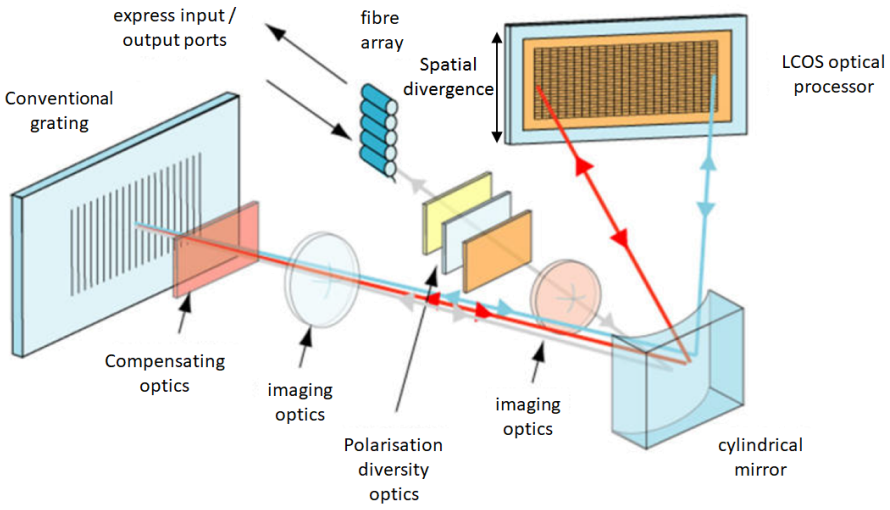

Figure 3.11: Schematic layout of the WaveShaper. Beam path is as follows (in order of causality): forward direction gray line is input and is relayed to the grating by the cylindrical mirror; red and blue lines are the spectrally-dispersed light and are relayed to the LCoS chip; have been processed by the LCoS chip and are reconverging as it is relayed back to the grating; back direction gray line is the output and is relayed back to the output fibre [113]. The schematic shows a telecommunications version with multiple input/output channels while our model has only one channel.

500mW, it needs to be inserted before the amplifier chain for safe operation.

3.4.2.2 Cross-Correlator

To be able to analyse the accuracy of the temporal pulse shaping, a cross-correlation trace was recorded for each shape. That is more advanced and provided better information rather than just an auto-correlation trace (in [50]). Our setup required a cross-correlator with a scan range of higher than 100 ps. Here, a brief background about the cross-correlation principle and our home-made cross-correlator characteristics are explained.

The common way to measure pulses in time domain is employing a photodiode that produces electrons if it absorbs photons. It measures the integral of the pulse intensity, but this is limited by the maximum resolution of our equipment of ~20 ps, besides this method provides no phase information [118, 119]. A method for shorter pulses is the second harmonic generation (SHG) intensity auto-correlator (Figure 3.12). In an auto-correlator, replica beams pass through a nonlinear crystal to generate the second harmonic and the delay is changed by a delay stage (Auto-correlation intensity $A(\tau) \equiv \int_{-\infty}^{+\infty} I(t)I(t-\tau)dt$).

However, the output shape is not a direct representation of the input so it is hard to interpret for complex pulse profiles. Therefore, getting a more precise verification for the pulse shapes can be typically gained using a cross-correlator. In contrast to published results in [50], where the auto-correlation measurements were used to validate temporal pulse shapes, here we applied a home-built cross-correlator. It is a direct, fast and accurate technique to measure pulses with complex shapes.

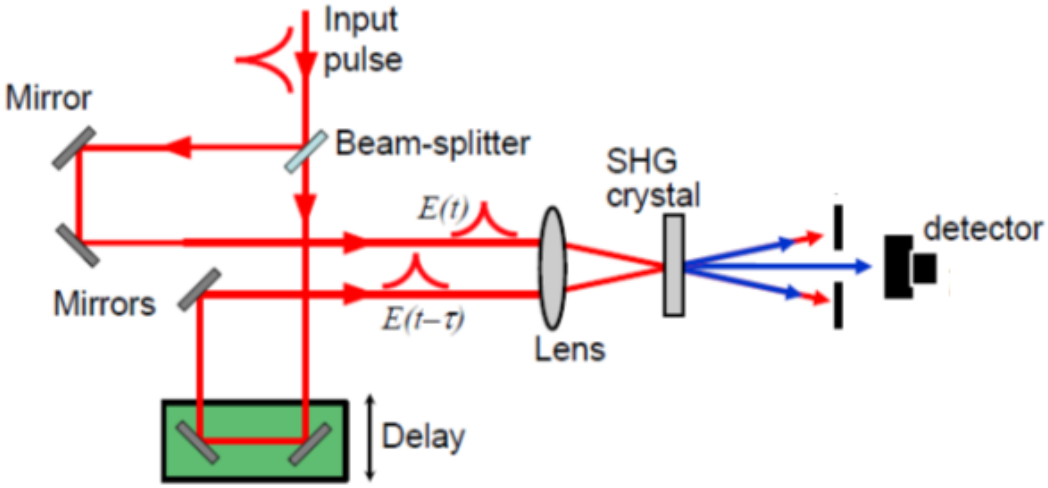

Figure 3.12: Schematic of an intensity autocorrelator `https://www.brown.edu/research/labs/mittleman/sites/brown.edu.research.labs.mittleman/files/uploads/lecture14.pdf`.

In the cross-correlator, two beams are overlapping to generate sum frequency generation (SFG). Now one beam has a much shorter pulse width to fully determine the unknown pulse intensity as shown in Figure 3.13. The cross-correlation intensity is calculated through the equation

$$C(\tau) \equiv \int_{-\infty}^{+\infty} I(t) I_{ref}(t-\tau) dt. \tag{3.23}$$

Delay determines the resolution of cross-correlation trace, which means the step length of the delay stage is the key parameter. Shorter step length will contribute to higher resolution. For example a step length of 0.1 mm corresponds to 666 fs in time domain.

A cross-correlator built by Mr. Duanyang Xu in ORC was employed to measure the temporal pulse profiles (Figure 3.13). The reference pulse was created from a fiberised monitor tap arm after passing a core-pumped amplifier stage to have enough peak power before reaching the SHG crystal. The reference pulse dispersion was compensated with a pair of diffraction gratings (loss ∼6 dB round trip through the gratings pair).

This system is fully controlled and measured by LabView to construct time-domain shape images of pulses. The delay stage used a roof-mirror on a high precision linear stage from Nanomotion Ltd (Model: FB050-020-50N4A-FB-HR4k). The measurement ran by an accuracy of 0.05 mm corresponding to 333 fs time interval leading about 400 data points for each shape. The medium that produces the SFG signal is a 5mm×5mm×0.3mm Type I BBO crystal that is placed on an adjustable rotation mount to achieve phase matching conditions and providing a maximum detection level of 17 dB above background.

In order to reduce the noise due to the scattered laser light at higher energy, two dichroic mirrors (HR@0.5 μm, HT@1 μm) filtered out the 1 μm background light. A blue filter and a beam tube placed in front of the detector provided more filtering.

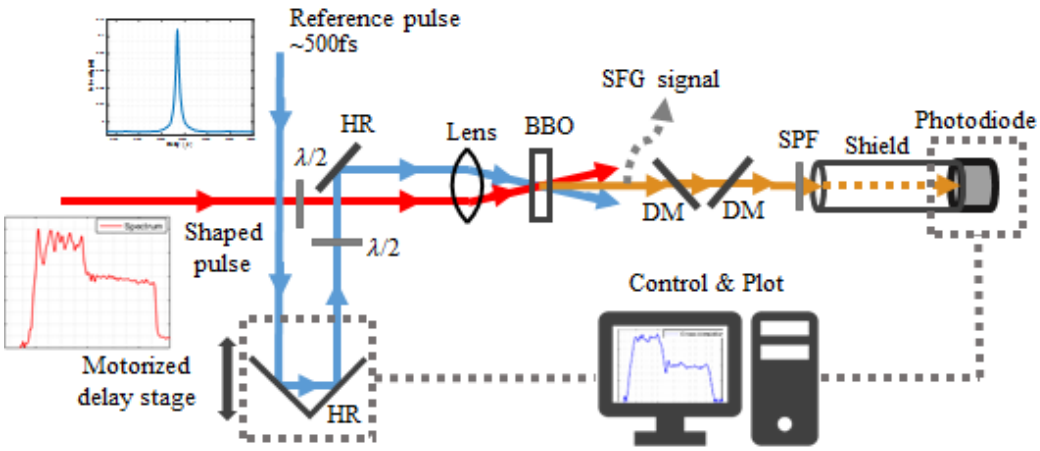

Figure 3.13: General cross-correlation setup for the temporal pulse shaping verification, DM : Dichroic mirror, HR: High reflectivity mirror.

This cross-correlator has been used to verify our measured picosecond temporal profiles in chapters 6 and 7.

3.5 Spatial Beam Shaping

Development of robust fundamental transverse mode in large-mode-area (LMA) fibres has attracted increasing attention over the last decade. This has been done by bend-loss filtering, specially designed fibres (e.g. with a photonic crystal geometry, tailored gain dopant distribution in the fibre core [15, 120]) to facilitate scaling of mode area whilst providing suppression of unwanted higher order modes. Recently, operation on individual higher-order modes in few-moded rare-earth-doped fibre lasers have particularly gained interest. Increase in the A_{eff} of the fibre lasers raised the threshold for damage and detrimental nonlinear loss processes, which in consequence allow further scaling of output power and pulse energy. Unique properties (i.e. intensity profile, polarisation and phase distribution) of some of these higher order modes enables their application in micro-machining, prototyping, marking, etc., so is ideal for laser materials processing, besides in future provides the implementation of practical and power scalable mode shaping methods [22, 52, 53]. A recent review of adaptive optics based approaches to laser processing provides an indication of the state-of-the-art with active pulse shaping techniques [121].

In this thesis, achievements of lasing in the first higher-order doughnut-shaped mode (LP_{11} mode group) in few-moded Yb-doped fibre lasers are reported. Therefore, some fundamental backgrounds of transverse modes in optical fibres and the used mode conversion techniques are briefly described in the following subsections.

3.5.1 Transverse Modes in Optical Fibres

According to optical waveguide theory, the electric field vector $\vec{e_t}$ in an optical fibre obeying the vector wave equation is given by [3, 122]:

$$(\nabla_t^2 + n^2k^2 - \beta^2)\vec{e_t} = -\nabla_t[\vec{e_t} \cdot \nabla_t \ln(n^2)] \tag{3.24}$$

where ∇_t is the transverse gradient vector, ∇_t^2 is the transverse vector Laplacian, n is the refractive index of the fibre, k is the free-space wavenumber (given by $2\pi/\lambda$), and β is the propagation constant of each individual vector mode. In a weakly guided optical fibre where the refractive index difference (Δ) between core and cladding is small, the scalar wave equation can be derived by neglecting the index gradient (e.g. setting the right hand of Equation 3.24 equal to zero). The neglect of the index gradient in the right-hand-side of Equation 3.24 leads to polarisation-independent propagation, thereby allowing the choice of linearly polarised (LP) modes, or circularly polarised modes, as well as arbitrary linear combinations as possible solutions of Equation 3.24. However, by considering a finite value for Δ, coupling between orthogonally polarised LP modes will be introduced, and there is an increasing coupling between polarisation components with the increase of Δ, lending to transit to the TE, TM, HE and EH modes. Corresponding intensity distributions for the two lowest-order vector modes are shown in Figure 3.14 (a) with schematic representations of polarisation orientations.

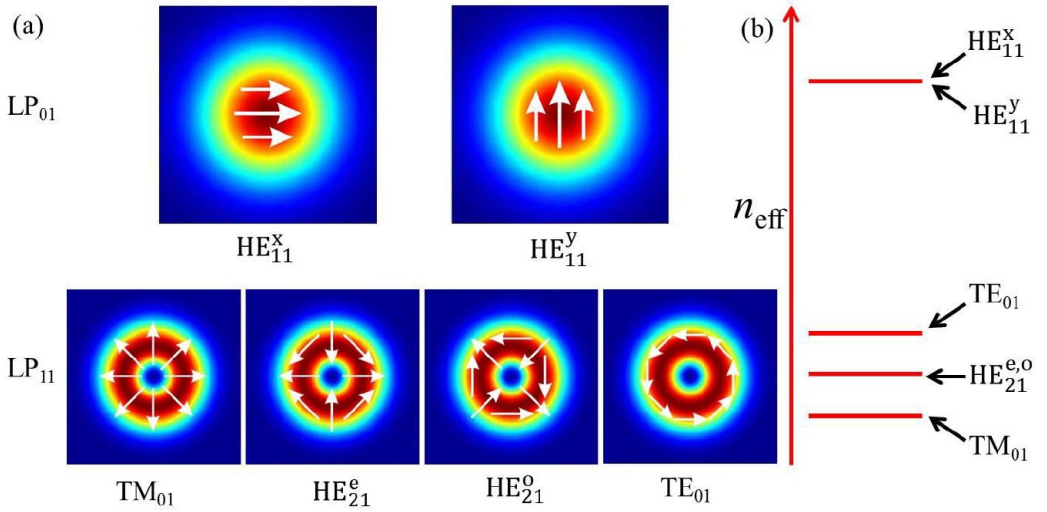

Figure 3.14: a) Intensity profiles of the fundamental (LP_{01}) and the first higher-order (LP_{11}) mode groups in a step-index fibre. White arrows show the orientation of electric field in each mode; b) relative n_{eff} for each vector mode [62].

Figure 3.14 (b) indicates relevant effective refractive index (n_{eff}) for each vector mode. For modes with azimuthal order l =0, LP_{0m} modes in the scalar approximations and HE_{1m} in the vector solutions, have two-fold degeneracies due to having exactly the same value for n_{eff} with orthogonal linear polarisation orientations. However, designated LP_{1m} modes in the scalar approximation can be generated by mixing four vector solutions, TE_{0m} (transverse electric field), TM_{0m} (transverse magnetic field), HE_{2m}^{even}, and HE_{2m}^{odd} modes in the appropriate ratios. The four modes present the same intensity distributions but with different polarisation orientations. Four vector modes, TE_{01}, TM_{01}, HE_{21}^{even} and HE_{21}^{odd}, comprising the lowest-order LP_{11} mode of LP_{1m} modes are shown in the bottom row of Figure 3.14 (a). Due to the same value of n_{eff}, the HE_{21}^{even} and HE_{21}^{odd} modes are degenerate. The TE_{01} mode with azimuthal polarisation distribution and TM_{01} mode with radial polarisation distribution have slightly different values for n_{eff} and are of the most interest in the application perspectives.

In a weakly guided fibre, the effective index differences of the four vector modes

TE_{01}, TM_{01}, HE_{21}^{even} and HE_{21}^{odd} are very small ($< 10^{-5}$), and consequently they are likely to couple with each other during propagation along the fibre. As a result two lobed structure beam profiles are mostly observed for the LP_{11} modes. Coupling of the modes increases as the differences in effective indices decreases [62, 123–125].

Figure 3.15 illustrates some examples of the linear pair combinations of eigen modes in LP_{11} group. The bottom row shows the linear combination of the four eigen vector modes with their intensity distribution and polarisation states are depicted at the top row. The polarisation orientations are orthogonal for the pair of TE_{01} and TM_{01} modes as well as for the pair of HE_{21}^{even} and HE_{21}^{odd} modes. Therefore, the combinations of these two pairs of modes result in a stable doughnut-shaped intensity distribution with varying polarisation states depending on their relative phase, while the combinations of other pairs of eigen modes form two-lobe structure intensity patterns. Yet, it should be considered that these patterns are unstable and the orientations rotate since they are formed by the interference of two eigen modes with slight different n_{eff} that periodically vary along the fibre length.

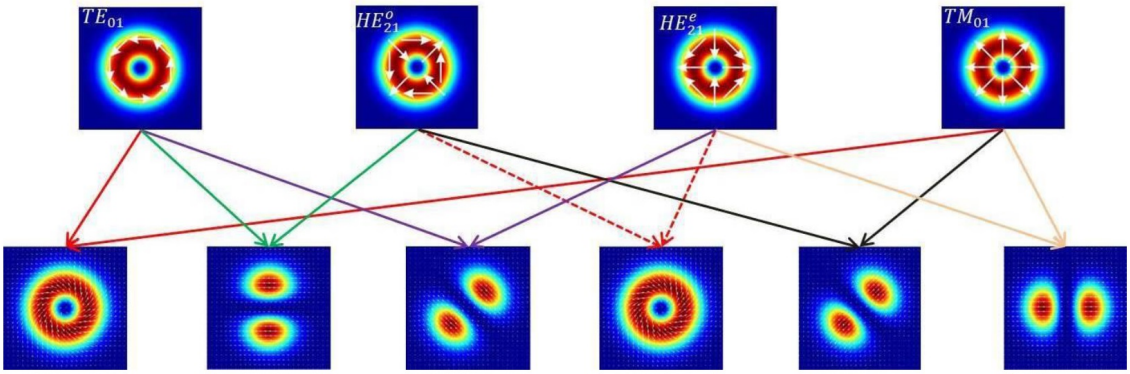

Figure 3.15: Intensity distributions of the first higher-order mode group in a weekly guided cylindrical fibre. The top row shows four eigen modes of fibre, while the bottom row shows specific combination of pairs of eigen modes, resulting in LP_{11} modes or doughnut-shaped beams, which are probably observed at fibre output. White arrows indicate the orientation of electric field in each beam [62].

From Figure 3.14, it appears that generation of doughnut-shaped modes such as azimuthally (TE_{01}) or radially (TM_{01}) polarised beams is feasible in few-moded fibres. However, the near-degeneracy of four modes in the LP_{11} group means the strict requirement of a robust mode discrimination to generate such cylindrical vector beams in fibres. In recent years, a number of techniques have been developed and applied to select doughnut-shaped modes in few-mode fibres. These investigations have been conducted predominantly in Yb-doped fibre lasers. Using an external mode converter is one of the most popular ways to transform a linearly-polarised TEM_{00} beam into radially or azimuthally polarised beam. Traditionally, these converters were constructed from liquid crystals [126–130] or from an arrangement of half-wave plates bonded together to form a segmented spatially variant retardation plate (SVR) [131]. Nevertheless, applying these converters result in low polarisation purity, degraded beam quality and low transformation efficiency. However, an improved performance is realised in [124] by applying a new type of radial polarisation converter (S-waveplate), achieved by writing nanostructure gratings in silica glass with a femtosecond laser [132]. Hence,

in the following section, this new type of radial polarisation converter is introduced and its demonstration is presented in chapter 4. Meanwhile, a liquid crystal based device called as ***q***-plate received a significant interest lately. Despite the low damage threshold of this device, low insertion loss in contrast to SVR plates encouraged users to use it for polarisation conversion. A brief description of ***q***-plate is provided in the next sections and then in chapter 5, its utilization in picosecond laser system is presented.

It is worth mentioning that due to the ∼1.2 dB insertion loss (75% mode-conversion efficiency) of the early generation of the S-waveplate and ∼2 dB coupling loss in MOPA systems, it has been placed before the final amplifier stage to convert the incident linearly polarised Gaussian-shaped beam into a radially-polarised doughnut-shaped beam (applied in nanosecond system, chapter 4). However, if there is not the aim to excite radial or azimuthal polarisation states in few-moded YDF, it can be placed after power amplification while the incident power level is carefully reduced maintaining the polarisation state (applied in the reported picosecond system in chapter 7). The latest generation of S-waveplates, demonstrated recently and after the ERM project working plan ([133]), have ultralow-losses and transmission efficiencies of ∼99% (close to the maximum theoretical value of ∼93% [134]), so they are suitable for placement after the final amplifier. Low damage threshold of the ***q***-plates doesn't make them appropriate to be applied directly after power amplification stage despite their lower insertion loss.

3.5.2 Spatially Variant Waveplate

As explained in the previous sub-section, quasi-continuous spatially variant waveplate can be achieved with liquid crystal. But this device suffers from temporal instability with regard to the orientation of the liquid-crystal molecules [135]. Also it has relatively low damage threshold (∼2 W/cm^2).

A new type of spatially variant waveplates (also called S-waveplate) based on nanostructured gratings fabricated by femtosecond laser writing in silica glass allow the operation from visible to near-infrared regions and with high incident powers. Two types of spatially variant waveplates are typically produced depending on the induced retardation. First kind is a half-waveplate that transforms a linearly polarised beam into radially or azimuthally polarised beam (Figure 3.16 (a)). The nanograting distributions in this waveplate induce birefringence with slow and fast axes aligned parallel and perpendicular to the grating direction respectively, which is aligned at an angle $\phi/2$ from the azimuthal angle ϕ to form a continuously spatially variant half-waveplate [136]. The second type is a quarter-waveplate as shown in Figure 3.16 (b) in which the directions of grating structures are aligned at an angle of $\phi - \pi/4$. The linearly polarised beam incident upon it will be converted into a beam with a helical phase front. It also converts circular polarisation to radial or azimuthal polarisation.

In this project we were interested to work with radial and azimuthal polarised beams where the linearly polarised state of incident beam is transformed to radial polarisation after passing through a $\lambda/2$ S-waveplate. An example of working principle for $\lambda/2$ S-waveplate is shown in Figure 3.17. A linearly-polarised Gaussian beam is transformed to a radially-polarised beam with doughnut-shaped intensity distribution in the far-field.

The experimental performance of $\lambda/2$ S-waveplate to generate radially/azimuthally-

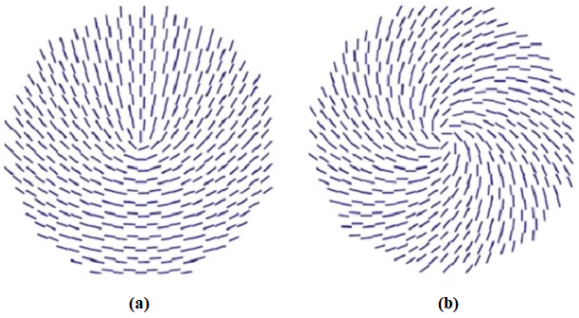

Figure 3.16: Schematic drawings of nanograting distributions in spatially variant a) half-waveplate and b) quarter-waveplate [137].

polarised beam with doughnut-shaped intensity distribution profile at high power MOPA system is explained in chapters 4 and 7.

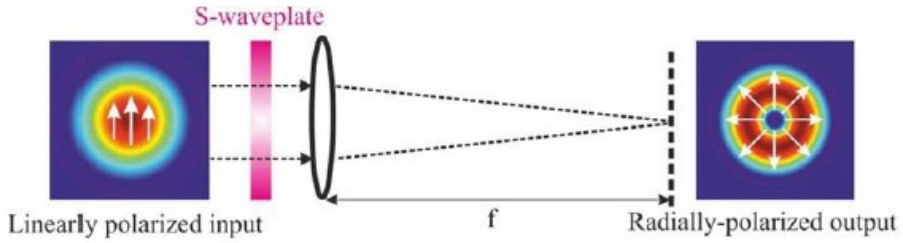

Figure 3.17: Principle of S-waveplate: Incident linearly-polarised beam is converted into radially-polarised beam in the far-field [62].

3.5.3 *Q*- Plate

Q-plates are well known liquid crystal based devices. The name originates from the mathematical symbol q denoted for peculiar singular pattern format [129, 130]. These are actually phase-plates, which couple spin angular momentum (SAM) and orbital angular momentum (OAM) of light when the sign of OAM is controlled by the input polarisation. The other type recognized with the same name is Vortex Retarders, which are half-wave retarders designed to affect the radial and azimuthal polarisation of optical fields. A vortex retarder has a constant retardant across the clear aperture but its fast axis rotates continuously over the area of the optic [128]. These plates are essentially a thin liquid crystal film sandwiched between two glasses, with a peculiar singular pattern of molecular alignment, obtained by suitable treatment of the containing glass surfaces in advance.

The low power handling limit of the ***q***-plates means applying them is only possible after the low power stages of a laser system. However, a very recent reported research ([138]) has described the fabrication and characterisation of ***q***-plates (phase-plates) made without liquid crystals making them an ideal candidate to use in high power laser sources or inside laser cavities. In comparison to S-waveplate, ***q***-plates result in lower insertion loss in the laser system, which promote their application for power scaling. The experimental performance of a ***q***-plate to generate radially-polarised beam with doughnut-shaped intensity distribution profile in high power picosecond MOPA system is explained in chapter 5.

3.6 Conclusion

A brief background of the fundamental and characteristics of Yb-doped MOPA laser systems as the applied system in this thesis described here. The power scaling challenges discussed and as the main purpose of the ERM project, techniques of spatial and temporal beam tailoring for both nanosecond and picosecond pulse regimes widely explained.

Chapter 4

Spatio-Temporal Shaping in Nanosecond Pulse Regime

High power and high energy spatial and temporal pulse shaping in a nanosecond pulsed fibre MOPA system has been investigated as the first part of the ERM project target. The preeminent radially and azimuthally polarised nanosecond Yb-doped fibre MOPA performance, incorporating temporal shaping, offered a fully-fiberised laser system for a variety of applications including materials processing is explained in this chapter. A brief review of the state-of-the-art and the implemented experimental laser setup alongside the detailed published results are presented in the following sections.

4.1 Introduction

Pulsed fibre MOPA systems have been extensively used to achieve high powers and moderate pulse energies beyond the limitations of traditional solid-state lasers (e.g. [26, 37, 38]) and challenged only by thin-disk lasers [5, 7–9]. However, a high power nanosecond pulsed fibre MOPA system suffers severe temporal distortion because of the gain saturation effect (section 3.4.1). For many industrial applications, a stable high peak power pulse with a square shape or featured temporal profiles are desirable and temporal pulse shaping should be carried out.

As discussed in chapter 3, MOPA setups are comprised of a seed laser followed by an optical amplifier chain. In order to execute a pulse re-shaping or pre-shaping procedure, different methods can be considered based on adaptive pulse shaping described in section 3.4.1. One of the methods is based on the direct modulation of the optical output of a seed laser using an electro-optic modulator (EOM) driven by an arbitrary waveform generator (AWG) for pre-shaping the pulse. The results are presented in [31–34] for square, triangular, and two-stepped shaped output pulses with 100 ns and 200 ns durations, respectively at different MOPA lasers and pulse energy range from 0.2-2 mJ with the signal wavelength peak close to 1070 nm. Another pulse shaping method is to use an acousto-optic modulator (AOM) to form the input pulse, which provides the control needed for tailoring the required output pulses [23, 80]. A minimum single peak pulse width of ∼30 ns has been measured at a pulse energy up to 1 mJ over a total pulse duration of ∼200 ns [80]. The response of the AOM (10-100 ns) is slower compared to the EOM, limiting the pulse shaping capability and may not be adequate for user defined output pulses, for instance a square shaped output pulse in a high gain system. However, an AOM can handle higher powers in contrast to an EOM

and benefits from a lower insertion loss characteristics helps in reducing the number of amplification stages in a MOPA structure.

With the improvements in laser diode driver manufacturing, some are now able to provide a faster response for temporal pulse shaping than an EOM. This enhancement helps us not only to get close to a fully-fiberised MOPA system, but also yields the possibility of operating the system with nanosecond pulses, leading to nanosecond pulse shaping with sub-nanosecond temporal features, desirable for laser system application in materials processing. Therefore, a first reported high energy nanosecond MOPA system seeded by a super luminescent diode (SLD) using direct electric modulation was built to generate radially polarised doughnut-shaped beam. The system incorporate a well-developed temporal shaping technique in the nanosecond regime via active pulse shaping at 25 kHz repetition rate. In contrast to previous published works of high power temporally and spatially shaping in fiberised MOPA ([104]), we demonstrated a power scaling approach, with the incident linearly polarised Gaussian beam was converted into a radially and azimuthally polarised beam prior to power amplifier. The doughnut-shaped intensity distribution was maintained through the active fibre of power amplifier stage. Furthermore, the MOPA was designed to operate at a centre wavelength of ∼1040 nm to further enhance the possibility of power scaling.

Our engineered version of this MOPA laser having been programmed for the desired temporal pulse profiles and with a spatial output in either Gaussian or radially polarised beam was delivered to University of Cambridge for material processing trials as part of the ERM project. Dr. Di Lin was leading the nanosecond beam tailoring part under Prof. D. J. Richardson supervision and I cooperated in building the entire setup and collecting the demonstrated data.

4.2 Experimental Procedure and Results

In the developed MOPA system, a directly modulated SLD with a broad output spectrum (FWHM≈ 20 nm) was used. In order to improve the signal fidelity and content, it was first amplified and a small fraction of spectral content sliced out by a fibre Bragg grating (FBG) with 3-dB bandwidth of 0.25 nm. This spectral splicing process results in ∼ 20 dB loss in optical power and the second amplifier was used to overcome the loss. Then, the signal is ready to go to the third amplifier stage to gain enough power level that can be used to seed the final amplifier (power amplifier) stage. Figure 4.1 illustrates a full schematic of the experimental setup that consists of a pulse shaper stage followed by 4-stage Yb-doped fibre amplifier chain. More details of the operating characteristic of each block are explained in the following sections. The overall laser performance developed in this project was proved by conducting some laser material processing trials at the University of Cambridge.

4.2.1 Seed Laser

The first block of the setup (i.e. the pulse shaper) is the master oscillator (MO) part of the MOPA and it consists of a seed laser driven by electronic drivers. The seed is a directly modulated SLD, which incorporates a pulse shaping mechanism through the use of a computer controlled arbitrary waveform generator (AWG, 7000-series) with a 12 GHz sampling rate and 10-bit amplitude resolution capable of adjusting pulse widths from 1ns to continuous-wave at a maximum repetition rate of 500 MHz.

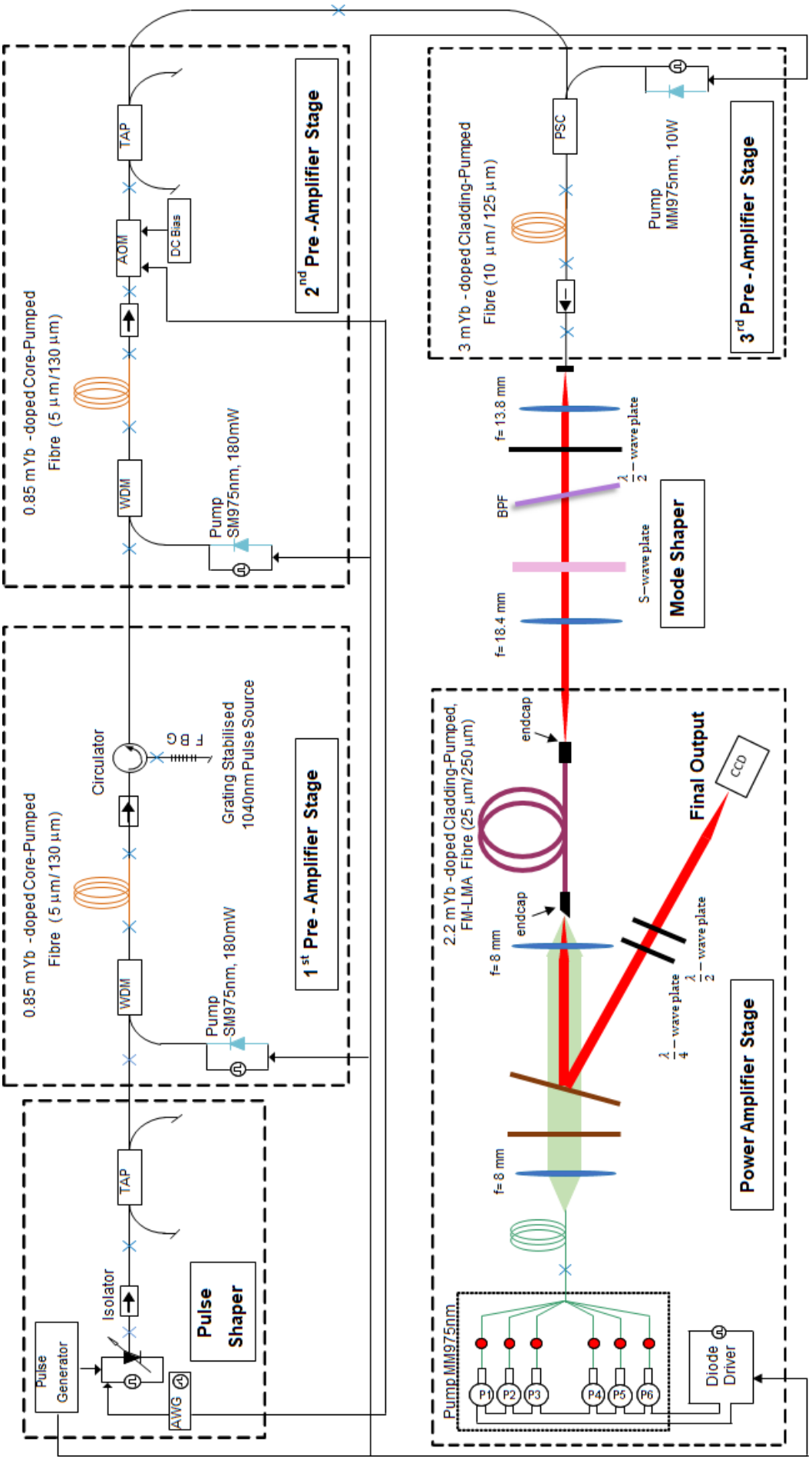

Figure 4.1: Schematic of nanosecond laser system.

For the seed laser source, DFBs or Fabry-Pérot laser sources can be considered but the narrow linewidth (e.g. 10 - 100 MHz) [110] can induce severe stimulated Brillouin scattering (SBS). Therefore, the SLD or superluminescent light emitting diodes (SLEDs) with a broader linewidth are preferred choice as a seed source in a fibre MOPA system. They are similar to laser diodes (LDs), which are based on an electrically driven pn-junction that becomes optically active as it is biased in the forward direction. They function by generating high single pass amplified spontaneous emission (ASE) over a wide range of wavelengths. Unlike laser diodes either the optical feedback is not sufficient for any lasing action or they are especially designed to be insensitive to optical feedback. Therefore, formation of resonator modes and having a narrow optical spectrum is avoided. This can be obtained by the joint action of a tilted waveguide and anti-reflection coated facets. High gain factors of 30 dB or more are the key to amplifying the seeded spontaneous emission in the SLDs.

The SLD (Innolume SLD-1030-20-YY-150) used in our experiment is a fibre pigtailed device with a central wavelength of 1030 nm and 3-dB bandwidth of ∼20 nm. Performance of the SLD has been tested before its application as the seed of the MOPA system. At first, the CW operation at 25°C with a simple room temperature heatsink mount was implemented, which perfectly matched with its specification. The power-current (P-I) curve is shown in Figure 4.2 (a) with a maximum power of 155 mW for 800 mA operating current. The optical spectrum was also measured and presented in Figure 4.2 (b) at several different current levels.

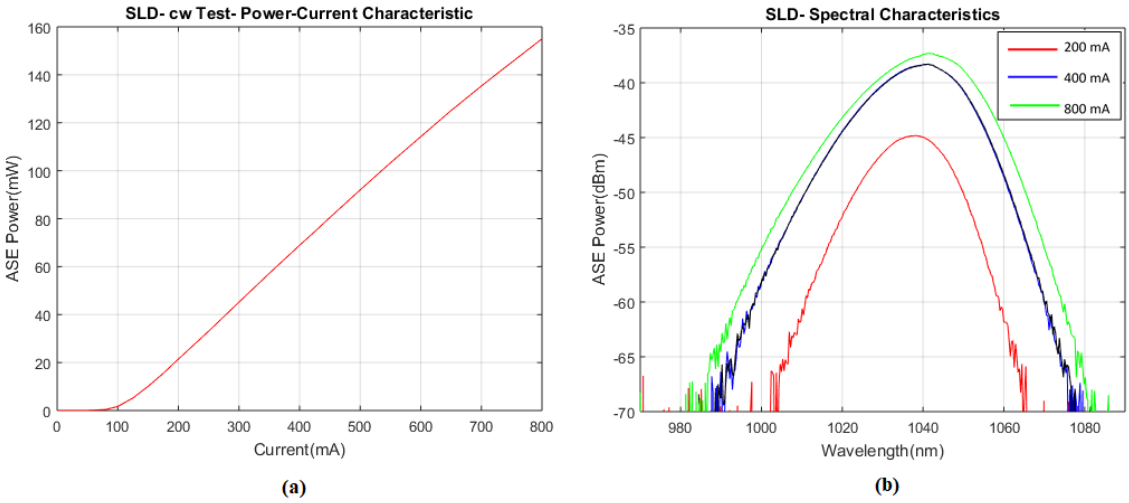

Figure 4.2: a) Power- current characteristic, b) Spectral characteristics of SLD with CW test.

Before mounting the SLD on the pulse laser diode driver, some tests were implemented to check the feasibility of reducing the complexity of the setup (i.e. to check the possibility of reduced number of amplifier stages). The idea of stabilising the SLD with a FBG at 1040 nm centre wavelength was investigated.

Two configurations were implemented as illustrated in Figure 4.3 and for each of them the output ASE power was measured at different current levels from 0 to 800 mA (Figure 4.4). For the first configuration, the SLD was stabilised with a direct connection to a FBG with $10\% < R < 15\%$ reflectivity. The output power from SLD (green line in Figure 4.4) experiences significant power drop (∼9 dB) compared to the SLD itself

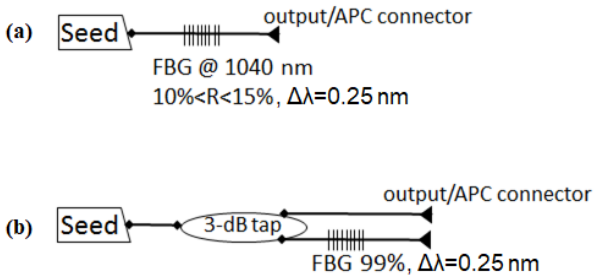

Figure 4.3: SLD stabilisation with a) a direct connection to one FBG with 10% reflectivity, b) 99% reflectivity FBG through a 3-dB coupler resulting in an effective ∼25% feedback fraction.

without any FBG (red line). This reduced output power may be due to the insufficient reflection feedback. Instead a 99% reflectivity FBG was connected with a 3-dB coupler in a second configuration in Figure 4.3 (b). This configuration was considered as it can increase the loss level inside the cavity and from the theoretical point of view should increase the output power from the other port of the tap. However, the measured output power, depicted a similar range of power loss as in the first configuration.

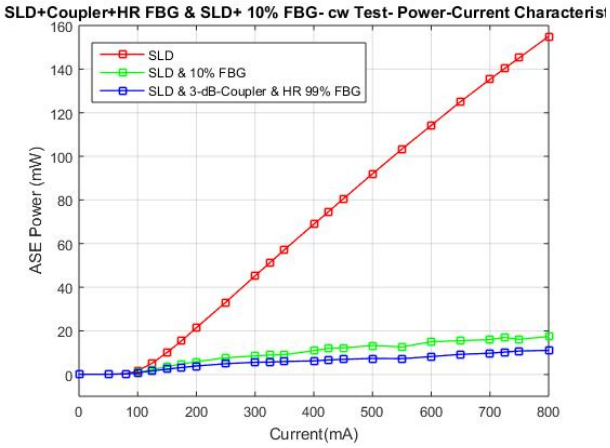

Figure 4.4: Comparison of ASE power density- current characteristics of SLD (red line), SLD stabilised by 10% reflectivity FBG (green line) and by 99% reflectivity FBG through a 3-dB coupler connection (blue line).

Next, the SLD without FBG feedback was connected to the pulse laser diode driver (MWTechnologies, PSLD-A model) for pulsed measurements. Being one of the required pulses for the further measurements, a square pulse shape with 100 ns pulse duration and 100 kHz repetition rate was produced by the AWG. The output power and spectral characteristics of the SLD itself were recorded, respectively for different signal voltage levels corresponding to the range of operating currents of the SLD (Figure 4.5). Running the diode beyond 500 mV, gain saturation in the temporal output pulse shape and in the power- voltage (P-V) characteristic curve were observed. Therefore, the measurements were continued without going beyond that level of signal voltage.

Subsequently, the pulsed measurements for the configuration of a stabilised SLD using a 10% reflectivity FBG for a square 100 ns 100 kHz input pulse were evaluated. The maximum average output power was ∼250 μW. The optical output pulses at

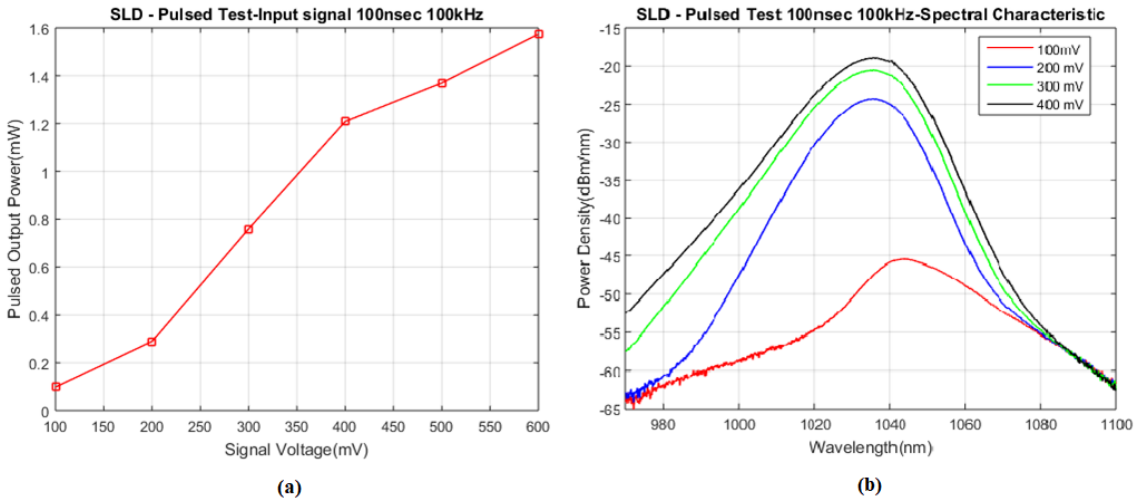

Figure 4.5: a) Power- signal voltage characteristic, b) Spectral characteristics of SLD in pulsed test by a square 100 ns 100 kHz input signal pulse shape at different signal voltage.

different power levels presented in Figure 4.6 (a), showing a sharp spike followed by multiple spikes rather than one single peak with a steady state tail, as the power increases. Each of the peaks has similar modulation period regardless of the power level and the peak amplitudes decays by propagation time. Therefore, we suspect it may be due to some feedback within the system. In the spectral domain (Figure 4.6 (b)), the wavelength stabilisation effect can be noticed as a lasing peak at the FBG wavelength of 1040nm. With the increase of the applied current, this lasing peak intensity grows slowly. However, the OSNR of the spectrum is not high enough to achieve the required output power at the lasing wavelength and there was no effective gain to use a FBG stabilised setup here. Investigations of the output with different pulse shapes such as ramped input pulse shape and ramp-flat composition have been done to check any application possibility, while no cleaner pulses with enough gain could be achieved as we originally expected for the ultimate goals of pulse shaping. Therefore, we can not use the FBG stabilised setup and returned back to the original spectral slicing scheme with a FBG (Figure 4.1).

Then, the SLD was mounted on a faster commercial driver board (PicoLas, BFS-VRM 03 HP) and directly modulated using the AWG. In order to prevent backward ASE directed toward the seed laser, an optical PM-isolator was spliced directly after the SLD (PM fibre pigtailed) as well as one tap coupler to monitor the output pulses before being amplified at the first pre-amplifier stage (section 4.2.2). The same procedure (inserting optical isolator and tap coupler) was considered for each of the amplifier stages when I characterised the system by monitoring the pulses in terms of their power, pulse shape, and spectral content as they propagated from the diode to the output of the third pre-amplifier stage.

4.2.2 First Pre-amplifier Stage

The first pre-amplifier stage consists of an 85 cm long length of polarisation maintaining Yb-doped fibre (PM-YDF) that has a 5 μm core diameter with a numerical aperture (NA) of 0.12 and a 130 μm cladding diameter with an NA of 0.46 (Nufern PM-YDF-5/130-VIII). A 975nm single mode pump laser diode was employed to amplify the pulse with a

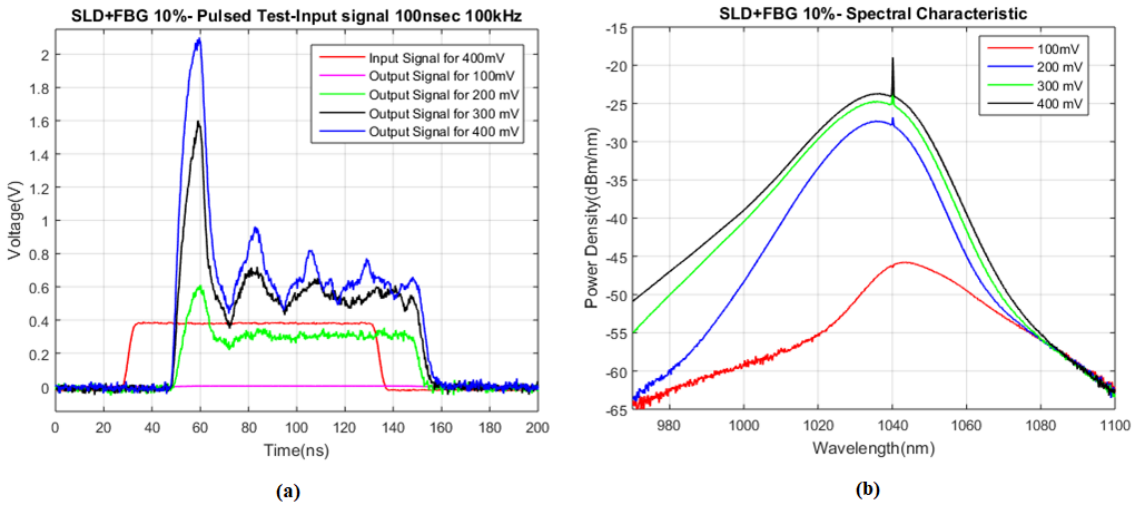

Figure 4.6: a) Temporal domain characteristics (output signals have been measured with a delay from input signal (red line) as there was no triggering between input and output at the time of measurement), b) Spectral domain characteristics of SLD stabilised configuration by a 10% reflectivity FBG in pulsed test by a square 100 ns 100 kHz input signal pulse shape at different signal voltage.

gain of ∼22 dB resulting in an average power of ∼14 mW in a forward core-pumped format with 180 mW pump power. Pump light was coupled into the fibre through a polarisation maintaining wavelength division multiplexer (PM-WDM). Then a uniform pitch fibre Bragg grating (FBG) at the centre wavelength of 1040 nm with a high reflectivity of $> 99\%$ and 3-dB bandwidth of 0.25 nm was inserted using a circulator after the first pre-amplifier stage. Figure 4.7 shows the seed spectrum monitored after the insertion of the FBG. Due to the spectral slicing as well as the circulator loss, a significant loss (∼20dB) was unavoidable. It is worth mentioning that since the FBG is not apodized, two main side peaks with ∼20 dB lower power density in respect to the main peak are visible. With that level of power density difference, they were assumed to have no severe influence and contribution to the output beam.

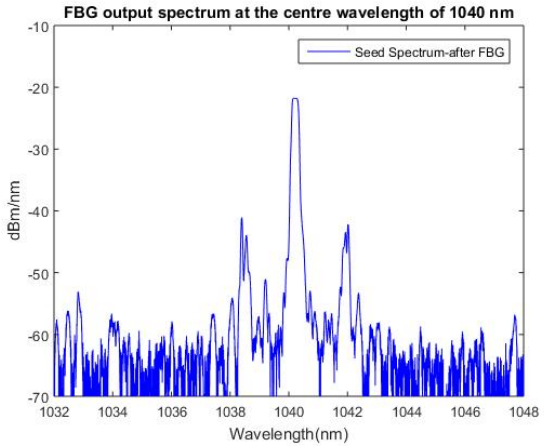

Figure 4.7: Seed spectrum after the fibre Bragg grating (FBG). Centre wavelength 1040 nm.

Since our target is materials processing, we are interested in a pulsed fibre laser

with few tens of ns pulse width and few tens of kHz repetition rate. First of all, some measurements have been done with a 100 ns pulse at 25 kHz repetition rate to seed the YDF amplifier chain, which are presented here and also published in the CLEO conference 2016 [123]. Then, other measurements for the two pre-amplifier stages have been implemented as they are seeded by different duration square pulse shapes with duration of 10, 25, 50 and 100 ns each at 10, 25, 50 and 100 kHz repetition rates. The output power (after the circulator) and gain (before the circulator) of the first pre-amplifier regarding the seed power of each of the pulses are presented in the Figure 4.8.

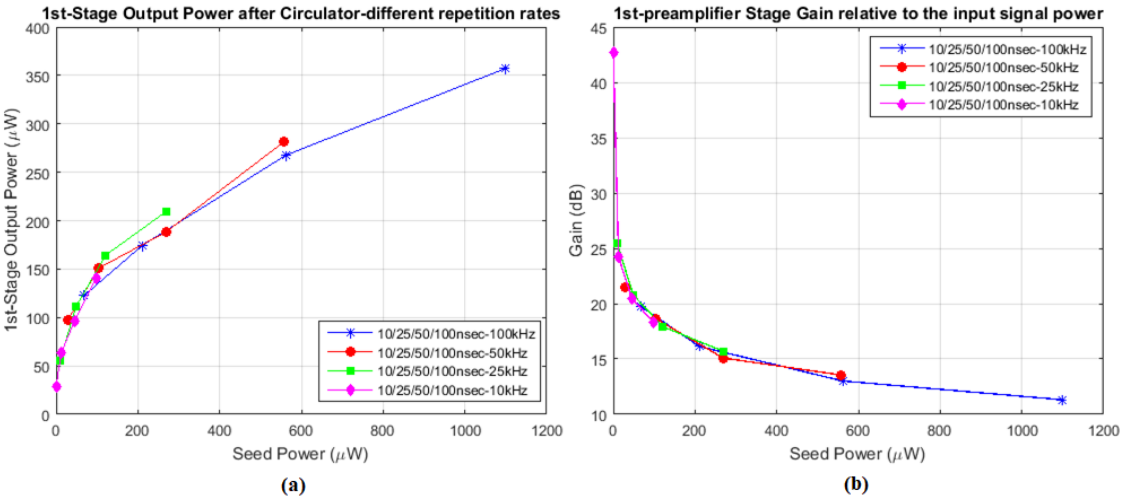

Figure 4.8: a) Output power of the first pre-amplifier stage, after circulator, b) gain of the first pre-amplifier stage measured before circulator for 10, 25, 50 and 100 ns input pulses at 10, 25, 50 and 100 kHz repetition rates (before insertion of an isolator before circulator), both versus seed power of each of the pulses.

For completeness, at the technical level, I note that after monitoring the temporal output signal of the seed from the tap coupler, we noticed that the back reflection peak appears on the seed output signal as soon as the first pre-amplifier stage is turned on. The back reflection peak was more obvious for the shorter pulses with lower repetition rates, such as 10 ns pulses at 10 kHz repetition rate. We believe that the backward signal was amplified through the amplification process in the first pre-amplifier stage. Therefore, another isolator was inserted in our setup between the amplifier output and input of the circulator to suppress any further back reflection after the SLD. However, all the results that are demonstrated in this chapter are before insertion of this extra optical isolator in the setup except Figure 4.11 due to the unavailability of the measured data before isolator insertion for those spectra.

4.2.3 Second Pre-amplifier Stage

The second pre-amplifier stage has a similar configuration to the first pre-amplifier but was designed to amplify the spectrally sliced pulses up to an average power of ∼18 mW, compensating the ∼20 dB total insertion loss of the FBG.

It is worth mentioning that the first version of amplifier chain up to first three stages initially had high content of ASE in the output beam. Therefore, a fibre pigtailed AOM was used for pulse picking and to remove the ASE between pulses after the

second pre-amplifier stage. More details of the observed ASE in the spectrum and how the AOM can remove this from the output beam is explained in the third pre-amplifier section. The insertion of the AOM has resulted in reducing the average power to ∼12 mW (from ∼18 mW without the AOM). The results shown in this sub-section are taken after insertion of the AOM.

Similar to the first stage, the output of the second pre-amplifer stage has been monitored for temporal and spectral pulse characterisations for several duration of square shaped input pulses. Figures 4.9 and 4.10 depict the output power and gain of the second pre-amplifier stage for several different pulse widths and repetition rates. As expected, an increase of the repetition rate results in a higher average power for each pulse width.

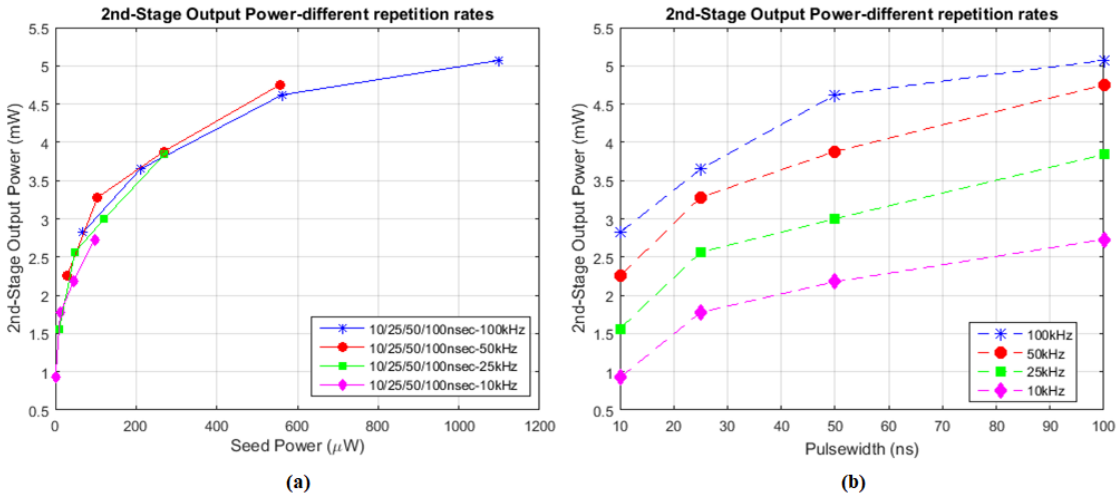

Figure 4.9: Output power of the second pre-amplifier stage a) versus seed power of 10, 25, 50 and 100 ns input pulses at 10, 25, 50 and 100 kHz repetition rates, b) versus 10, 25, 50 and 100 ns input pulse widths, respectively, for different repetition rates.

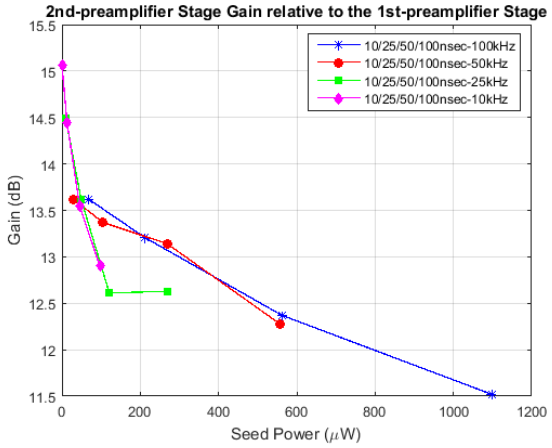

Figure 4.10: Gain of the second pre-amplifier stage measured for 10, 25, 50 and 100 ns input pulses at 10, 25, 50 and 100 kHz repetition rates relative to the output power of the first pre-amplifier stage versus seed power of each of the pulses.

A comparison of the first and second amplifier stage spectra is presented in Figure 4.11 at two different pulse definitions (100 ns pulse width at 25 kHz repetition rate and 10 ns pulse width at 10 kHz repetition rate). Due to higher repetition rate of 25 kHz and longer pulse width of 100 ns in comparison to 10 kHz example, a higher power density level of ∼10 dB can be observed in Figure 4.11 (a). The OSNR difference of the both pre-amplifier stages at the slicing central wavelength shows ∼20 dB gain after the second stage for both of the tested pulses. These spectral side lobes were filtered out after the third pre-amplifier stage with the use of a bandpass filter (BPF) as discussed in the next section.

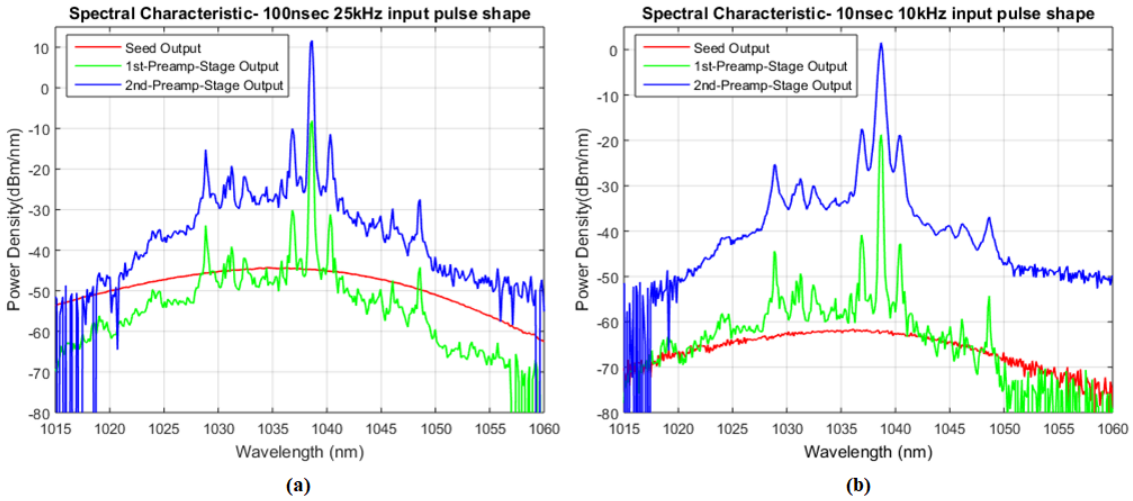

Figure 4.11: Spectral characteristics of the first pre-amplifier and second pre-amplifier stage output for a) 100 ns 25 kHz , b) 10 ns 10 kHz input pulses (after insertion of an isolator before the circulator).

4.2.4 Third Pre-amplifier Stage

The third pre-amplifier consists of a 3 m long dual-clad PM-YDF (Nufern PLMA-YDF-10/125-VIII) with a core diameter of 10 μm (core NA= 0.075) and a cladding diameter of 125 μm (cladding NA=0.46). This amplifier stage was cladding pumped with a 975 nm multimode pigtailed laser diode in the forward direction. High refractive index polymer is used at the output section of the Yb fibre to strip out the cladding modes and hence to leak out the unabsorbed pump from the fibre. A low index polymer is applied at the input splice point between a pump/signal combiner (PSC) and the Yb-doped fibre to transfer the pump light into the active fibre and a piece of copper tape was added to provide better heat dissipation at the splice point. The output of the third pre-amplifier stage was characterised following the angle-cleaved pigtailed fibre of the output isolator (∼1.6 dB insertion loss) that was spliced after the Yb fibre. The gain is shown in Figure 4.12.

Spectral characteristics of this stage are shown in Figure 4.13 at several different pump powers. With increasing the pump power, the ASE increases and SRS starts to appear at output power of ∼1.38 W, which limits power scaling. Therefore, a free-space bandpass filter (BPF) with a 3-dB bandwidth of 4 nm was inserted after the third pre-amplifier not only to remove any excess ASE from the output, but also to filter out the Raman scattering peak. A linearly polarised Gaussian-shaped spatial beam with a pulse

energy of ∼11 μJ (∼ 280 mW output power) and a polarisation extinction ratio (PER) of >20 dB has been attained for 100 ns input pulses at 25 kHz repetition rate measured after BPF.

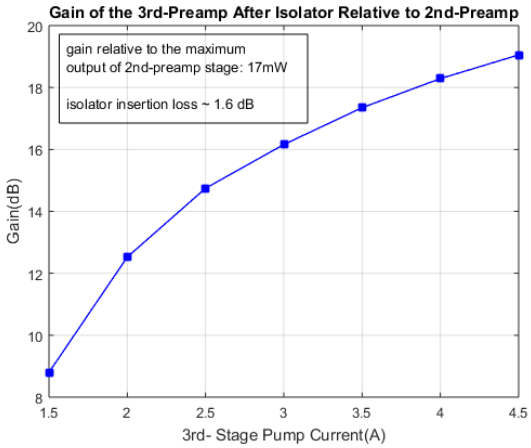

Figure 4.12: Gain of the third pre-amplifier stage measured after the isolator relative to the maximum output power of the second pre-amplifier (∼17mW). Fibre was angle-cleaved.

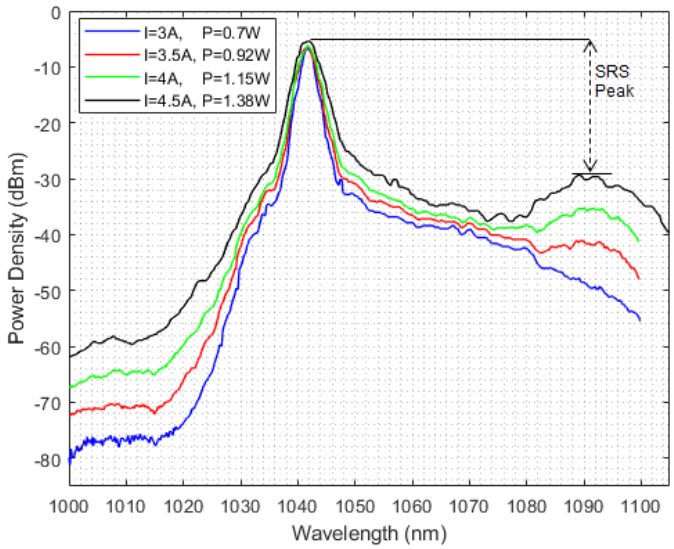

Figure 4.13: Spectral characteristics of the third pre-amplifier stage for different power levels of the pumping power level. Fibre was angle-cleaved.

4.2.5 Power Amplifier Stage

The final amplifier comprises a 2.2 m long few-mode YDF (Liekki Yb1200-25/250) with a core diameter of 25 μm (core NA=0.075), and an inner cladding diameter of 250 μm (cladding NA=0.46). The V-number of the YDF at 1040nm is ∼5.28 (supporting around ∼14 modes) and thus it supports both radially polarised (TM_{01}) and azimuthally polarised (TE_{01}) modes. It is worth mentioning that first a fibre length of 2.5 m was employed and then reduced to decrease the nonlinearities. The pump beam was provided by a chain of fibre-coupled 974.8 nm laser diodes, which were free-space

coupled into the YDF in a counter-pumped configuration. The pump absorption was measured to be $\sim$ 92%. Both ends of the fibre were spliced to endcaps with a diameter of 250 μm and a length of $\sim$1.5 mm to suppress parasitic oscillations and to prevent optical damage at the air-silica interface. The input end facet was flat-cleaved, and the output end facet was angle-cleaved with an angle of $\sim$8 degree. The flat-cleaved end facet at the input side of the fibre ensures the radially polarised doughnut-shaped beam could be coupled into the fibre core without any spatial distortion.

A $\frac{\lambda}{2}$- waveplate and a spatially variant waveplate (S-waveplate) were placed before the final amplifier to convert the incident linearly polarised Gaussian-shaped beam into a radially polarised doughnut-shaped beam. This spatially shaped beam was then coupled into the few-mode YDF (the FM-LMA fibre in Figure 4.1) to excite the TM_{01} mode. The measured input power to the final amplifier before and after the beam shaping optics and the BPF is presented in Figure 4.14.

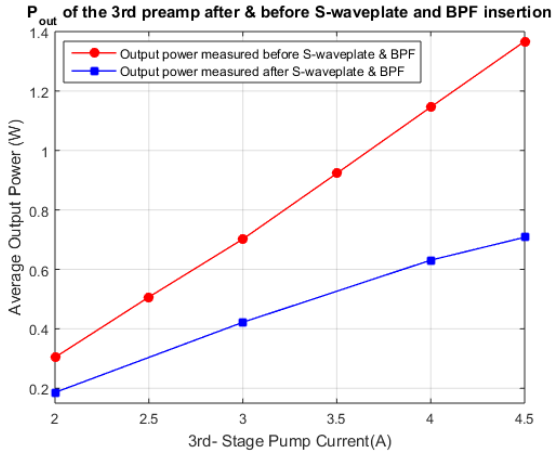

Figure 4.14: Comparison of the input power launched to the final amplifier stage before (red line) and after (blue line) the spatial mode shaping optics and the BPF.

With an insertion loss of $\sim$1.2 dB of the S-waveplate and a coupling loss of $\sim$2 dB to the final stage amplifier, we achieved a maximum coupled power of $\sim$140 mW ($\sim 5\mu$J) for radially polarised beam. However, due to the relatively small differences in effective refractive index ($<10^{-5}$) of the four vector modes (TM_{01}, TE_{01}, HE_{21}^{even} and HE_{21}^{odd} modes in the LP_{11} mode group) in weakly guiding standard circular core fibres, severe mode coupling can be expected even though care was taken that the fibre was only exposed to small perturbations (refer to subsection 3.5.1). The fibre was loosely coiled with a large bend diameter of $\sim$25 cm, and with minimized fibre twist.

The intensity distribution of the radially polarised doughnut-shaped output beam of the system was monitored using a CCD camera (Figure 4.15 (a)). The slight ellipticity of the beam profile apparent in that figure may be caused by a slightly curved surface of the angle-cleaved output end facet. Using a linear polariser with transmission axis at different angles aided angular analysis of the polarisation state of the doughnut-shaped output beam. In theory, the intensity distributions of a radially (or azimuthally) polarised beam after passing through a rotated linear polariser exhibit symmetric two-lobe features aligned either parallel or orthogonal to the transmission axis of the polariser. Intensity distribution of the output beam after passing through a rotated

linear polariser are shown in Figure 4.15 (b)-(e). White arrow indicates the orientation of the transmission axis of the polariser at 0, 45, 90, and 135 degrees.

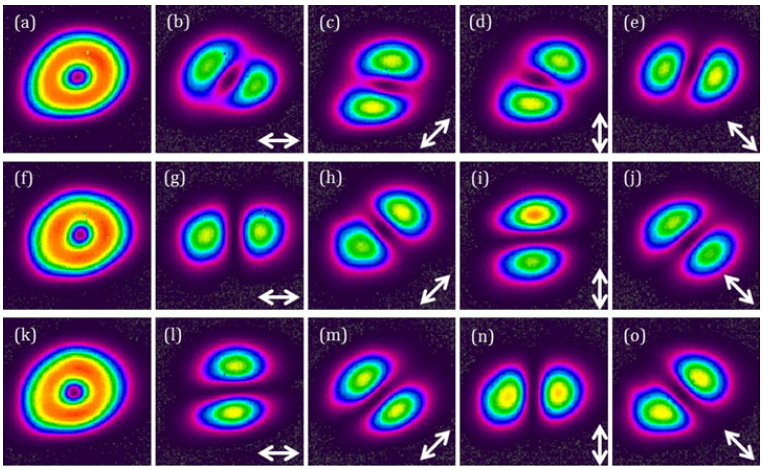

Figure 4.15: Experimentally observed intensity distributions of the original output beam (top row), the radially-polarised output beam (second row), and the azimuthally-polarised output beam (bottom row) at the maximum pulse energy of ~860 μJ. (a), (f) and (k) show total intensity profiles. (b)-(e), (g)-(j), and (l)-(o) show beam profiles after passing through a rotated linear polariser. The white arrows indicate the transmission axis of the polariser.

It can be obeserved that the axis of the two-lobe-structured intensity distribution is not parallel to the axis of the linear polariser, which indicates change in polarisation of the radially polarised input beam during amplification due to strong mode coupling between the four nearly-degenerate vector modes in the LP_{11} mode group. Residual birefringence of the fibre core is due to imperfection in the fibre fabrication process, any residual stress applied to the fibre core when coiling the fibre, and thermally induced variation of the refractive index of the fibre core may also lead to mode coupling. It is worth mentioning that the doughnut-shaped intensity distribution was well maintained while the polarisation state changed slightly with variation of the output power. The polarisation change could be successfully compensated (over extended operating periods) using a combination of a quarter-waveplate and half-waveplate. When the fast axes of the quarter-waveplate and half-waveplate were rotated to specific orientations, a radially polarised beam could be achieved as shown in Figure 4.15 (f). The symmetric two-lobe-structured intensity distributions parallel to the transmission axis of the linear polariser (shown in Figure 4.15 (g)-(j)) confirm that the resultant output was indeed a radially polarised beam. In addition, further rotating the fast axis of the half-waveplate by 45 degrees, yielded an azimuthally polarised beam as shown in Figure 4.15 (k). The azimuthal polarisation state verified through the symmetric two-lobe structured intensity distributions orthogonal to the transmission axis of the linear polariser (Figure 4.15 (l)-(o)). The beam quality factor (M^2) was measured to be approximately 2.2 at the maximum output power in close agreement with the theoretical value of 2 for a doughnut-shaped radially polarised TM_{01} mode.

It should be stated that the results in Figure 4.15 have been achieved after some improvements in the setup such as insertion of the AOM and reduction of the parasitic oscillations by re-doing the endcaps, which lead to a high pulse energy of ~860 μJ and published in Optics Letters [139].

We next moved on to incorporating temporal pulse shaping, at first with two-step pulses named as front peak decaying tail (FPDT) pulses expected to reveal a peak pulse duration of around 20 ns out of 100 ns full pulse duration. Therefore, a programmed square input pulse shape with 100 ns pulse duration at 25 kHz repetition rate transferred to the seed through AWG. Output pulse shapes and spectral characteristics of the output beam at the final stage regarding the launched pump to that stage are shown in Figure 4.16 (a) and (b), respectively. The 3-dB spectral bandwidth was broadened from ∼0.2nm (after the FBG, Figure 4.7) to ∼0.6 nm (at the output) due to self-phase modulation (SPM) induced by the high peak powers.

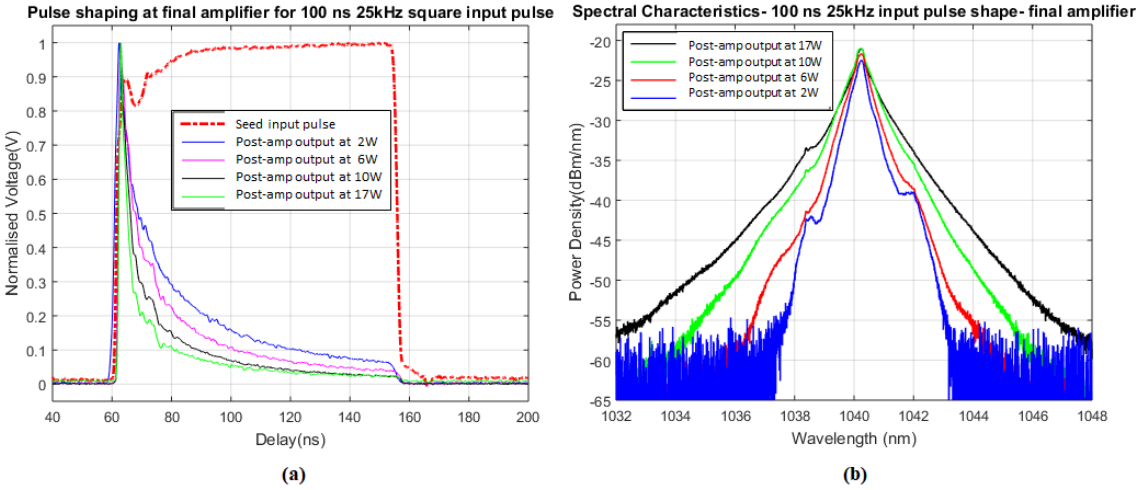

Figure 4.16: a) Temporal pulse shaping, b) Spectral analysis at final amplifier stage for a 100ns square input pulse shape at 25 kHz repetition rate.

The average output power and pulse energy of the doughnut-shaped beam as a function of pump power are presented in Figure 4.17. The maximum pulse energy was ∼580 μJ. The difference between the pulse energy and output power, which becomes larger at increased pump power, is due to the growth of ASE that restricted further power scaling. To investigate the presence of ASE content, we implemented a time resolved measurement, where some laser output was extracted by an acousto-optic modulator (AOM) as shown in Figure 4.18. This AOM was driven by a Stanford Research Systems pulse generator and was triggered by the signal from the seeding pulses. The AOM can be controlled to gate only the pulses or the ASE, which can be analysed by an optical spectrum analyser (OSA) and oscilloscope. An appropriately synchronised electrical signal pulse, which controls the RF signal supply, was turned on to deflect the optical pulse, the ASE signal or both. Here, a square electrical pulse shape with a window length that could include the signal was applied for deflection of the optical pulse. An inverted version of the square pulse was used to deflect the ASE while a constant DC signal was used to deflect both the signal and the ASE components of the output beam. The presence of ASE content was systematically verified. Therefore, a fibre pigtailed AOM was inserted after the second pre-amplifier stage and the maximum measured pulse energy increased to ∼700 μJ (Figure 4.19).

The next challenge was that the higher pump power resulted in parasitic lasing of the fundamental LP_{01} mode and this limited the maximum extractable pulse energy. Its effect is visible in the spectral characteristics of the final stage in Figure 4.20. This

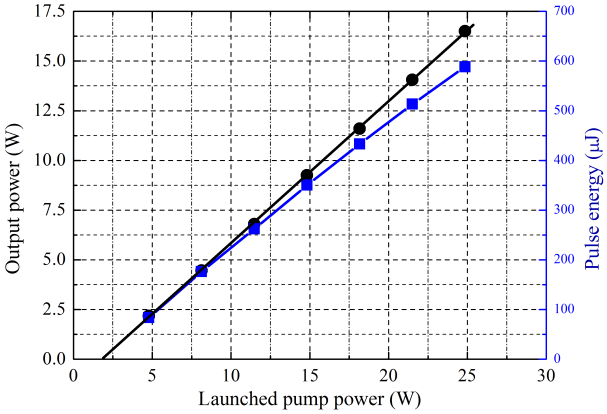

Figure 4.17: Output and pulse energy of the doughnut-shaped output beam as a function of the launched pump power to the final amplifier [123].

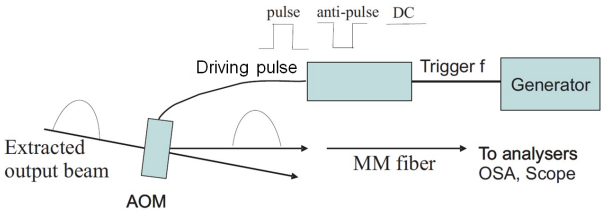

Figure 4.18: Set up to measure ASE using an AOM to separate the pulse and ASE content [32].

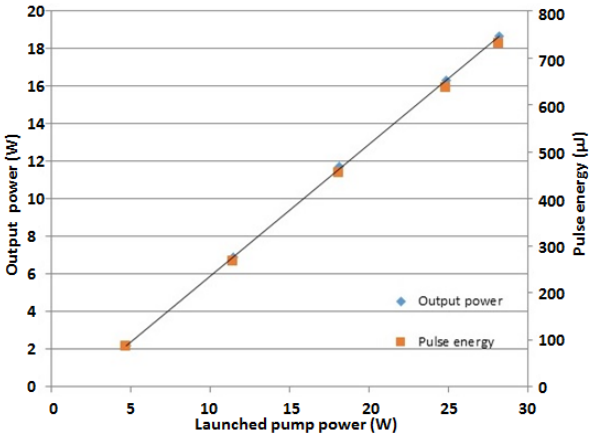

Figure 4.19: Average output power and pulse energy of the doughnut-shaped output beam as a function of the launched pump power to the final amplifier after the insertion of AOM.

parasitic lasing is attributed to residual feedback from the endcaps in conjunction with the high gain associated with undepleted population inversion at the centre of the fibre core due to the null in intensity for the doughnut-shaped beam.

In consequence, the endcaps were remade, resulted in a better endcap, to achieve high power scaling and we managed to reach the maximum power of 22.5 W with a slope efficiency of ~66%, respect to the launched pump power. The maximum pulse energy was then measured to be ~860 μJ with a relatively low ASE fraction, less than 5%, of the total output power (Figure 4.21). The gain of the final amplifier reached

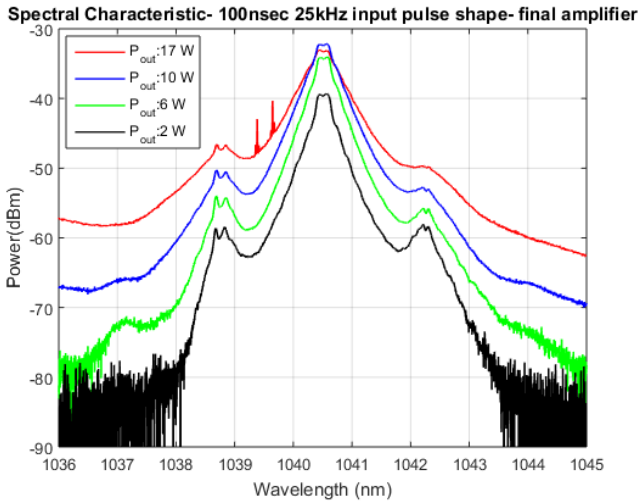

Figure 4.20: Spectral characteristics of the power amplifier stage showing onset of parasitic lasing.

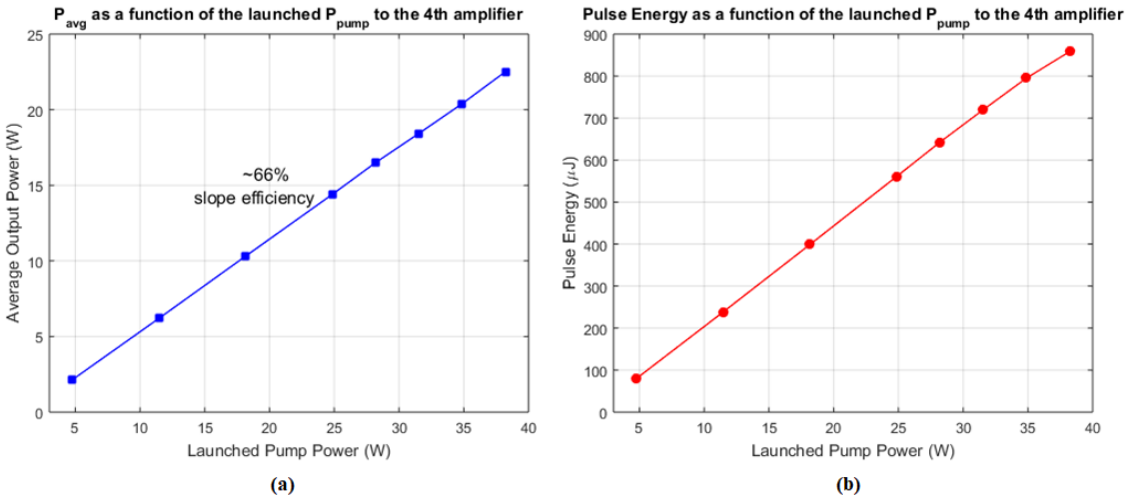

Figure 4.21: a) Average output power and b) Pulse energy of the doughnut-shaped output beam as a function of the launched pump power to the final amplifier.

∼22dB with an overall gain of ∼55 dB along the whole MOPA system. The spectral characteristics of the final stage are shown in Figure 4.22. There is a clear improvement in comparison to Figure 4.20.

In the next step, the length of the passive fibre of the isolator, after the third pre-amplifier stage, reduced by 4 times from ∼1 m pigtail length, which was expected to raise the Raman threshold by ∼4 times. In comparison to the Raman peak appearance in Figure 4.13, it can be seen that this peak becomes apparent at an OSNR>30 dB, in respect to the signal peak, in Figure 4.23 and the signal is less affected by SRS even in higher average output power level of 22.5 W.

Furthermore, the measured output power of the third pre-amplifier stage before and after the BPF, after reduction of the passive fibre length (Figure 4.24) depicts that almost same output power (∼99%) from the third stage can be delivered to the final stage and

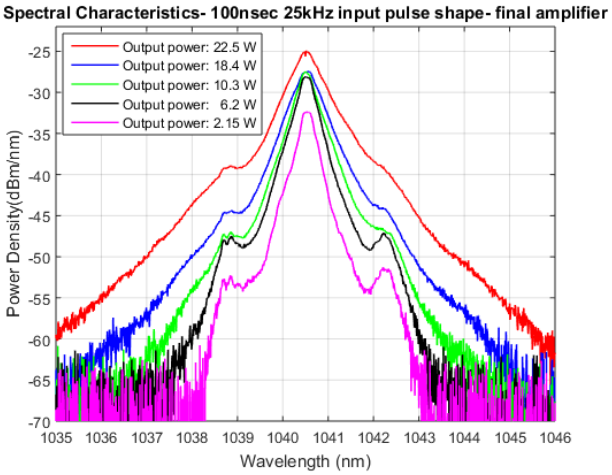

Figure 4.22: Spectral characteristics of the final amplifier stage after insertion of an AOM to reduce ASE and reduction of parasitic lasing by improving the endcaps.

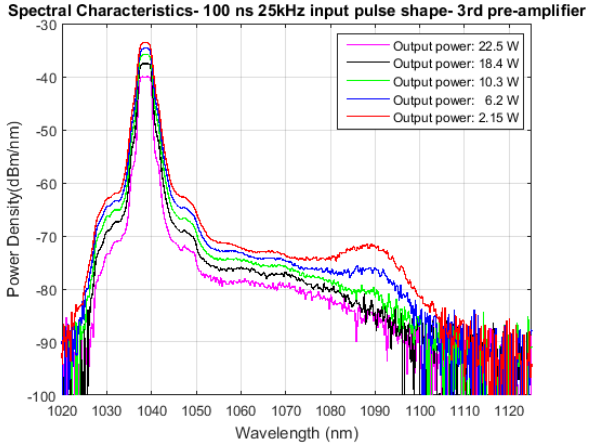

Figure 4.23: Spectral characteristics of the third pre-amplifier stage after reduction of the length of the passive fibre in the third stage, measured at 2 nm OSA resolution.

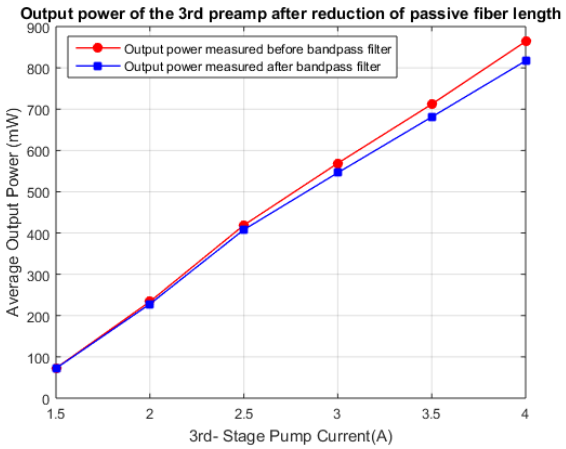

Figure 4.24: Measured output power of the third pre-amplifier stage before and after the BPF, after reduction the length of the passive fibre in that stage.

for amplification.

4.3 Overall Performance of System

A nanosecond pulse regime MOPA system was successfully developed. Figure 4.25 shows a photo of the actual setup, which depicts an integrated laser system for desired applications. As explained in the previous section a maximum average output power of 22.5 W was produced with a maximum pulse energy of ~860 μJ for a 100 ns pulse duration at 25 kHz repetition rate.

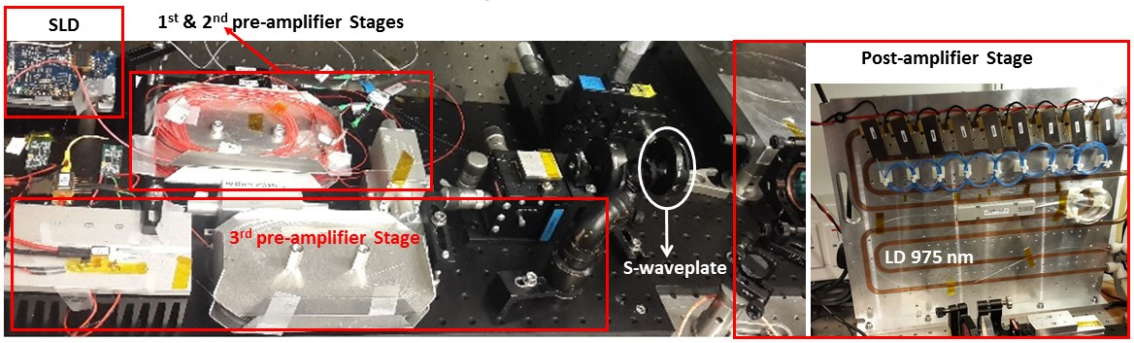

Figure 4.25: Photos of actual setup.

Performance of the setup in the spatial domain was investigated before providing the laser system for the materials processing trials to the project partner at the Institute for Manufacturing (IfM), University of Cambridge. Two-step pulse shapes have been previously shown to be advantageous in machining materials such as silicon [25, 35]. Hence, such a pulse shape was generated, examples of which with the same overall duration of 94 ns are shown in Figure 4.26. The pulse energy of ~860 μJ was distributed differently between the two steps within each pulse of both pulse shapes. The first shaped pulse comprised a 6.4 ns full width at half maximum (FWHM) leading peak, provided a 39 kW peak power pulse followed by 87 ns tail with 7 kW peak power. While the second configuration provides a 26 kW peak power maintained for 14 ns in the leading peak, followed by 6 kW for the 80 ns tail. After full characterisation of the spatio-temporal pulse shaping laser system in the nanosecond regime, the source is ready to be applied for materials processing tests.

4.4 Pulse Tailoring Application: Materials Processing in Collaboration with Cambridge University

The objective of this laser was to investigate material removal mechanisms of titanium (Ti64), silicon $< 1|1|1 >$, steel and aluminum using a variety of pulse shapes and spatial profiles. For the trial attempts on the mentioned materials, a two-step pulse shape with the peak intensity of $\geq$10 kW and ~300 W energy bridge was desired. The laser was launched into the optical beam delivery setup of a pulsed digital holographic interferometry system ([25]) while the influence of polarisation and spatial profile were inspected in comparison with a Gaussian beam.

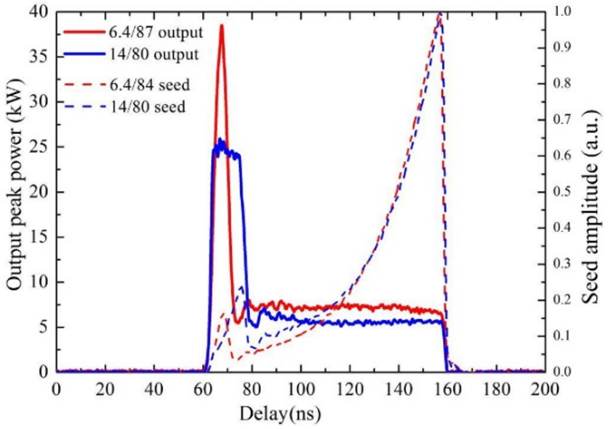

Figure 4.26: Normalized pulse shapes after the SLD (dashed lines) and the corresponding output peak powers (solid lines) for two different 2-step pulses.

In those trials 1 - 50 pulses were delivered to samples at 25 kHz repetition rate. Volumetric ablation rates and crater depth were measured, and energy cost differences were calculated (by the project partner). Post-process scanning electron microscope (SEM) analysis was undertaken at the University of Cambridge. As an example, achieved results for steel sample materials are presented in Figures 4.27.

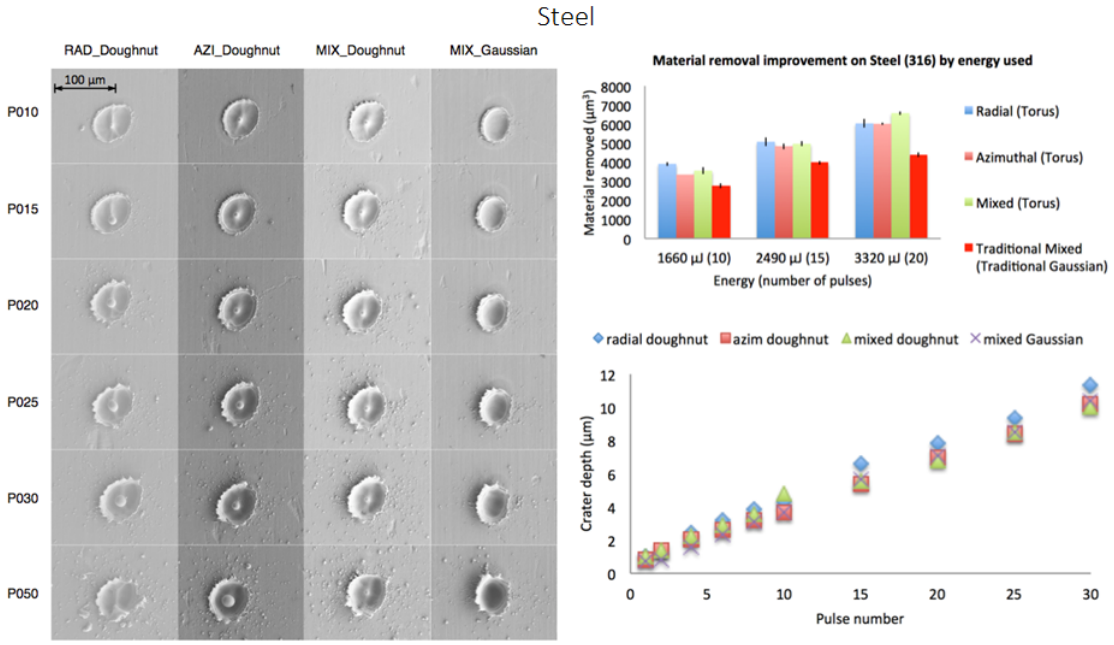

Figure 4.27: Material removal improvement in μm^3 and crater depth (μm) for steel(316) material sample under test as a function of pulse energy and pulse number with single peak pulse shape and radial, azimuthal and Gaussian spatial beam profiles. Results are from project collaborator.

Results show that a maximum volume of removed material of the order of $\sim$5000 μm^3 can be yielded while radial or azimuthal spatial profiles are applied in comparison to a maximum $\sim$4000 μm^3 in Gaussian mode trials when higher pulse energy was used. Also, a maximum crater depth of $\sim$11 μm can be achieved for steel samples, which increases linearly with pulse energy, specially for radial polarised pulses. Tailoring the pulse spatial

profile clearly enabled control of the ablation crater.

4.5 Conclusion

In conclusion, we have demonstrated for the first time a directly modulated SLD seeded YDF MOPA system with spatial and temporal pulse-shaping capability. ~860 μJ nanosecond pulses at a repetition rate of 25 kHz with user-defined temporal pulse shapes, as well as radially and azimuthally polarised doughnut-shaped beams, have been achieved. Such a spatially and temporally flexible laser source is expected to be applied as a fully-fiberised laser source, enabling a variety of laser materials processing applications with greater speed and precision than with conventional nanosecond lasers and Gaussian output beams and typically at lower pulse energies.

The laser was packed and delivered to the university of Cambridge for further materials processing trails.

Chapter 5

High Power Spatial Shaping in Picosecond Pulse MOPA Using a Gain-Switched Laser Source

Unprecedented generation of high average output power, high peak power, and high pulse energy radially polarised picosecond pulses from a compact gain-switched laser-diode-seeded fully-fiberised Yb-doped MOPA system is reported in this chapter. This laser was developed as the next step of the ERM project for materials processing applications by our project partner at the University of Cambridge, particularly to execute expected high quality polishing experiments. A linearly polarised Gaussian-shaped beam is efficiently converted into a doughnut-shaped radially polarised beam prior to the final power amplifier with the aid of a ***q***-plate. The experimental setup and reported spatial shaping and power scaling achievements are elucidated in the following sections after a brief review of the state-of-the-art.

5.1 Introduction

Polarisation as the vector nature of the light and one important property of it has attracted great interest in recent years for light:matter interactions, especially the laser beams with cylindrical symmetry in polarisation [140]. The so-called cylindrical vector beams (CVBs) benefits from the axially symmetric field amplitude distributions and radial or azimuthal polarisation states have shown a wide range of developments in a variety of applications including optical trapping [141–144], high resolution imaging [145], and material processing [22, 51–53]. High power cylindrically polarised laser beams have presented an increased cutting efficiency with a significant reduction of material spatter in deep-welding and more efficient microhole drilling in better machining quality [53]. The direct generation of CVBs under both CW and pulsed operation at average powers exceeding 100 W has been recently demonstrated from a CO_2 laser [146], Nd:YAG rod amplifier [147], thin-disk multipass amplifier [148], and a single crystal fibre amplifier [149].

Efficient generation of CVBs from Yb-doped fibre lasers and amplifiers (based on few mode YDFs) by employing a S-waveplate in the laser cavity/amplifier chain at several tens of watts of average output power in both CW and pulsed modes have been demonstrated in ORC [50, 124, 125, 139]. A gain-switched diode-seeded YDF based MOPA architecture, which has previously been demonstrated to provide a compact and

robust approach to amplify picosecond pulses to the hundreds of watts of average output power level with diffraction-limited beam [90], represents a promising way to generate high-performance, high-power CVBs in the picosecond regime to be applied in materials processing investigations. Therefore, an in-house built self-seeded gain-switched laser diode source produces ∼150 ps pulses at 1034.7 nm with a 3-dB spectral bandwidth of 0.03 nm at a pulse energy of ∼4 pJ with 87.5 MHz repetition rate, was chosen to seed a Yb-doped fibre MOPA to scale up the output power of the polarised beam to in excess of 100W.

At first, performance of the self-seeded gain-switched diode laser source was investigated as a non transform-limited optical pulse generator. Then, the MOPA chain was built and a ***q***-plate was used to convert the linearly polarised Gaussian beam into doughnut-shaped radially polarised beam. A fibre pigtailed electro-optic modulator (EOM) was applied as a pulse picker to reduce the repetition rate to 1.367 MHz. Finally, the desired vector beam was efficiently amplified, yielding ∼110 ps pulses with a maximum output pulse energy of ∼30.7 μJ and peak power of ∼280 kW. The average power was scaled up to 106 W by increasing the repetition rate to 5.468 MHz (published in Optics Letters [150]) and the laser delivered to University of Cambridge to explore its efficiency on the surface quality enhancement in materials polishing.

It is worth mentioning that originally it was the idea to use the SPM effects to broaden pulse for temporal pulse shaping. Attempts were unsuccessful, therefore, we focused on spatial beam shaping and power scaling approaches. However, I followed the aim of simultaneous spatial and temporal picosecond pulse shaping with another setup using a WaveShaper (subsection 3.4.2.1), as explained in the next two chapters.

The principle of gain-switching as a convenient and simple method to generate picosecond pulses, and details of the achievements are explained in the following sections. Dr. Lin was leading the spatial beam shaping and power scaling sections and I contributed in MOPA development and data collection.

5.2 Gain-Switching

Short optical pulses with pulse width less than 50 ps can be generated by "gain switching" technique in which a diode laser is driven with a short electrical pulse such that it results in the excitation of the first spike of a typical relaxation oscillation and terminates before the onset of the second optical spike. Therefore, very short optical pulses can be generated with this simple technique, whose widths are considerably shorter than the injected electrical pulse [151]. However, the resulting pulse width range is restricted due to the difficulty in sustaining a large initial inversion before stimulated emission [152]. Evolution in the photon and electron densities during a gain switch cycle is illustrated in Figure 5.1 [152].

At t=0 a current pulse is injected to the semiconductor laser when it is suitably biased below threshold. The gain and photon density are usually very low initially, but the carrier density builds up rapidly to a level where the gain exceeds the lasing threshold. The limited lifetime of the electron-hole pairs initiates a cascade of photons and a sharp depletion in the carrier density. Once the electrical current is stopped, the carrier density cannot be replenished, resulting in a decay of the photon density and

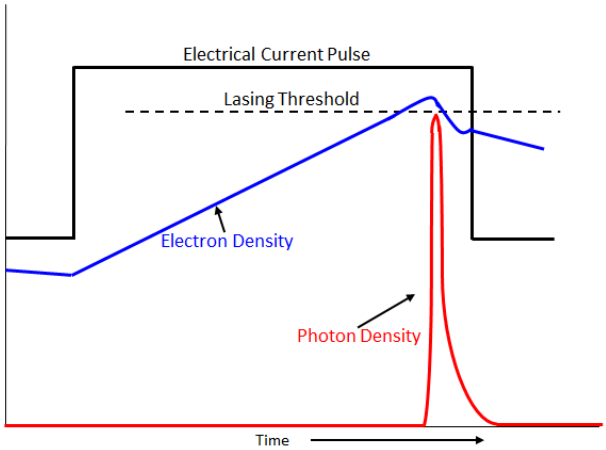

Figure 5.1: Typical Evolution of the photon and electron density during a gain switch cycle [152].

consequently a single optical pulse or spike. However, if carrier injection has not been stopped in time, then the carrier density can rebuild once more and the process repeats, generating multiple pulses. Therefore, stable picosecond pulses can be generated through this method when bias level, modulation frequency, electrical pulse width and its amplitude are optimised.

In order to obtain a good spectral quality output i.e. lasing on a single longitudinal cavity mode, some form of seeding is required and injection seeding via an external narrow linewidth laser source or self-seeding are the two most popular choices. A detailed investigation of injection-seeded and self-seeded gain-switched Fabry-Pérot laser diode at 1060 nm in [153] and [154] concluded that self-seeded gain-switched diodes provide similar performance compared to the injection seeding with an external narrow-linewidth laser source. Self-seeding is simple and less expensive than injection-seeding. Self-seeded gain-switched source operates by reflecting a portion of each pulse back into the diode laser using a grating. This requires that the repetition rate be set to any harmonic of the frequency defined by the round trip time of the seed pulses in order to synchronise the gain and seed pulses. While not used here, for completeness I note that mode-locked gain-switched pulses can be generated through self-seeding resulting in transform-limited optical pulses ([153] and [155]).

5.3 Gain Switched Laser System and Results

In this section, experimental setup and measurement results of a gain-switched diode laser-seeded MOPA system generating radially polarised pulses of 110 ps duration at a repetition rate of 1.367 MHz will be provided. This system has attained a maximum average output power of 42 W and a pulse energy of 30.7 μJ corresponding to a pulse peak power of 280 kW.

5.3.1 Experimental Setup

The picosecond seed used for the experiment consists of a PM-fibre pigtailed gain-switched diode laser as shown in Figure 5.2. The 1030 nm Fabry-Pérot laser diode (Oclaro LC96A1030-20R) was DC-biased below the lasing threshold via a Bias-Tee and

gain-switched by a train of sinusoidal RF pulses operating at a repetition rate of 87.5MHz. The laser diode (LD) was mounted on a printed circuit board (PCB) and was matched to the transmission line via a ∼50 Ω resistor and thermally stabilised at 25°C with a thermoelectric cooler (TEC). A 3 GHz pulse generator (Agilent 8133A) was used to generate the electrical sine-wave. The RF signal was fed into a 34 dBm RF power amplifier and superimposed on a DC bias current of 20 mA. This self-seeded configuration used feedback from a uniform fibre Bragg grating (FBG) with a reflectivity of 12.5% at centre wavelength of 1034.5 nm. In order to have a simultaneous monitoring of both temporal and spectral profiles of the output pulse at the end of the grating, a PM 3-dB tap coupler was spliced after a PM isolator connected to the FBG. The temporal profile of the pulses was measured with a 32 GHz bandwidth photo-detector (Agilent HP 83440D) and a 50 GHz bandwidth digital communication analyser (DCA) (Agilent 83480A). The spectral characteristics were measured with an optical spectrum analyser (YOKOGAWA AQ6370D).

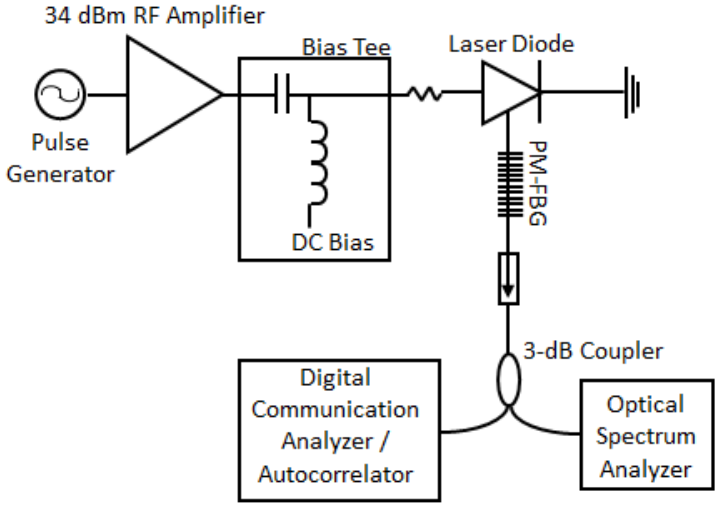

Figure 5.2: Experimental configuration for direct gain switching picosecond pulse generation through direct gain switching.

Optical pulses with 150 ps pulse duration and energy of ∼4 pJ (average power of 350 μW) at 1034.5 nm wavelength were produced. A 3-dB spectral bandwidth of 0.03 nm was measured.

A schematic of the picosecond MOPA system is depicted in Figure 5.3. The same amplifier stages that have been used in the nanosecond MOPA system (chapter 4) were used here. However, the first pre-amplifier stage box, after the gain-switched seed diode, replaced with a pre-amplifier with 0.85 m active fibre length, same as the second pre-amplifier stage. In this pre-amplifier stage, the seed pulses were amplified to an average power of ∼20 mW, which equates to a signal gain of ∼18 dB. A fibre pigtailed EOM (Photline NIR-MX-LN-10) was inserted, subsequently and before the second pre-amplifier stage. It was used as a pulse picker to reduce the repetition frequency from 87.5 MHz to 1.367 MHz in order to generate high energy/peak power pulses for materials processing trials. However, insertion of the EOM in the setup resulted in a total loss of 20.8 dB including ∼2.7 dB insertion loss of the EOM itself and an additional factor of 64 due to the reduction of the repetition frequency.

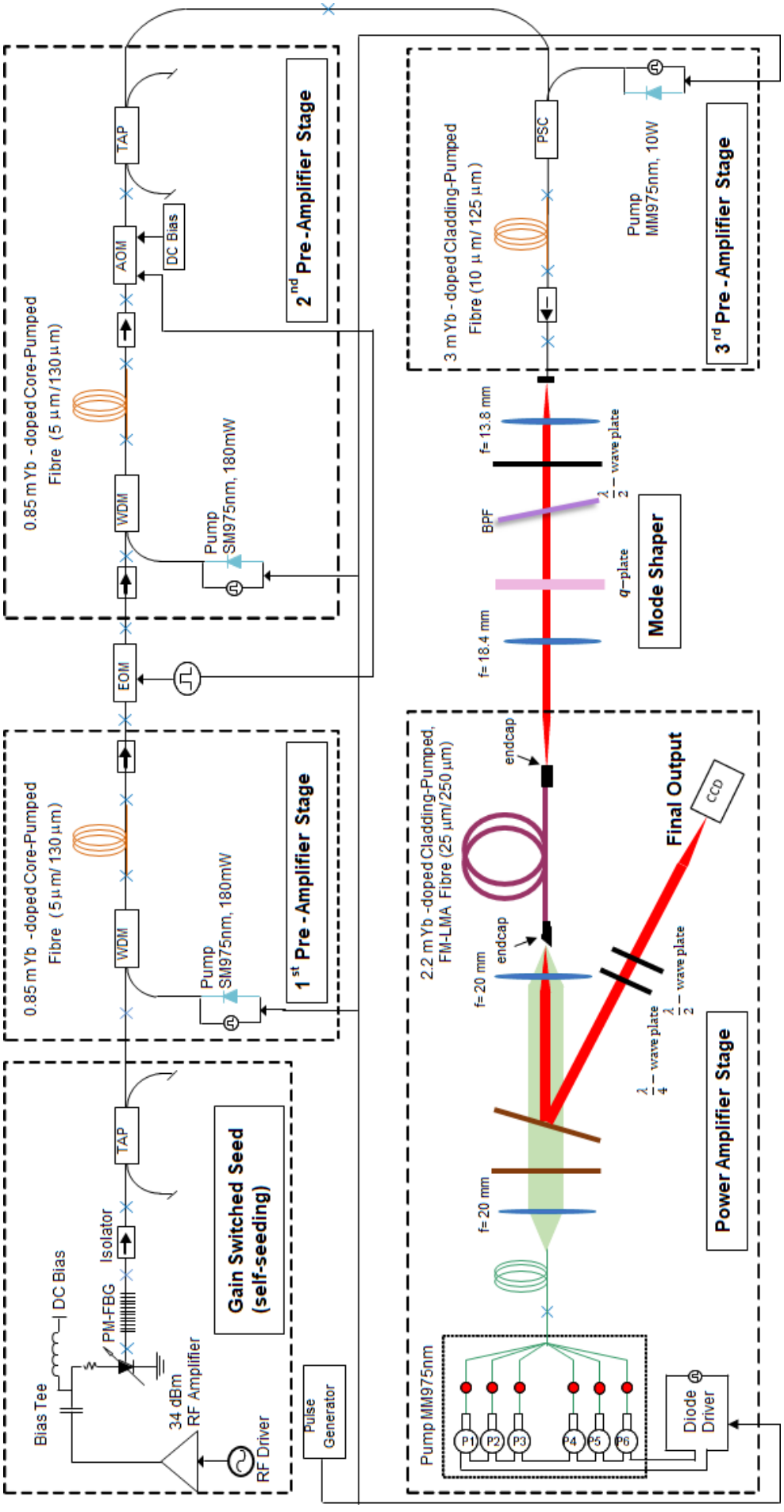

Figure 5.3: Schematic of picosecond laser system.

The second pre-amplifier was used to ensure adequate seeding to the next cladding-pumped amplifier stage. As in the nanosecond setup, a fibre pigtailed acoustic-optic modulator (AOM) was used after second pre-amplifier stage, to remove inter-pulse ASE. The AOM was synchronised to the EOM and an average power of ~5mW was obtained for seeding the third pre-amplifier stage.

The third pre-amplifier output had a linearly polarised Gaussian-shaped spatial beam with a polarisation extinction ratio (PER) of >20 dB and an output power of ~200 mW.

In order to convert the linearly polarised Gaussian-shaped beam into a radially polarised doughnut-shaped beam, a commercially available spatially varying half-wave plate made of liquid crystal polymer (*q*-plate, Thorlabs WPV10L-1064) was placed before the final amplifier. The shaped beam was then coupled into the final amplifier to excite the TM_{01} mode. The *q*-plate has a high transmission efficiency of ~>98%, and enabled a low coupling loss of ~1 dB. Therefore, the system enables sufficient power to be coupled into the final amplifier stage as compared to the use of a S-waveplate with higher total loss of ~3 dB. ~160 mW of radially polarised beam was coupled into the final amplifier. Figure 5.4 shows the output optical spectra of different pre-amplifier stages measured with an OSA with a low resolution of 2 nm.

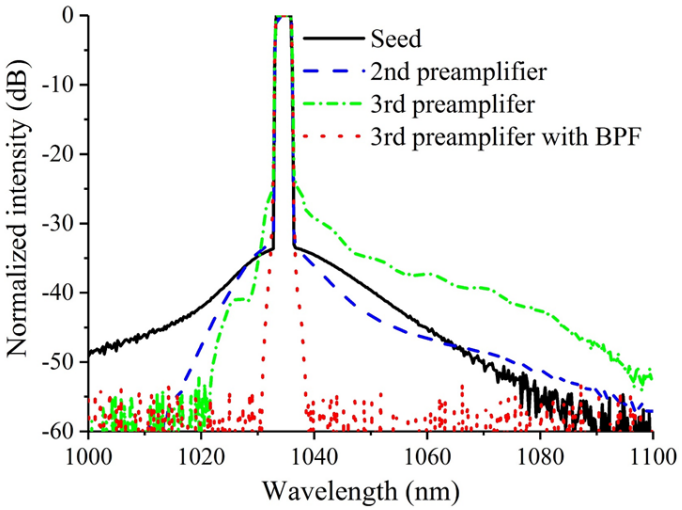

Figure 5.4: Spectra (resolution=2 nm) measured after the seed, the core-pumped preamplifier, and cladding-pumped preamplifier stages.

5.3.2 General Performance of the Gain Switched Setup: Power Scaling in Radially Polarized Output Beam

A maximum output power of ~42 W was measured for radially polarised TM_{01} mode (red circle) at a launched pump power of ~61 W, and ~29 W was obtained for the fundamental LP_{01} mode (blue square), both with a similar slope efficiency of ~76% with respect to the launched pump power (Figure 5.5). Therefore, a total energy gain of ~68 dB can be considered for the MOPA system. Also, pulse energy of 30.7 μJ was obtained for TM_{01} mode at a repetition frequency of 1.367 MHz, corresponding to ~280 kW peak power.

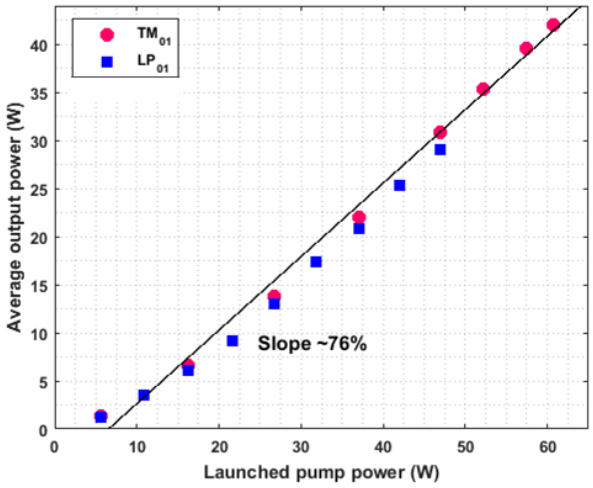

Figure 5.5: Average output power versus launched power measured at the power amplifier stage.

For the LP_{01} mode ∼29 W was obtained while the SRS peak at ∼1090 nm is ∼30 dB below the signal peak (Figure 5.6 (a), blue line), corresponding to a pulse energy of 21.2μJ and a peak power of ∼190 kW. It was observed that the doughnut-shaped TM_{01} mode has a higher SRS threshold and the average output power can be scaled up to 42 W for the same SRS peak suppression, as the comparison of the spectral characteristics of the pulse after the MOPA chain illustrates in Figure 5.6 (a) (red line).

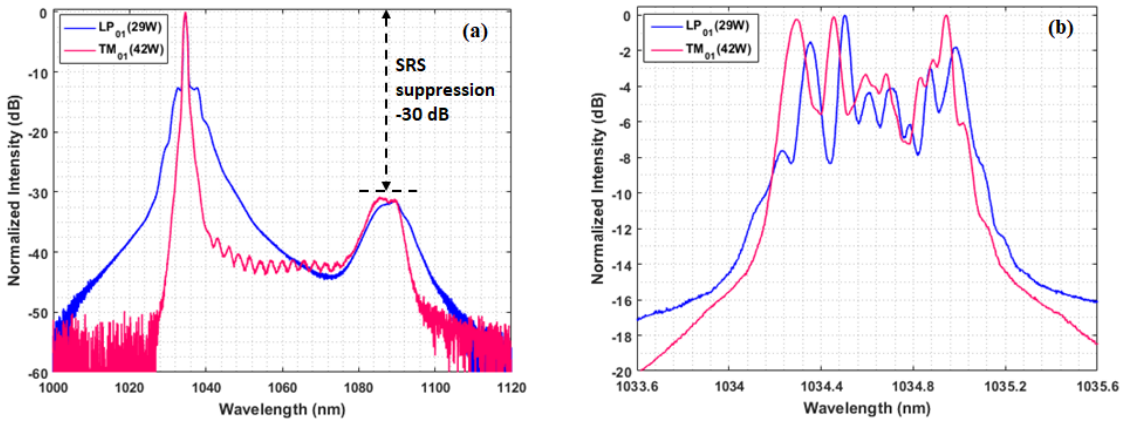

Figure 5.6: a) Spectra (resolution=0.5 nm) measured for the LP_{01} and TM_{01} modes at different output powers, b) Spectra (resolution= 0.02 nm) measured at the maximum output power of the LP_{01} mode (blue line) and TM_{01} mode (red line), 29 W and 42 W, respectively.

The short fibres used in the pre-amplifier stages suppressed nonlinear effects prior to the final amplifier stage. Hence, the majority of the observed broadening, due to SPM was in the power amplifier stage. The 3-dB spectral bandwidth of the output pulse broadened from 0.03 nm to 0.69 nm for the LP_{01} mode (blue line) and 0.73 nm for the TM_{01} mode (red line) in Figure 5.6 (b) as the power and energy were scaled up. The spectral profile acquired a maximum nonlinear phase shift of 6.5π (Equation 3.11).

The measured pulse width was compressed to a duration of ∼110 ps at the maximum output power of 42 W as shown in Figure 5.7 (oscillator pulse duration was ∼150 ps).

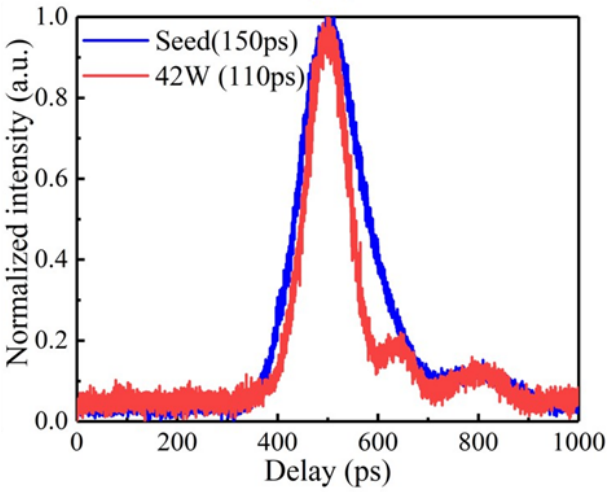

Figure 5.7: Temporal pulse profiles of the pulse generated from the oscillator (blue line) and at the maximum TM_{01} output (red line).

The typical doughnut-shaped intensity profile obtained at the maximum output power is shown in the Figure 5.8 (a) and (b) for the LP_{01} and TM_{01} modes, respectively. As with the nanosecond system the polarisation evolved with power changes but is ultimately correctable by a pair of half-wave and quarter-wave plates. The intensity distributions of the output beam after passing through a rotated linear polariser exhibited a symmetric two-lobe-structured intensity distribution parallel to the transmission axis of a polariser are shown in Figure 5.8 bottom row and were as expected from a radially polarised TM_{01} mode. White arrows indicate the transmission axis of the polariser.

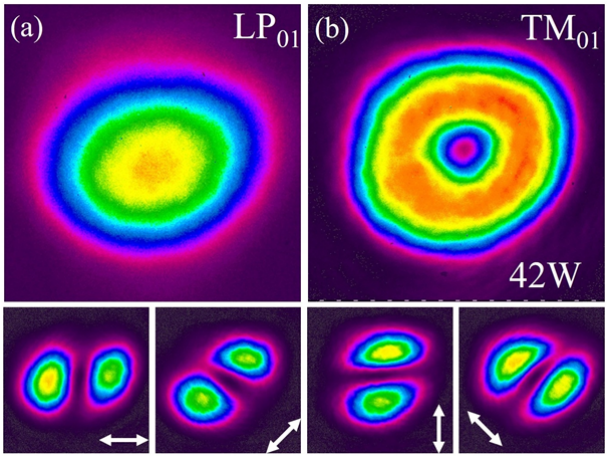

Figure 5.8: Typical beam profiles at maximum output power a) The LP_{01} mode at 29 W and, b) the TM_{01} mode at 42 W. The bottom row shows the beam intensity distributions of the TM_{01} mode passing through a rotated linear polariser.

5.4 Spatial Shaping Results at Average Output Power >100W

The presented MOPA system optimised to generate a high average output power beyond 100 W of radially polarised picosecond pulses. Eventually, an average output power of 106 W, at a repetition rate of 5.468 MHz, for the radially polarised beam was produced

by Dr. Di Lin [150] and then sent to University of Cambridge for material processing trials. To achieve this, the repetition rate of the MOPA system was increased four times to 5.468 MHz, to couple ∼500 mW doughnut-shaped radially polarised beam from the pre-amplifier chain into the final power amplifier stage, resulting in a linear increase of the average output power for the doughnut-shaped TM_{01} mode up to ∼106 W. Therefore, an amplifier efficiency of 77% with respect to the launched pump power was obtained at a gain of 23.3 dB corresponding to ∼176 kW peak power and pulse energy of ∼19.4 μJ for radially polarised output beam (Figure 5.9).

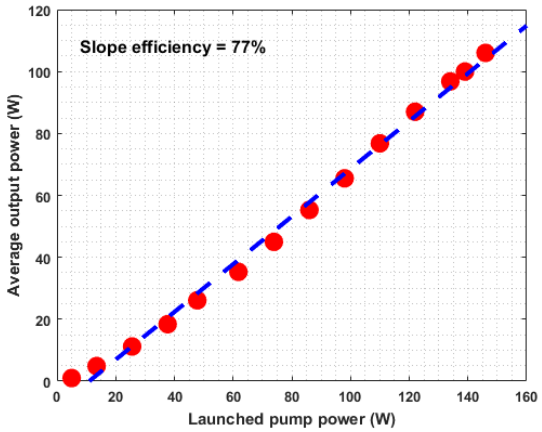

Figure 5.9: Average output power of the TM_{01} mode at a repetition rate of 5.468 MHz versus the launched pump power.

The evolution of the beam intensity distribution of the TM_{01} mode as a function of output power is shown in the Figure 5.10 (a)-(d). A doughnut-shaped beam profile was obtained, although the intensity at the beam centre gradually increased with an increase in output power and becomes quite appreciable at the maximum output power of 106W, as shown in Figure 5.10 (d). The one-dimensional intensity profile across the beam center for Figure 5.10 (d) is plotted in Figure 5.10 (e), indicates ∼93% of power appears to be in the TM_{01} mode at 106 W output power.

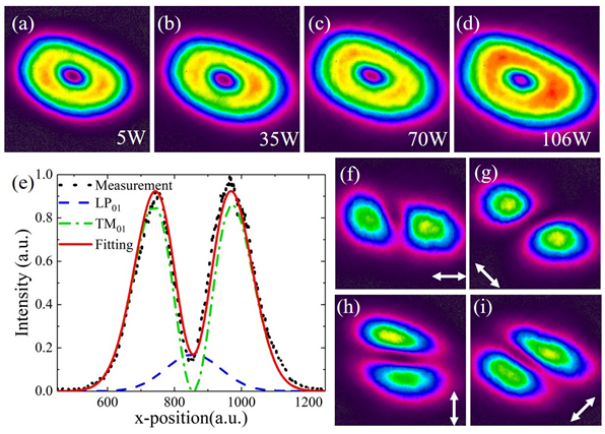

Figure 5.10: (a)-(d) Measured intensity profiles of the radially polarised beam at different output powers, (e) one-dimensional intensity profile across the beam center at 106 W fitted with an incoherent superposition of the LP_{01} and TM_{01} modes, (f)-(g) the beam intensity distributions after passing through a rotated linear polariser [150].

5.5 Conclusion

In this chapter, generation of radially polarised picosecond pulses with high energy of 30.7 μJ, high peak power of 280 kW, and an average output power of 42 W at repetition rate of 1.367 MHz were presented. The average output power of the radially polarised beam was scaled up to 106 W at a repetition rate of 5.468 MHz, corresponding to a pulse energy of $\sim$19.4 μJ and a peak power of $\sim$176 kW. Such a fibre laser source with unique polarisation properties is expected to be attractive and enabling for a variety of laser materials processing. The laser delivered to the University of Cambridge for further materials processing trails in both linearly polarised Gaussian and radially polarised modes.

Chapter 6

Full Temporal Shaping of Picosecond Pulses Using a Mode-Locked Femtosecond Seeded MOPA

The first picosecond temporal pulse shaping attempt in a fully-fiberised MOPA lasr through the requirements of the ERM project is described in this chapter. Development of a mode-locked seeded MOPA including seed, fiberised pulse stretcher, and power scaling configuration is explained. The generation of complex pulse shapes was achieved through the principle of frequency-to-time mapping (FTM), described in chapter 3, with the use of WaveShaper. Investigations on the challenges for power scaling in temporally shaped ultrafast pulses are presented in association with experimental results.

6.1 Introduction

There is a great interest for picosecond pulse profiles in the industry applications, especially materials processing. None of the commercially available laser systems in the range of picosecond presented the capability of creating complex pulse shapes with durations in the 10-100 ps regime. However, a number of researches have been carried out for picosecond pulse shaping with desired temporal features [45–48]. Recently, a robust, flexible and applicable method was developed in the ORC [50], explaining a closed-loop control algorithm to achieve a laser system for high precision materials processing and other industrial applications. In that work the FTM technique (subsection 3.4.2.1) was applied to a CPA laser system, comprising a cumbersome stretcher with large stretch ratio and compressor configuration [156]. Therefore, my project was focused on the implementation of an optimised fully-fiberised Yb-doped MOPA with all fibre stretcher, that could provide a compact, integrable, and practical picosecond laser for materials processing, particularly for our project partner.

Negative impact of nonlinearities on the output pulse forms is observed as a result of the high peak power in a fiberised MOPA, which mainly manifest after the power amplifier stage. Hence, some improvements have been identified to obtain more refined set of experiments. Furthermore, there was no possiblity to compress the pulse, unlike the CPA based laser.

As it was discussed in chapter 3, a laser source with broad spectral width is required to provide enough bandwidth for the temporal pulse shaping using the WaveShaper. Hence a femtosecond mode-locked laser source was selected and used with a fiberised stretcher to provide appropriate dispersion for demonstrating combined spatio-temporal shaping. The prototype of the MOPA in this chapter is based on an in-house built seed, while in the next chapter the final system was enhanced by frequency multiplier and seeding with a smoother spectrum, as this was found to be critical owing to the high B-integral value of the setup (section 6.3.2.1). Mode-locked laser oscillator configuration details, operating principle and its performance are explained in the following section.

6.2 Mode-Locked Laser Oscillator Development and Characterisation

In accordance with the wide range of works to develop the mode-locked lasers, passively mode-locked pulse fibre lasers present a compact, flexible, stable and a low cost version of pulsed laser sources [157–164]. These sources have an extensive category of applications, including optical communications [45,47,48,165], microscopy [166,167] and imaging [168], ultrafast science [169], materials processing [27, 50, 132, 170] and more [171]. Among all, a self-starting positively chirped pulse fibre oscillator configuration is constructed with a semiconductor saturable absorber mirror (SESAM 6.2.1.1) as the passive mode-locking element coupled with a broadband chirped fibre Bragg grating (CFBG 6.2.1.2) [172–176] depicted that not only is capable to provide the desired spectral bandwidth, also stand on SESAM parameters, can produce short picosecond pulses using less fibre length for the dispersive stretcher. In that regard, a linear cavity configuration [172–175,177] is possible as a simpler in design, rather than a ring cavity layout [176, 178]. In light of the above approaches, an optimised linear cavity was constructed with polarisation maintaining single mode fibre granting an environmentally-stable mode-locked fibre laser. The laser generated positively chirped pulses with a pulse duration of 7.5 ps at a repetition rate of ∼23 MHz on 10 nm 3-dB optical spectra bandwidth, well enough for our aim of temporal pulse shaping in a MOPA system. All the details of the oscillator configuration, characteristics of the applied components and its performance are presented in the next subsections after a brief explanation of mode locking principle.

6.2.1 Mode-Locked Fibre Laser Operating Principles

Mode-locking is a technique by which a laser forms ultrashort pulses and can be described in terms of either the frequency domain or the time domain. The term mode locking itself emanates from the frequency-domain description [179]. By careful design of the laser cavity, a pulse can experience saturable gain/loss, spectral filtering, dispersive spreading and a range of nonlinear phenomena related to the Kerr effect and stimulated scattering within each cavity round trip [164]. Practically, periodic modulation of the amplitude or phase of light at the fundamental cavity free-spectral range initiates mode-locking that can be implemented either actively using an optical modulator, or passively using a saturable absorber device with a nonlinear absorption profile [180–182].

Having more gain than losses in the laser cavity results in the so called longitudinal modes when their gain increase after each round trip through the cavity, replenishes the

pulse energy (Figure 6.1 (a)). They are also imposed by the optical cavity, spaced out by $\Delta\nu = c/2nL$, resulting in a steady-state output of the laser, where c is the speed of light, L is the length of the laser resonator and n is the effective group-velocity index. Mode locking implies a fixed phase shift exists between the various modes and the cavity emits a train of periodic temporal output pulses that are phase locked [179, 183].

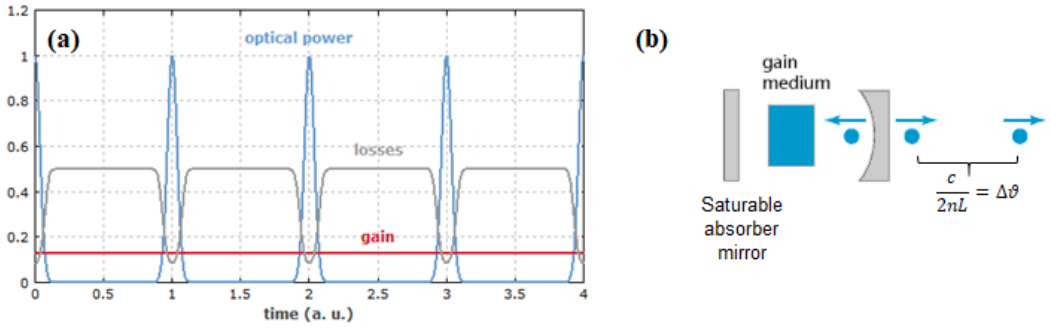

Figure 6.1: a) Temporal evolution of optical power and losses in a passively mode-locked laser, b) Schematic setup of a passive mode-locked laser `https://www.rp-photonics.com/passive_mode_locking.html`.

The large gain bandwidth of rare-earth-doped fibres (typically tens of nanometers) allows the generation of femtosecond pulses. In that regard, ultrafast fibre lasers, which are actively or passively mode-locked for generating ultrashort pulses, are known as mode-locked fibre lasers [183, 184]. Passive mode-locking techniques do not require an external signal to the laser unlike the active type to produce pulses. A commonly used device to achieve the nonlinear saturable absorption is through the combination of a mirror and a saturable absorber, forming a SESAM, resulting in a simpler laser setup (Figure 6.1 (b)). This mechanism generates shorter pulses than with active mode locking due to the faster loss modulation provided by the SESAM. The pulse duration is determined by a balance of various effects, including the pulse shaping action of the saturable absorber as well as pulse broadening by the limited gain bandwidth. In a passive dissipative mode-locked fibre laser a SESAM plays the role of the passive element. Additionally, CFBG insertion introduces the dispersion balancing required for stretch pulse mode locking temporal pulse shaping.

6.2.1.1 Characteristics of the SESAM

A semiconductor saturable absorber mirror (SESAM or SAM) is a mirror structure with an incorporated saturable absorber in front of it, all made with semiconductor fabrication technology. It typically contains a semiconductor Bragg mirror structure and a single quantum well absorber layer (InGaAs type for 1 μm wavelength). Such devices have the potential to generate ultrashort pulses in passively mode-locked scheme of various types of lasers. They usually allow to obtain a reliable self-starting mode locking in case of correct selection of the operating parameters of the SESAM, as reported in a wide range of literature such as [8, 157–159, 161, 162, 172–174, 176–178, 183, 185–187].

Most important characteristics of a SESAM particularly used for passive mode locking are the operation wavelength, bandwidth, modulation depth, saturation fluence, and the recovery time, which by varying the material composition and addressing certain design parameters can be tailored. An inappropriate design leads to instabilities

or SESAM damage. Therefore, for the mode-locked fibre oscillator we relied on the previous customised designed SESAMs by BATOP for such systems. Two SESAMs were trialled, 749-I and 796 wafer. Their spectral reflectance curves are illustrated in Figure 6.2 (a) and (b), respectively. Both of them have 1 ps relaxation time constant with a chip area of 4 mm × 4 mm and a thickness of 450 μm. Both of them were ordered as the unmounted version. The wafer number 749-I (Figure 6.2 (a)) has a high damage threshold of ϕ=3 mJ/cm^2, and a modulation depth of 11% and a very high reflectivity (>70%) at 1040 nm wavelength, while wafer 796 type (Figure 6.2 (b)) has reflectivity of 50%, at 1030 nm wavelength, and a modulation depth of 30% with much lower damage threshold in the range of 800 μJ/cm^2.

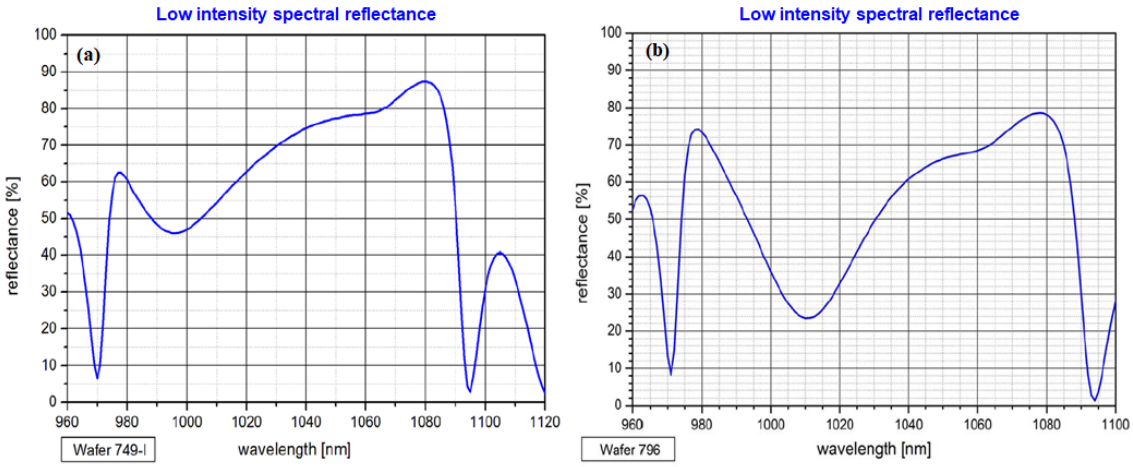

Figure 6.2: Spectral reflectance characteristics of SESAMs a) wafer 749-I and b) wafer 796.

The SESAMs were mounted first on the fibre mount FM-1.3 from same provider for fibre coupling experiments using SAM chips with a size of 1.3 mm × 1.3 mm, enabling a fully-fiberised linear cavity (Figure 6.3 (a)). To have the high efficiency of coupling to the fibre, a PM980 fibre with FC/UPC connector used. In this case the SAM chip can be easily removed to be replaced by any other one. Also, the end-facet of the fibre can be cleaned after any slight change of the SAM chip position owing to any unwanted local damage of the SAM surface. But despite all of these advantages, it suffers from stability problems in comparison to gluing the SAM onto a fibre end. Thus, a home-made SESAM holder like Figure 6.3 (b) was applied, which perfectly held the chip with an adequate fibre end-facet touch to the chip.

6.2.1.2 Characteristics of the CFBG

Chirped Fibre Bragg Gratings (CFBGs) are characterised by a non-uniform modulation of the refractive index within the core of an optical fibre in contrast to the spatially uniform periodicity of the unchirped FBGs [188–194]. A CFBG behaves as a cascade of FBGs, where the Bragg wavelength varies along the grating, since each one reflects a narrow spectrum [193]. Linearly chirped FBG configurations can also have a reflection spectrum broader than uniform FBGs, ranging between few nanometers to tens of nanometers [194].

CFBGs enable dispersion compensation by introduction of a wavelength dependent differential group delay, which led to their popularity for optical communications [188–

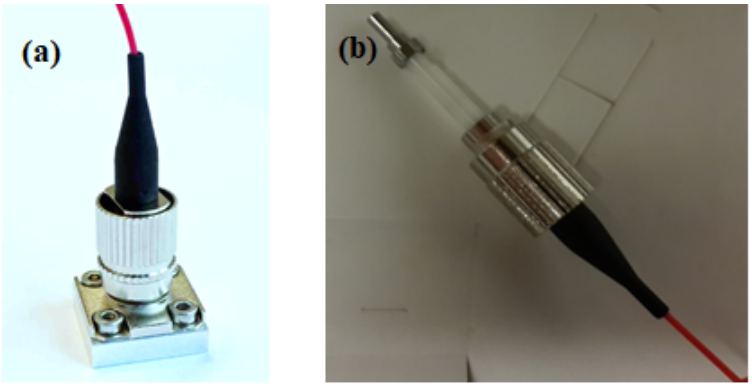

Figure 6.3: a) BATOP FM-1.3 fibre mount, b) home-made SESAM - fibre holder.

191]. As a result, their application gained interest in recent designs of linear cavity mode-locking oscillators, specifically PM CFBGs in 1 μm wavelength region [172, 174, 175]. Through the advice of NKT Photonics staff we selected a PM-CFBG with broad 3-dB spectral bandwidth of 15 nm fabricated by TeraXion for 1035 nm central wavelength. The designed CFBG has 16% reflectivity and a dispersion of 0.22 ps/nm (Figure 6.4). So it dominates the net cavity GVD and by not allowing full compression of the pulse in the cavity, minimises nonlinearity by having a very close absolute dispersion value to the estimated cavity dispersion via the required length of fibres. It is worth mentioning that this CFBG was the only available one at the time, which provides the desired parameters for our mode-locked oscillator.

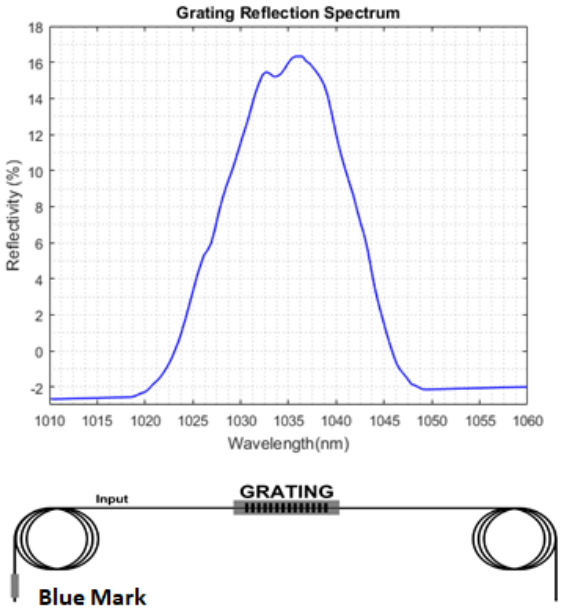

Figure 6.4: Reflection spectrum (top) and the schematic (bottom) of CFBG.

6.2.2 Oscillator Configuration and Laser Performance

Figure 6.5 illustrates the configuration of the home-made mode-locked oscillator. The linear cavity consists of one SAM, a length of passive fibre, here PM980 fibre, an in-

line polariser with a blocked fast-axis in the same direction as the isolator after the oscillator, gain fibre segment (PM-Yb 5/130 μm) and finally the chirped fibre Bragg grating (CFBG).

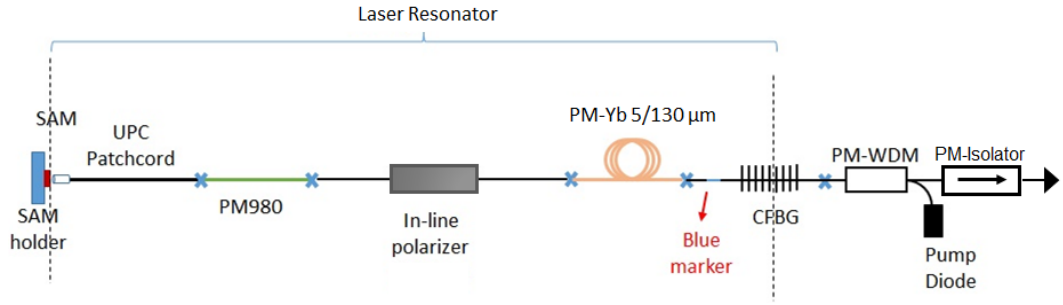

Figure 6.5: Experimental configuration of the mode-locked laser oscillator.

To avoid residual modulation in the spectrum, the PM-WDM is used outside the cavity and pumped the doped fibre through the CFBG leading to the reduction of the intra-cavity splice issues [175]. Rather than insertion of a coupler to control the pulse dynamics and polarisation in the cavity, a PM pigtailed 1064 ±30 nm in-line polariser (Thorlabs ILP1064PM-APC) was inserted, which has ∼10 dB PER at ∼1040 nm wavelength. A length of 80 cm of polarisation maintaining Yb-doped fibre (PM-YDF) that has a 5 μm core diameter with a numerical aperture (NA) of 0.12 and a 130 μm cladding diameter with an NA of 0.46, is used as the gain segment of the cavity. It is spliced to the shorter wavelength side of CFBG to complete the linear cavity configuration. The gain fibre is pumped by a 975 nm single mode pump laser diode. The total cavity length reached to ∼4.5 m, after a 1 meter length of passive PM980 fibre was used, corresponding to ∼23.2 MHz repetition rate. A maximum average output power of 55 mW was measured after the cavity (at the WDM pigtail), before the onset of multiple pulse generation occurrence rather than single pulse operation (Figure 6.6).

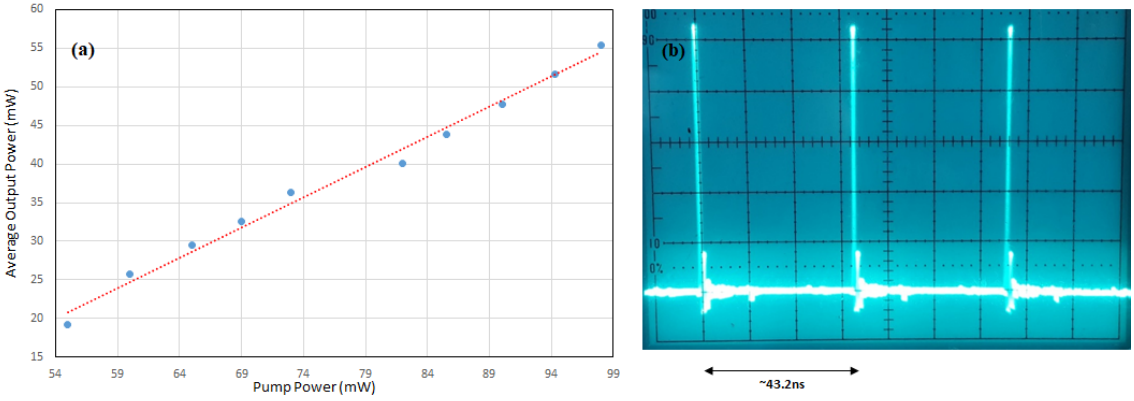

Figure 6.6: Mode-locked laser source performance a) average output power versus pump power, b) the output signal trace on scope.

It is worth mentioning that the wafer number 749-I SESAM (Figure 6.2 (a)) was first used in the cavity due to its higher reflectivity at 1040 nm wavelength. However, after insertion in the oscillator, this high reflectivity caused instabilities in the oscillator

performance, resulted in a non reliable mode-locking laser, ultimately. Consequently, it was replaced by the 796 wafer type with 50% reflectivity at 1030 nm wavelength (Figure 6.2 (b).

The spectrum is presented in Figure 6.7. By increasing the pump power, the optical spectrum maintains the spectral profile while the spectral bandwidth increases. However, the chirped pulse spectrum depicts the so called "cat ear" or "Batman" shape. So, it seems the peak power is too high in this cavity and the pulse is experiencing non-linear chirp, which cannot be compressed by a diffraction grating pair. Finally, a pulse energy of 1.56 nJ and a peak power of 207 W measured for ∼37 mW average output power, and 7.5 ps from this mode-locked laser (Figure 6.8 (a)). Avoiding strong residual modulation on the spectrum, the active fibre was not pumped for more than ∼73 mW.

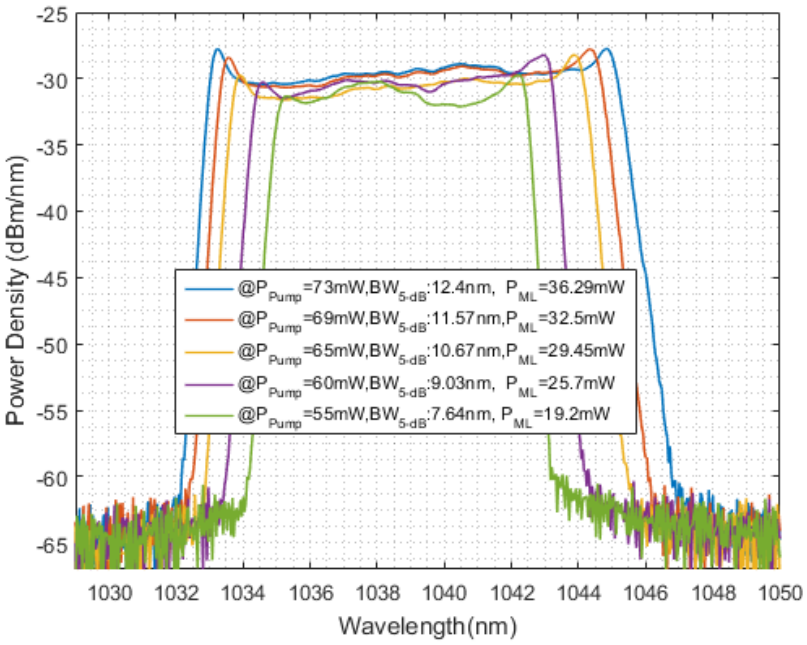

Figure 6.7: Mode-locked laser source spectral characteristics at different pump powers.

A non-collinear SHG autocorrelator instrument (FemtoChrome, model FR-103) was used to measure the pulse width after the oscillator. In standard configuration of this autocorrelator type, rotation frequency is set on 10 Hz. Hence, the coefficient of 32psec/msec should be use to scale the FWHM value measured. Additionally, according to the pulse shape assumption/fitting function, a conversion factor should be considered, which for Gaussian curve fitting is calculated to be 0.707. Results of the autocorrelation trace is presented in Figure 6.8 (a). In order to verify the oscillator is operating by single peak pulse at the ∼23.2 MHz repetition rate, the radio-frequency (RF) spectrum was measured by an electrical spectrum analyser (Agilent E4446A) as is illustrated in Figure 6.8 (b).

Note that to avoid environmental instabilities being a problem, the cavity was fully built with PM fibres, with the light polarisation only along the slow axis [175,195] similar to PM isolator applied after the seed. Moreover, the total fibre length of the cavity was

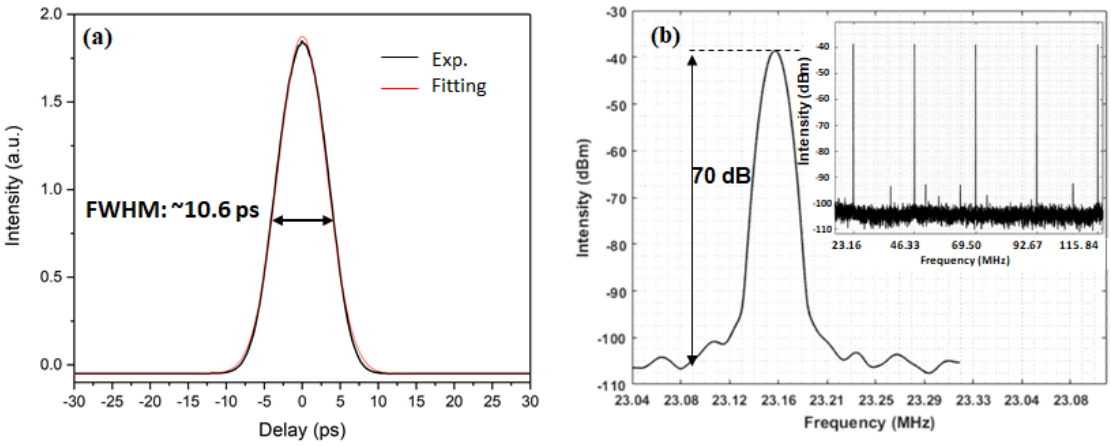

Figure 6.8: a) Autocorrelation trace of the oscillator with the Gaussian fitting, b) RF spectrum at the fundamental frequency of ~23.2 MHz. Inset: RF spectrum with ~100 MHz span.

chosen after measuring the pulse width after compressor through negative dispersion introduced by a diffraction grating pair (Figure 6.9) [196]. The time bandwidth product (TBP) was calculated to be 1.1, which is 2.5 times the transform-limited value for a Gaussian pulse (0.44), but close to that of a transform-limited pulse with a rectangular-spectrum (0.88). It seems the high peak power provides nonlinearity after the cavity through the transmission pigtail of the CFBG and WDM. As a result, even adding more fibre length after that, the output signal suffer more nonlinearities through SPM, preventing the pulse being compressed to the transform-limited width.

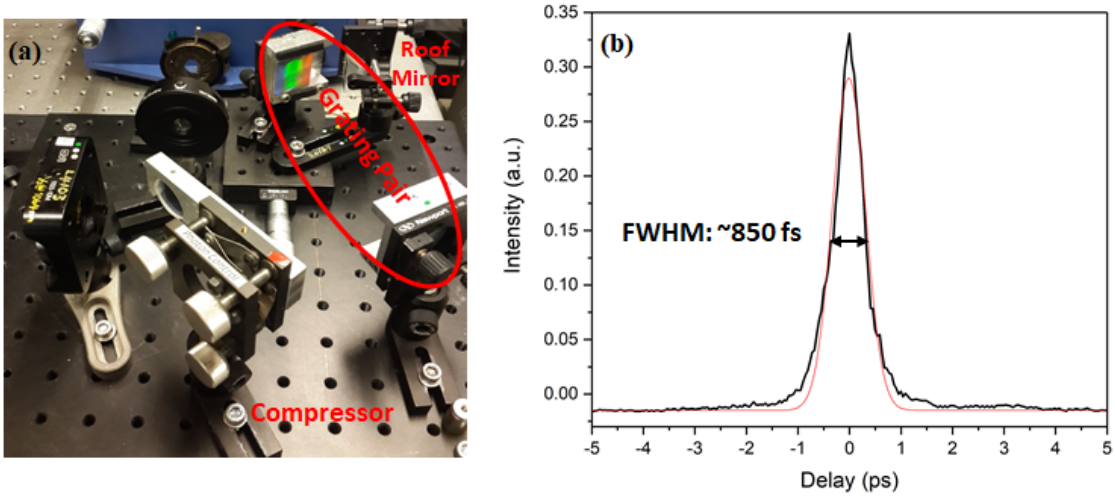

Figure 6.9: a) Compressor setup image including a diffraction grating pair and a roof mirror, b) Autocorrelation trace of the compressed pulse with the Gaussian fitting.

Eventually this entirely stable self-starting mode-locked oscillator resembled appropriate parameters via the delivering pulse width and the spectral bandwidth to carry out the temporal pulse shaping in a MOPA laser system at high average power.

6.3 Femtosecond Seeded MOPA Laser System Configuration and Results

The MOPA setup includes three amplifier stages (core-pumped, cladding-pumped and the power amplifier stage), a fiberised stretcher and the WaveShaper.

6.3.1 Experimental Setup

The experimental setup including diagnostics is presented in the Figure 6.10. All the inserted segments are described in the following subsections.

6.3.1.1 Stretcher

A PM isolator after the oscillator protects it from any reflections and 110 m length of Nufern PM980 fibre (PM980-XP) stretcher followed, creating ∼65 ps pulses with 12.5nm bandwidth. We observed that a highly modulated spectrum was measured after the stretcher, which we believe was due to the high nonlinear phase shift of $> 2\pi$ owing to the high peak power at the input of the stretcher. An input power level of less than 1% of the seed output power would lead to nonlinearity free spectrum. However, the microwatt power level requires more amplifier stages before the power amplification step. Consequently, the first 99/1% inserted coupler before stretcher (for monitoring feasibility or employing in cross-correlator) should be replaced by a coupler providing a coupling ratio in the range 15-20% at the input of the stretcher. Hence, 20% of the source power was coupled into the stretcher via a 20/80% PM coupler while the mode-locked oscillator output power decreased to ∼25 mW with a 5-dB spectral bandwidth close to 9 nm by reducing the pump power. To this extent an average power level of ∼3.7 mW was available after the stretcher, which would be much lower at the input of the cladding-pumped amplifier stage after passing the WaveShaper, isolator and monitor tap by a total insertion loss of ∼9 dB. Hence, adding a core-pumped pre-amplifier stage before the WaveShaper is necessary.

6.3.1.2 First Pre-amplifier Stage

This first pre-amplifier stage consists of an 80 cm long length of polarisation maintaining Yb-doped fibre (PM-YDF) that has a 5 μm core diameter with a numerical aperture (NA) of 0.12 and a 130 μm cladding diameter with an NA of 0.46. A 975 nm single mode pump diode was coupled into the fibre through a PM-WDM in a forward core-pumped format. An average amplified output power of ∼53 mW measured with the gain of ∼10-11dB.

6.3.1.3 WaveShaper

The output PM980 fibre of the core-pumped pre-amplifier was connected into the WaveShaper with a PM980 patch cord. The output power after the WaveShaper was ∼14 mW. The pulse width increased to ∼55 ps (over ∼10 nm spectral bandwidth), following an extra length of fibre inserted after the stretcher.

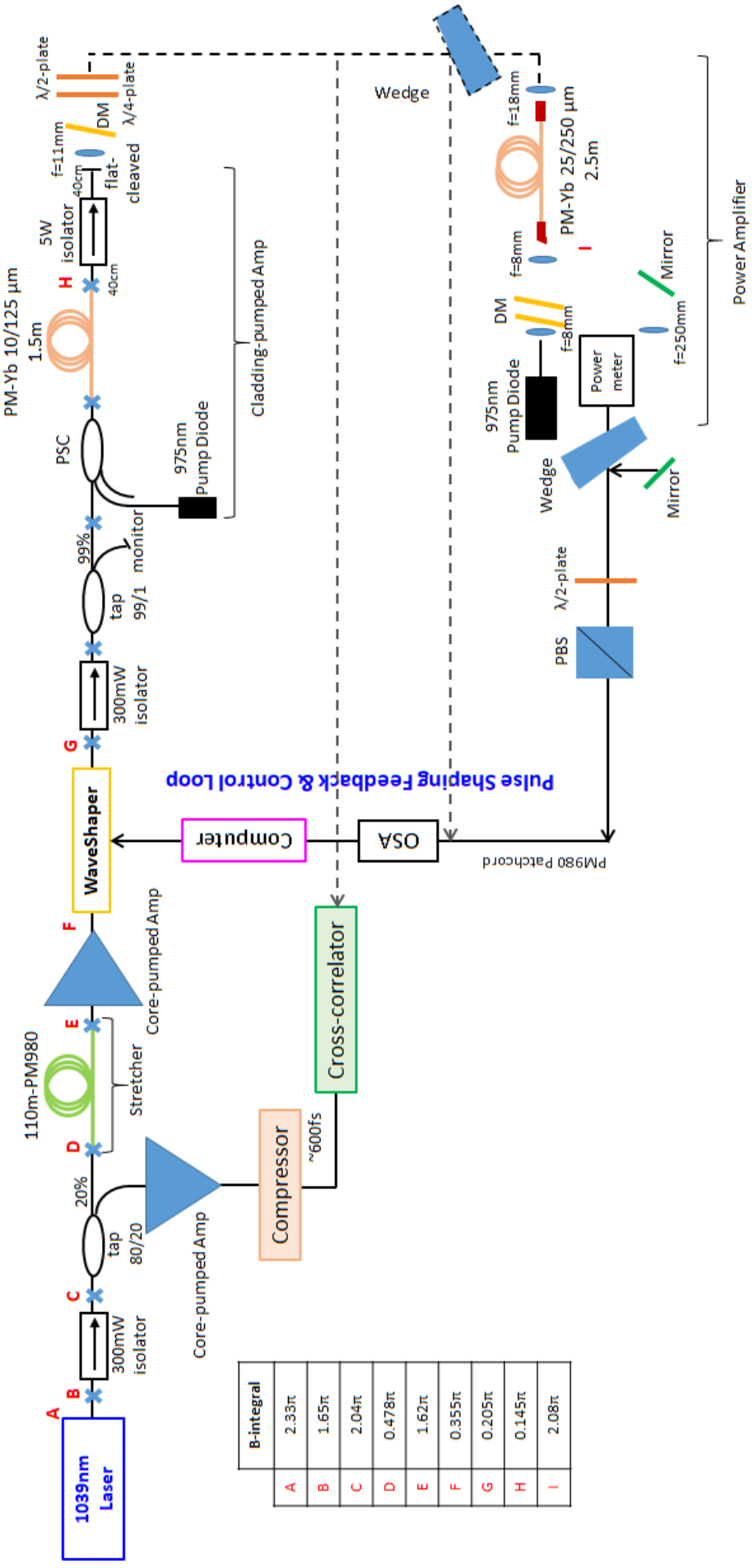

	B-integral
A	2.33π
B	1.65π
C	2.04π
D	0.478π
E	1.62π
F	0.355π
G	0.205π
H	0.145π
I	2.08π

Figure 6.10: Full picosecond experimental setup including temporal diagnostics.

Gain-induced reshaping and inhomogeneity in the WaveShaper meant open-loop control of the pulse shape was not appropriate and we implemented the same closed-loop iterative feedback algorithm using the measured output spectrum and compensate any distortions before yielding the final desired temporal shape as was published in reference [50]. Some improvements were made to increase the range of temporal shapes and to use just one iteration of the code. So it was faster for industrial applications.

The resolution difference between OSA and WaveShape precludes the direct sending of the desired spectral shape through the WaveShaper. Therefore, it needs to be corrected in the closed-loop iterative feedback algorithm for temporal pulse shaping. Hence, the steps in the algorithm are as following (refer to [50]): first, before beginning the feedback loop, the wavelength mismatch between the WaveShaper and the OSA was measured by setting the attenuation of the WaveShaper to zero for all wavelengths. This mismatch was then compensated in the rest of calculations of the iterative feedback loop. The subsequent iterative feedback loop consists of five main steps. (1) The spectrum at the output of each desired output of the laser system is measured using an OSA and loaded into the computer. (2) A desired light spectrum is calculated with the targeted shape and the same pulse energy as that in the measured spectrum. (3) The required modification or attenuation profile is calculated by taking the difference between measured and desired spectra. This is done at the 1-GHz spectral sampling grid of the WaveShaper, and the spectrum from the OSA is interpolated to that grid. The modification is added to any previous attenuation spectrum stored from earlier iterations. (4) The mean spectral fluctuation (i.e. unwanted spectral ripple) in the measured spectrum is evaluated and reduced from the attenuation for the whole spectrum. The value differs for each part of the laser system and depends on the amplification range obtained by power scaling (maximum 1 required for our system). We found that this improves the stability of the feedback loop for the nonlinear system and also makes it more resilient to ripples. Furthermore, any negative attenuation values (i.e. gain) were set to zero and all attenuation values larger than 25 dB were set to 25 dB, which ensured that all the attenuation values are within the specified setting range for the WaveShaper. (5) The calculated attenuation spectrum is sent to the WaveShaper by the program and as soon as the WaveShaper finishes changing the orientation of the liquid crystals in the SLM a new spectrum is measured and loaded into the computer according to Step (1) of the loop.

The algorithm was tried in a loop directly from the WaveShaper output port for square, double peak energy bridge (DPEB) and Gaussian pulse shapes as illustrated in Figure 6.11 (a) over 8.8 nm spectral bandwidth. The resulted shapes are provided in comparison with the original first trace after it passes through the WaveShaper (unshaped signal). In average the depth of ripples have been reduced to $\sim$0.5 dB from $\sim$1.5 dB, shaping more flattened spectral profile. That is well observable in the square pulse shape. Double peak pulse shape was defined to have 20 dB peak altitude, which well is resolved after running the shaping algorithm. However, in order to clarify the position of the peaks and direction of the working principle, the peak at shorter wavelength side of the spectrum was defined to be placed in $\sim$3 dB lower height that is properly assigned in the output shape. A Gaussian shape is also shown. Finally, the minimum possible spectral bandwidth for temporal pulse shaping was investigated using square pulses with different bandwidths as illustrated in Figure 6.11 (b). It depicted that no more square pulse shape can be obtained for the bandwidths below $\sim$2 nm.

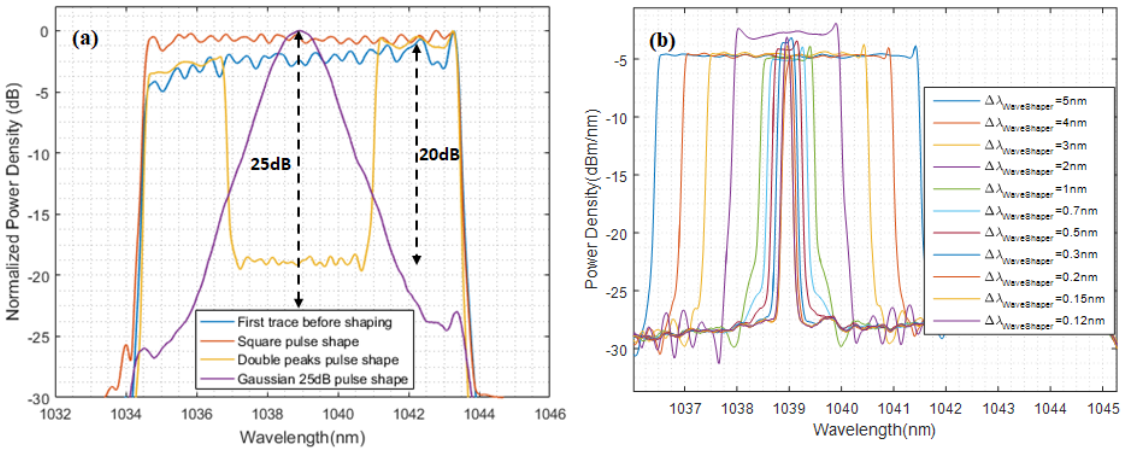

Figure 6.11: a) Square, double peak energy bridge (DPEB) and Gaussian pulse shaping after the WaveShaper, comparing the ripples modification with the first trace (blue spectral profile) b) Investigation of the WaveShaper performance regarding the minimum possible spectral bandwidth for temporal pulse shaping using square pulse shaping.

6.3.1.4 Second Pre-amplifier Stage

The second pre-amplifier consists of a 1.5 m long Yb-doped LMA double clad PM fibre with a core diameter of 10 μm (NA= 0.075) and a cladding diameter of 125 μm (NA=0.46). This amplifier stage was cladding pumped with a 975 nm multimode pigtailed laser diode in a forward direction. High index polymer is used at the output section of the Yb fibre to strip out the cladding modes and leak out the unabsorbed pump. A low index polymer is applied at the input splice point between a pump/signal combiner (PSC) and the Yb-doped fibre to transfer the pump light into the active fibre.

The performance of this stage in respect to different launched pump powers are presented in Figures 6.12 and 6.13 after insertion of a dichroic mirror (DM) to separate the signal from the unabsorbed pump power and a 4% wedge to reduce the power for spectral characteristic measurements (dashed-line and wedge in Figure 6.10). Average signal output power of up to ~1.7 W was measured for absorbed pump power of ~3 W, corresponding to 70 nJ pulse energy and a peak power of 1.8 kW while the amplifier is operating at 22.77 dB gain.

The Figure 6.13 shows the ripples increasing with power. Therefore, it was decided to investigate the laser operation at temporal pulse shaping attempts. However, the results in higher power were absolutely suffering of the nonlinear phase shift effect. Nonlinear phase shift values of ~1.7π and ~4π were calculated for ~400 mW and ~800 mW average signal power levels, respectively. Hence, the operating output power of this amplifier stage needed to be reduced to 400 mW rather than ~1.7 W, which not any more lead us to obtain the aim of 100 W at the end of the power amplifier stage by a 20 dB gain. To verify the capability of temporal pulse shaping some shaping experiments were carried out at a power level of 400 mW for ~1.2 W absorbed pump power. Operation at uniform gain distribution through the spectral profile are demonstrated in the next sections.

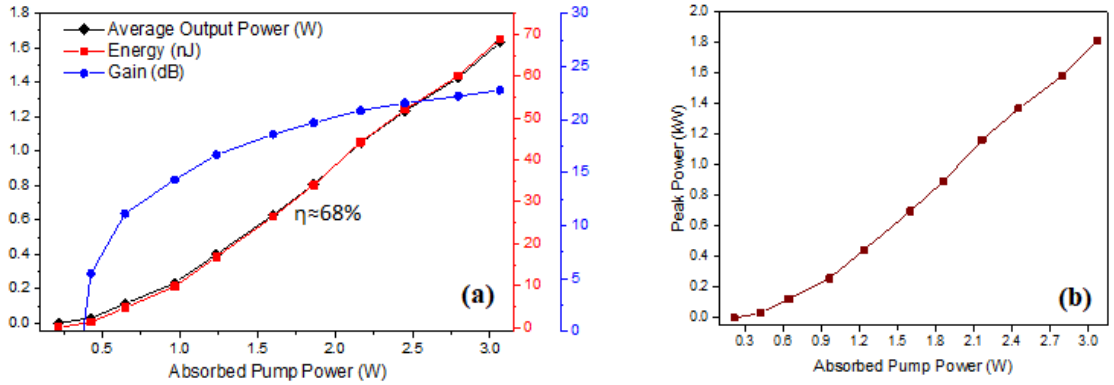

Figure 6.12: a) Average output power, energy and gain, b) Peak power of the second pre-amplifier stage versus the absorbed pump power.

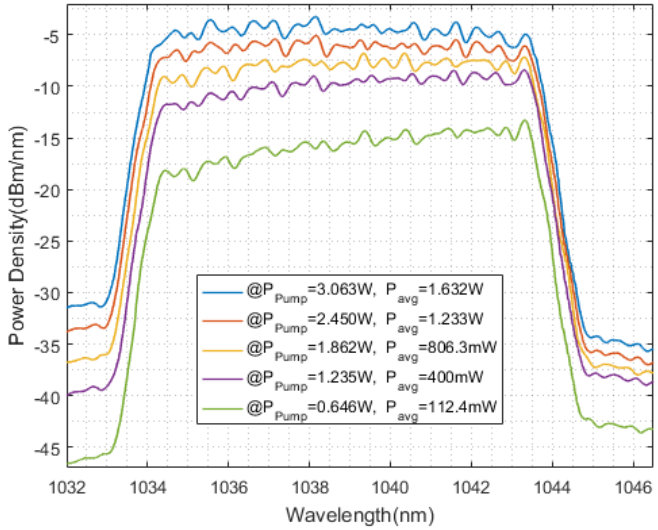

Figure 6.13: Spectral characteristics of the cladding-pumped amplifier stage at different absorbed pump powers.

6.3.1.5 Temporal Pulse Shaping Results After Second Pre-Amplifier

As described in chapter 3, I used a cross-correlator to characterise the pulses. The reference pulse duration of ∼600 fs was created through a pair of diffraction gratings similar to the configuration in Figure 6.9 (a) after the 80% port of the tap and a core-pumped amplifier stage. The setup is shown by the photograph in Figure 6.14. The path of the unknown signal is illustrated by dashed lines before a dashed wedge (placed on top of a folding mount to easily unblock the beam path toward power amplifier stage) in the experimental setup schematic in Figure 6.10.

First of all, a square shaped pulse was tested to calibrate our wavelength-to-time scaling precisely. A pulse width of ∼55 ps was measured for a bandwidth of 8.8 nm. The cross-correlation trace provides the pulse profile in time domain and it should well match the calculated shape from the spectral profile by incorporating the chirp in the spectral

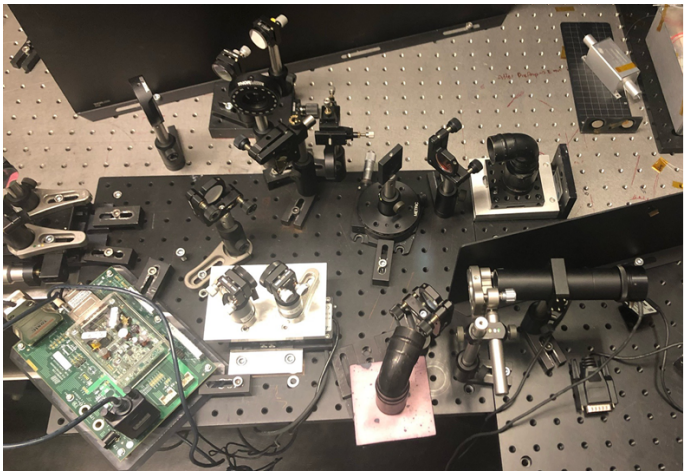

Figure 6.14: Cross-correlation setup image for the temporal pulse shaping verification.

phase and Fourier-transforming the result according to Equations 6.1, 6.2, and 6.3

$$\varphi(\omega) = \Delta L \times \beta_2 \frac{(\omega - \omega_0)^2}{2} \tag{6.1}$$

$$E(t) = \int E(\omega) e^{i\varphi(\omega)} e^{i\omega t} d\omega \tag{6.2}$$

$$I(t) = E(t)E^*(t) \tag{6.3}$$

where the β_2 is the second order dispersion coefficient of the stretcher and amplifier fibres. ΔL is the total length of the dispersing fibre ($\beta_2 \approx 2.3 \times 10^{-26} s^2/m$ is for PM980 fibre at 1039 nm).

As long as the features within a pulse are in the "far-field" then the logarithmic scaled profile of the cross-correlated trace matches directly with the spectral profile. Results of square pulse shape are presented in Figure 6.15. However, small spectral features are not stretched sufficiently and can be so close to being Fourier transform limited that their profiles require the use of Equation 6.2. Effect of these small features is visible in Figure 6.15 (b).

Then, for exploring the direction of cross-correlation traces based on the defined spectral shape, the best way was to try a single peak pulse shape and the mirror image of it as it is shown in Figure 6.16. Observances depicted that the cross-correlator reads the data at the direction of the spectral profile and in agreement with desired shape. A time domain measurement was also carried out with a high resolution 20 GHz Tektronix CSA803A communications signal analyser (CSA) and a 32 GHz bandwidth photo-detector (Agilent HP 83440D), again verifying the shape and directions besides the pulse widths.

In the next step the dynamic range measured by the cross-correlator was investigated. Double peak energy bridge (DPEB) pulses with different peak levels from 5 dB, 10 dB and 20 dB were provided and measured with the cross-correlator. Outcomes in comparison with the time domain measurements by CSA are presented in Figure 6.17, which demonstrated that a maximum dynamic range of 18 dB is feasible.

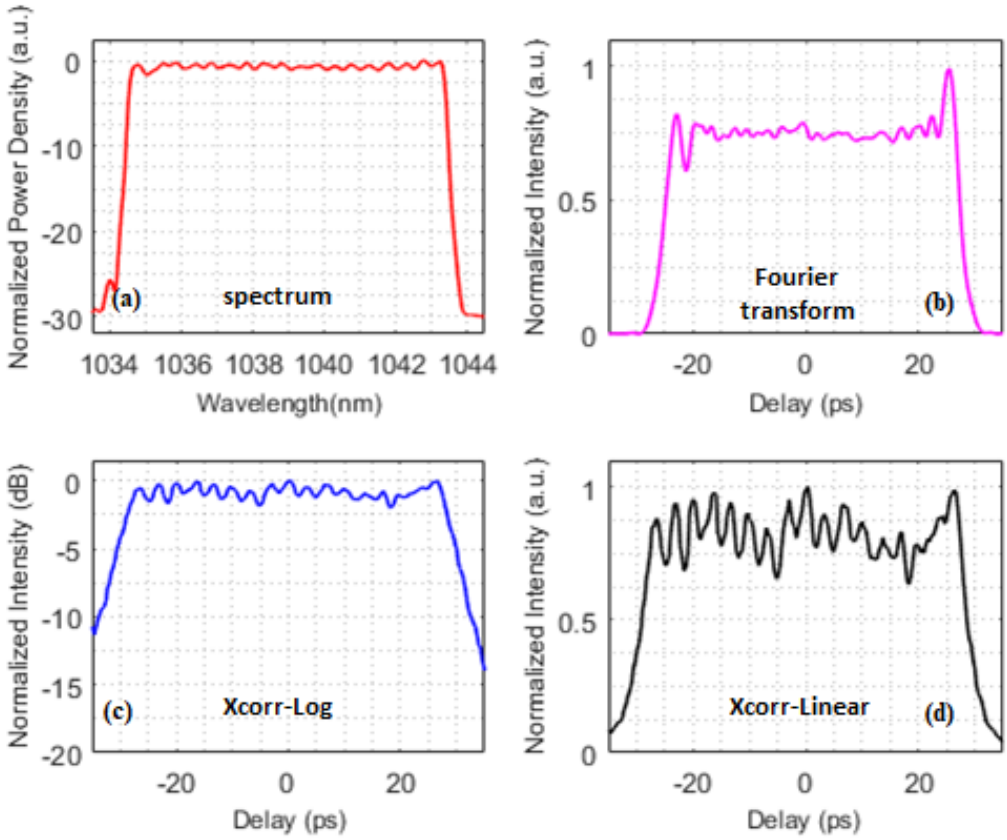

Figure 6.15: Square pulse shaping a) Spectrum, b) theoretical Fourier transform calculated pulse and measured cross-correlation data in c) logarithmic (Xcorr-Log) and d) linear (Xcorr-Linear) scales.

Then, triple-peak pulse shapes were explored to figure out the minimum possible distinguishable peak width through the cross-correlator. Moreover, this difference investigated on the spectral profile for equal peak widths of ∼12 ps and ∼8 ps as is shown in Figure 6.18 (a) and (b), respectively. The depth of ripples increased by shortening the width of pulse peaks. Therefore, based on the results in Figure 6.18 (b) shorter peak widths less than ∼8 ps attains not any more flatten peak. At this point, it is worth mentioning that due to the resolution limit of the CSA, or any other oscilloscope/detector, the middle peaks are usually undetectable while the resolution of cross-correlator does resolve them. Again here the height of peaks are deliberately chosen to be different to help distinguish the peaks (the left-side peak has ∼3 dB lower height in both shapes), otherwise they can be programmed for same amplitude.

Another interesting temporal shape is a Gaussian profile. Full width Gaussian shapes tested for different heights of 5 dB, 10 dB and 25 dB (the maximum attenuation level that can be programmed by WaveShaper). Results (Figure 6.19 (a)-(d)) are in good agreement with the targeted shapes for example for 25 dB Gaussian shape in Figure 6.19 (e) for the programmed amplitude for the WaveShaper. Maximum attenuation level for programming the WaveShaper is 25 dB while the OSNR of the signal at 400 mW output power (Figure 6.13) is close to 30 dB and therefore there is ∼5 dB difference between measured and targeted spectrum. Due to alignment imperfections of the signal coupling stage for OSA reading, an asymmetrical trace for the 5 dB height Gaussian shape is

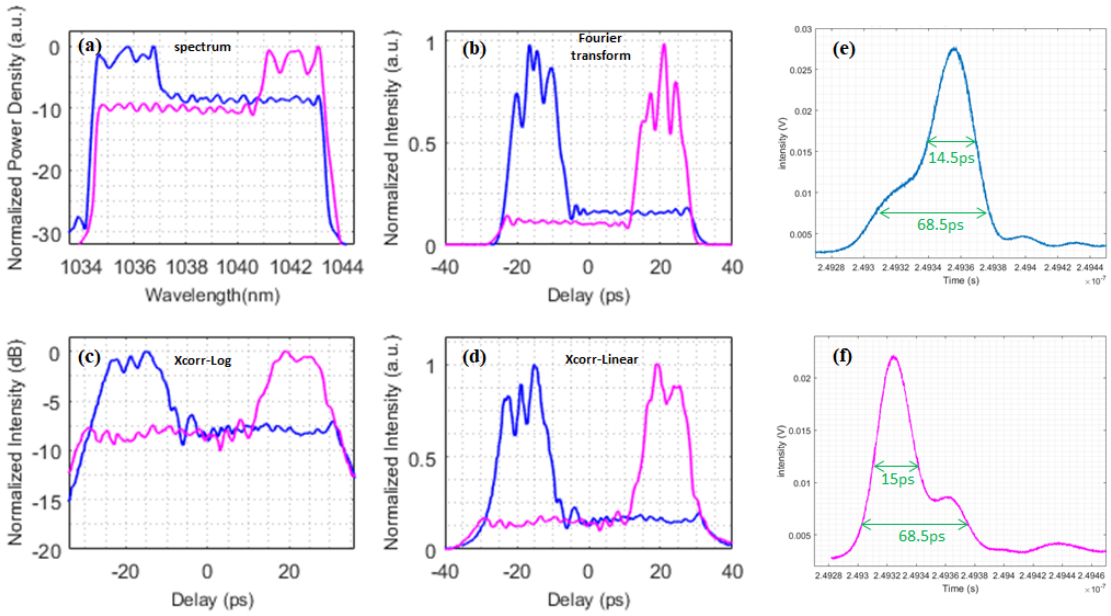

Figure 6.16: Single 10 dB peak pulse shaping a) Forward and flipped spectral profile, b) theoretical Fourier transform calculated pulse, measured cross-correlation data in c) logarithmic and d) linear scales, e) and f) showing the pulses measured by CSA.

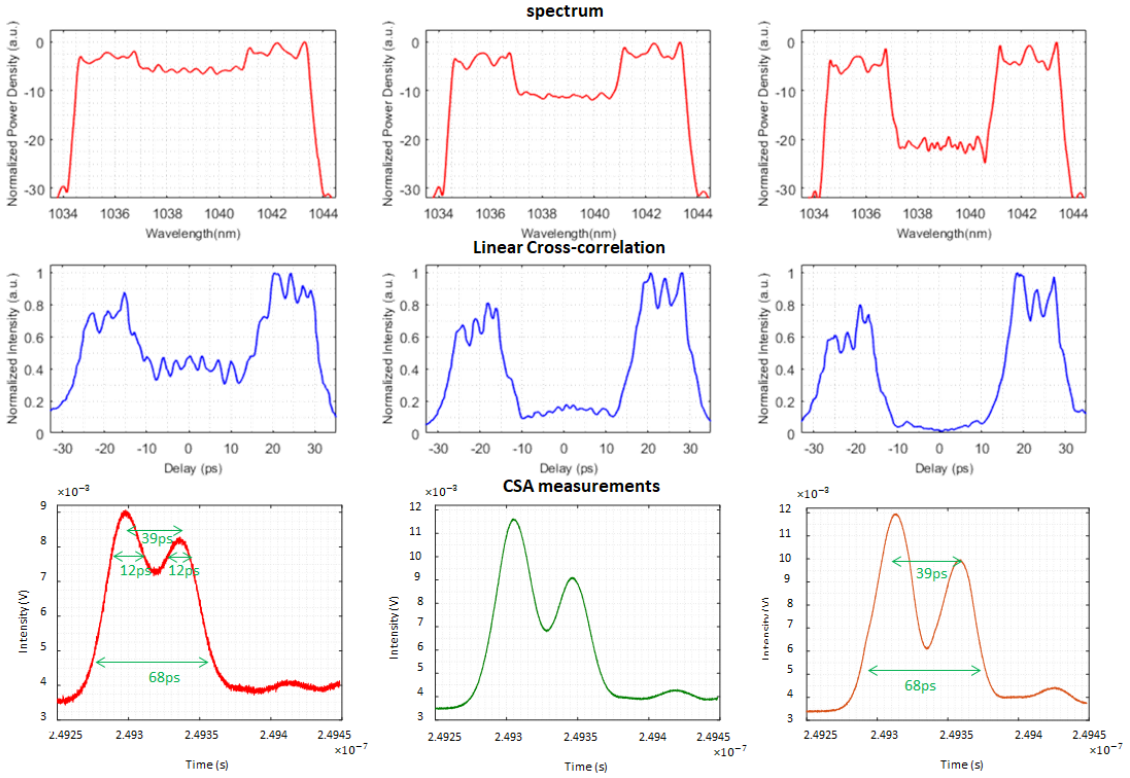

Figure 6.17: Double peak energy bridge (DPEB) pulses with different peaks' amplitude of 5 dB, 10 dB and 20 dB from left to right; and spectral profile, linear cross-correlator data and measured pulses by CSA from top to bottom rows.

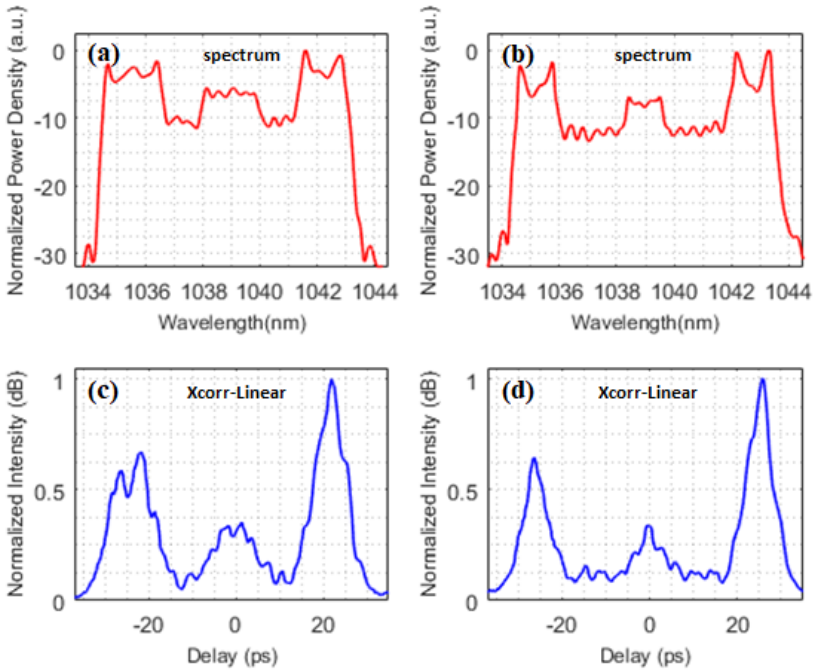

Figure 6.18: Triple 10-dB peak pulses with a) equal ∼12 ps, b) equal ∼8 ps peaks' widths and the corresponding measured linear cross-correlator data in c) and d) respectively.

visible in Figure 6.19, which is more clear in the cross-correlation result.

Furthermore, an attempt similar to flat topped pulse shapes was programmed for double, triple, and finally, a pulse train of Gaussian peaks in association with materials processing requirements, particularly the later type of pulse shape. For each of them, time domain profiles via Fourier transform calculation and cross-correlation trace comparison, showed a high level of similarity together and with the targeted pulse shapes. Both double and triple Gaussian peaks measurements in Figure 6.20 are executed for the maximum width of each peak in those profiles. Tests for peak heights of 20 dB and 25 dB resulted in more smoother spectral profiles with less effects of modulations. More reduction of the widths of each peak results in more smoother curves, since these shorter width of peaks may just pick up one or two of the modulations from the original spectrum in comparison to the full width Gaussian shapes.

Temporal pulse shaping tests continued by trying quintuple-peak Gaussian profile (Figure 6.21 (a)-(c)) as the maximum number of Gaussian peaks to be applied on the 8.8 nm spectral bandwidth, for ∼50 ps pusle width, resembling a train of pulses. To prove it, similar temporal pulse profile assessed for the half peak widths, showing the correct peak widths cannot be resolved by both Fourier transform calculation and cross-correlation trace (Figure 6.21 (d)-(f)). Even choosing lower depth intensity show that power level of the peak cannot really help to improve the results (Figure 6.21 (g)-(i)). Comparable results achieved for one single peak (step pulse) and single Gaussian peak pulse shapes, deduced that no pulses with a FWHM peak below 3 ps can be clearly shaped, while the spectral profile seems to be acceptable.

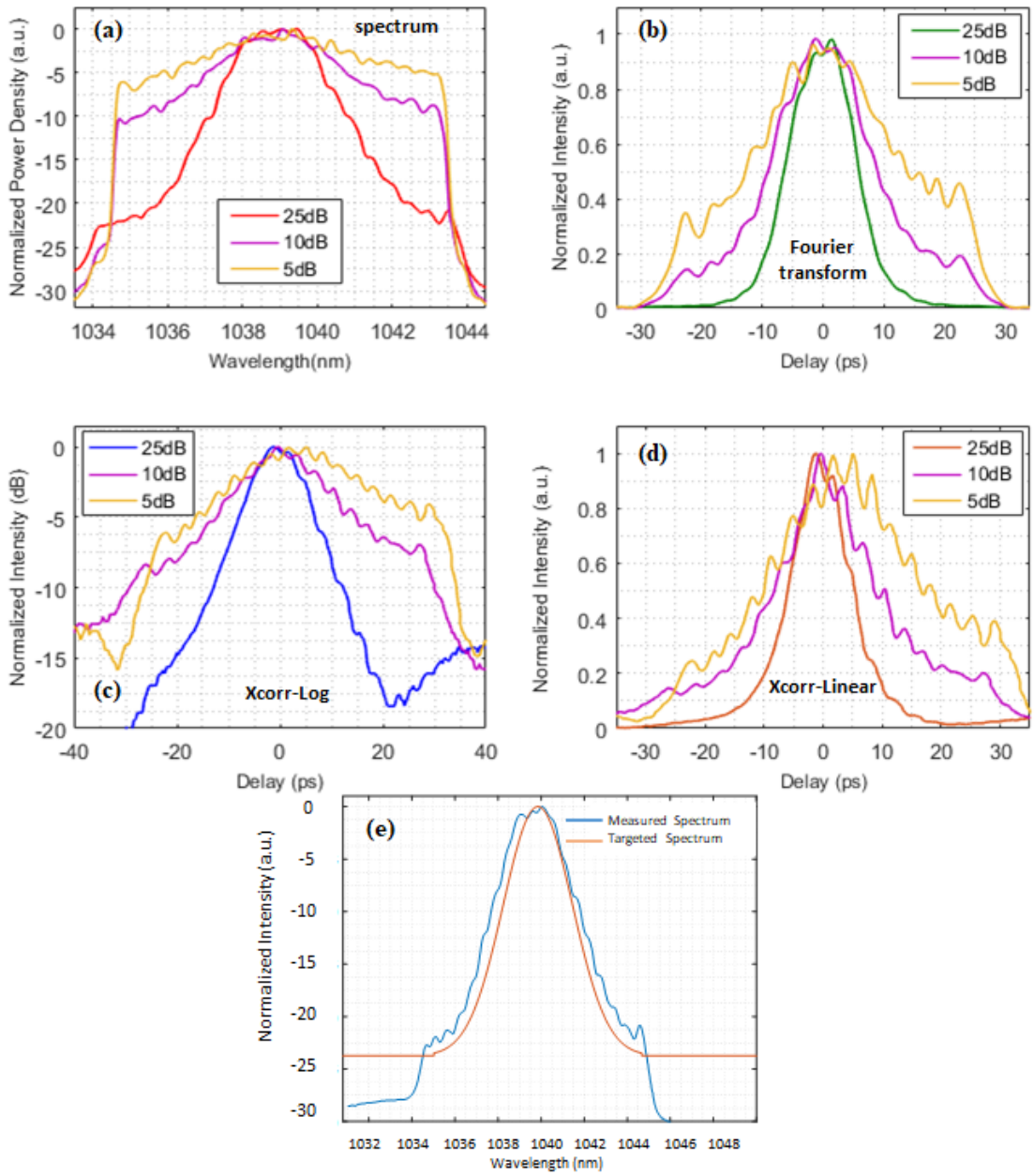

Figure 6.19: Gaussian pulse shaping with 5-10 and 25 dB peak altitude, a) Spectral profile, b) theoretical Fourier transform, c) and d) measured cross-correlation data in logarithmic and linear scales, respectively and e) the targeted programmed shape example.

Up to now, the laser setup depicted the capability and limitations for temporal pulse shaping at a power level of 400 mW. However, before power scaling through a power amplifier, a flattened spectral profile will improve the quality of the amplified spectral performances at higher power level because of the reduction in nonlinear phase shift elevation. Therefore, the output power of the second pre-amplifier stage was reduced to be ∼120 mW at the input of the power amplifier stage, still adequate for power scaling to not more than ∼10 W average output power via a gain of ∼20 dB. Additionally a combination of a half-waveplate and quarter-waveplate were adjusted when observing the trace on the OSA to minimise any polarisation beating adding to the spectral ripples.

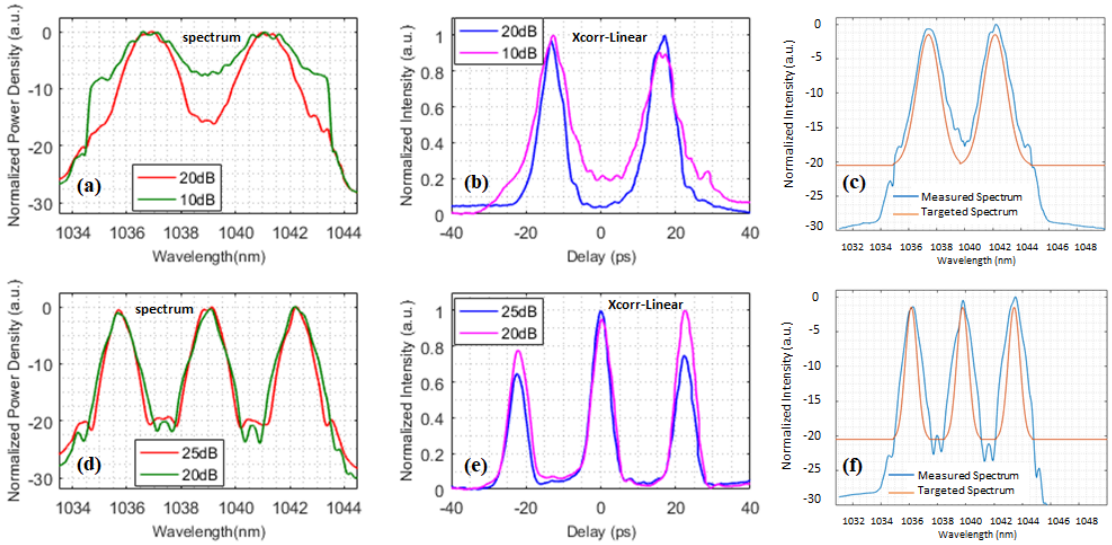

Figure 6.20: a) Double Gaussian 10 dB and 20 dB peak pulses spectra, b) cross-correlation data in linear scale, d) triple Gaussian 20 dB and 25 dB peak pulses spectra, e) cross-correlation data in linear scale, c) and f) the targeted programmed shape example for 20 dB double and triple Gaussian peak pulses, respectively.

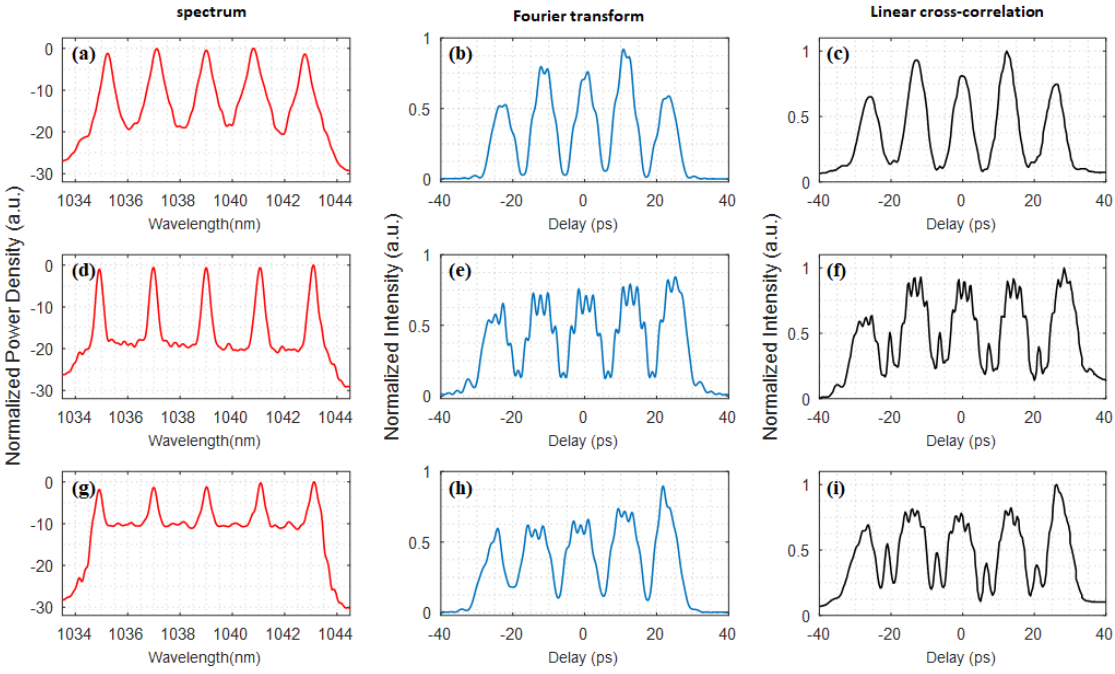

Figure 6.21: Quintuple-Gaussian-peak pulse shaping a) Spectrum of 20 dB 5 ps FWHM peaks, b) theoretical Fourier transform of 20 dB 5 ps FWHM peaks, c) linear cross-correlation data of 20 dB 5 ps FWHM peaks, d) spectrum of 20 dB 2.5 ps FWHM peaks, e) theoretical Fourier transform of 20 dB 2.5 ps FWHM peaks, f) linear cross-correlation data of 20 dB 2.5 ps FWHM peaks, g) spectrum of 10 dB 2.5 ps FWHM peaks, h) theoretical Fourier transform of 10 dB 2.5 ps FWHM peaks, i) linear cross-correlation data of 10 dB 2.5 ps FWHM peaks.

6.3.1.6 Power Amplifier Stage

The final amplifier comprises a 2.5 m long few-mode PM-YDF (Nufern PLMA-YDF-25/250-VIII) with a core diameter of 25 μm (NA=0.075), and an inner cladding diameter of 250 μm (NA=0.46). The pump beam was provided by fibre-coupled 975 nm 50 W IPG laser diodes, was free-space coupled into the YDF fibre in a counter-pumped configuration. Both ends of the fibre were spliced to endcaps with a diameter of 250 μm and a length of ~1.5 mm to suppress parasitic oscillations and to prevent optical damage at the air-silica interface. The input end facet was flat-cleaved, and the output end facet was angle-cleaved with an angle of ~8 degree. A beam quality of M^2 ≈1 was measured at the output of the power amplifier stage with the beam waist of 120 μm as it is illustrated in Figure 6.22. Dr. Di Lin as an authorised high power project member helped me to build this stage.

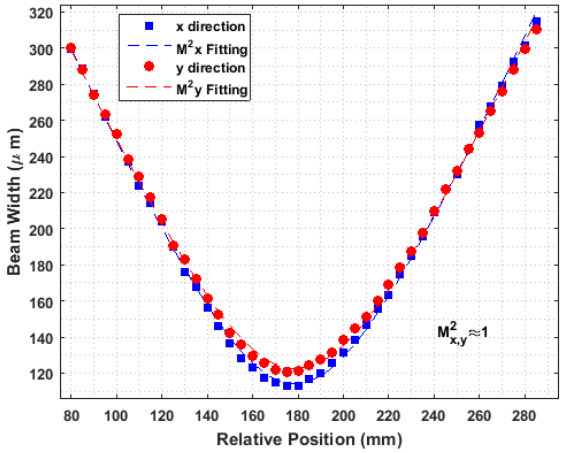

Figure 6.22: Measured beam quality.

6.3.2 Performance of the Laser System

After having the full configuration of the laser system, the power amplifier pumped ~20W to scale the average output power to 10.5 W at a gain of 19.4 dB (Figure 6.23). Corresponding to a maximum pulse energy of 450 nJ at the repetition rate of ~23.2MHz.

The peak power reaches close to 7.84 kW, which introduces nonlinear phase shift beyond 2π that highly modulate the spectrum, as illustrated in Figure 6.24. The ripple of ~3.5 dB was unacceptable and worsened when shaped pulses were used as is shown in the following section.

6.3.2.1 Temporal Pulse Shaping Results After Power Amplifier

Performance of the power amplifier stage for temporal pulse shaping was first carried out by amplifying the shaped output spectral profile at the end of the second pre-amplifier stage. Therefore, the resulted spectrum at the power amplifier stage was recorded step by step by increasing the pump power to produce up to 10 W average output power. Resulting shapes for the power levels from 2 W to 10 W of a square and single-peak pulse for a 120 mW input power level are shown in Figure 6.25 (a) and (b), respectively. Even though the square pulse shape before insertion to the power amplifier stage is

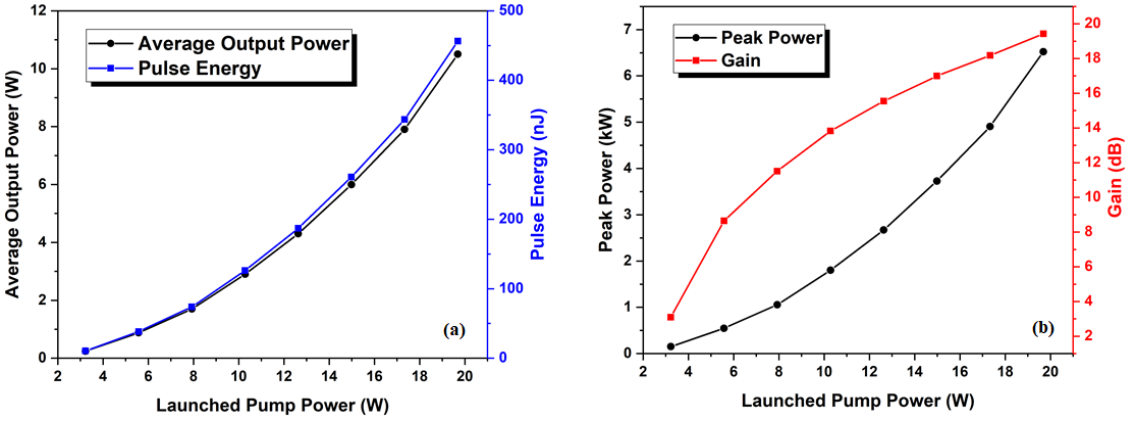

Figure 6.23: Mode-locked MOPA laser system average output power, gain, peak power and pulse energy versus the total launched pump power.

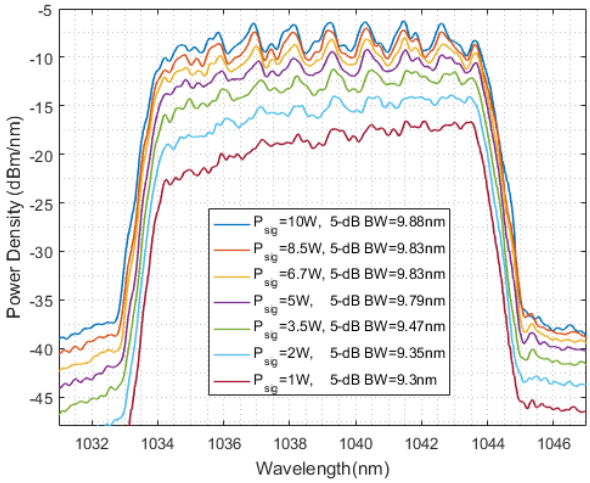

Figure 6.24: Spectral characteristics of power amplifier stage at different total launched pump power levels.

almost flat, the amplified spectra in Figure 6.25 (a) suffer large ripples in the spectral regime. Also, strong ripples can be observed on the spectral characteristics of the laser, for the single-peak pulse even though the peak width is chosen to be around 50% of the total pulse width. It is while owing to lower available peak power under the peak, it should result in a less modulated peak after shaping . The results depict the effect of SPM on the peak by appearance of a second peak (spectral cut) on the spectra as the power increases. The shaped Gaussian pulse produced a similar effect as shown in Figure 6.25(c).

Consequently, the pulse shaping feedback control loop should be used **after** the final output as it is drawn in Figure 6.10. The shaping program was tested for a single peak and Gaussian pulse shapes at 5 W and 10 W average output power levels (Figure 6.26 (a) and (b), respectively). Even after running more iterations of the feedback loop, the pulses remain distorted and the ripple ranges exceed 10-15 dB. That chaotic shaped result is more vivid in Gaussian shaping attempts at 10 W average power, where the result has no relation to the target shape (reddish curve in Figure 6.26 (b)) or the apex surpasses

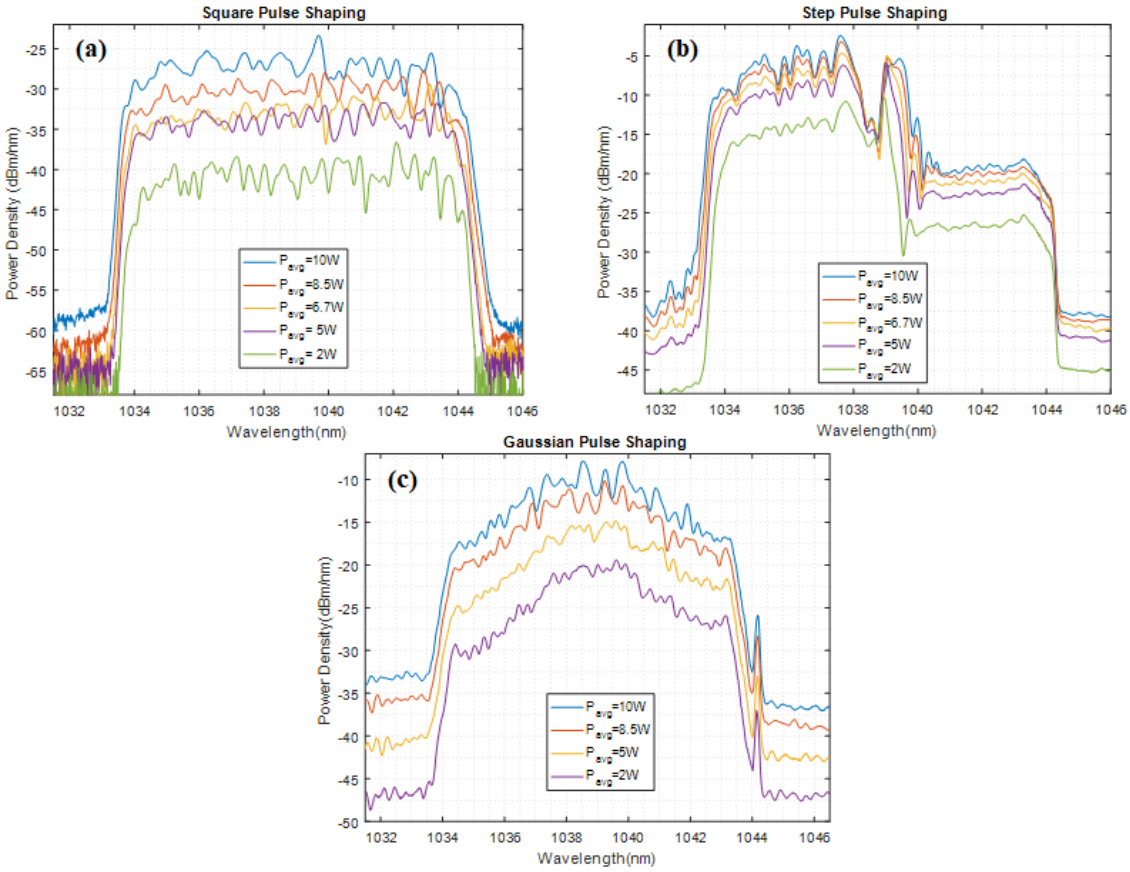

Figure 6.25: Temporal pulse shaping at different pump power of the power amplifier stage after shaped spectrum in second pre-amplifier stage for a) square, b) single peak and c) Gaussian pulse shaping at 2 W to 10 W average output power.

the attenuation level of WaveShaper despite the extra modification in the program like the blue curve in Figure 6.26 (b). Although Gaussian pulse shaping at 5 W power level is still achievable, the single peak pulse shape is corrupted.

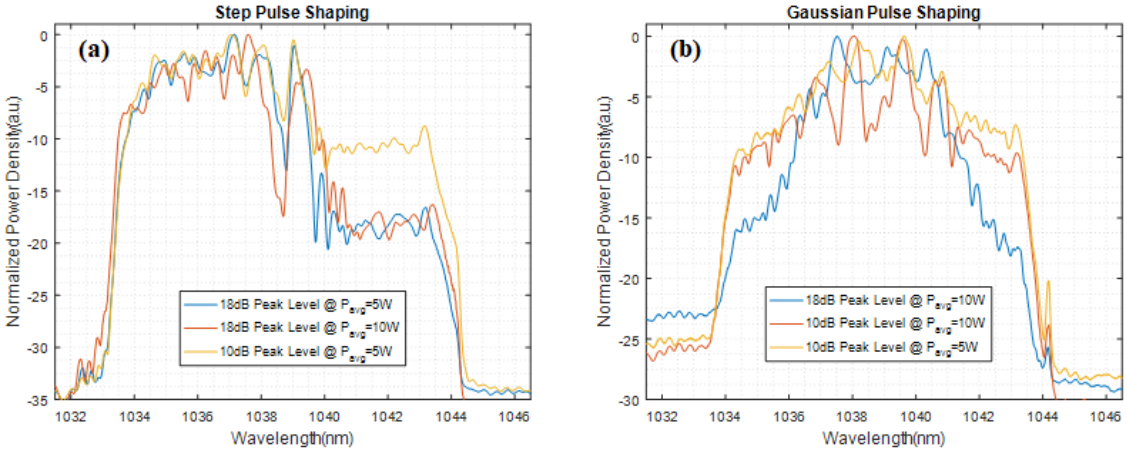

Figure 6.26: a) Single peak and b) Gaussian temporal pulse shaping at 5 W and 10 W average output power after power amplifier stage.

The total B-integral of the system (subsection 3.3.2.1) was calculated to be $\sim 6.72\pi$ (2.04π, 0.478π, 1.62π, 0.355π, 0.145π, and 2.08π from mode-locked laser source, 20% tap output, fibre stretcher, first pre-amplifier, second pre-amplifier and power amplifier, respectively). So, the MOPA laser system is operating with a nonlinear phase shift higher than 6π. The high peak power from the MOPA results in the high B-integral value for the laser and escalation of the unwanted ripples on the spectrum, which are originally created at the output of the mode-locked oscillator. Therefore, it might improve the laser performance if the seed is replaced by a femtosecond laser source operating with smoother spectra and high repetition rate to reduce the introduced peak power in the MOPA.

6.4 Conclusion

The first low power picosecond pulse shaping experiments were reported in this chapter. Using a home-made stable self-starting 1039 nm passively mode-locked laser amplified in an all fibre MOPA. The average power of the output signal reached 10 W. However, the ultimate purpose of the project is to increase the power to the 100 W regime, which resulted in poor spectral profiles and correspondingly very chaotic and disordered pulse shapes. The assumption was that SPM is limiting the probability of power scaling for temporal pulse shaping. Attempts to solve it were not successful. The B-integral calculation revealed that the laser source plays the dominant role in nonlinearity effects. Therefore, we must look for another laser source with smoother spectrum as are discussed in the next chapter.

Chapter 7

Picosecond Spatio-Temporal Pulse Shaping Using Femtosecond Based Picosecond System with Smoother Input Spectra

Demonstration of arbitrary picoseocnd temporal pulse profiles in a fully-fiberised Yb-fibre MOPA with radial polarisation, at the highest reported average output power compatible with the needs of our end users on the ERM project, is described in this chapter. The revised laser system configuration after insertion of a commercial femtosecond laser with smoother spectra in comparison to the house-built mode-locked laser is explained and analytical investigations by calculation of B-integral evolution carried out to show how the further power scaling is limited.

7.1 Introduction

Using a borrowed commercial NKT laser for a quick demonstration of temporal pulse shaping at the 10 W average output power level, a substantial reduction in the severe spectral ripples could be achieved, compared with the in-house built seed laser in previous chapter. The shorter pulse width and almost double repetition rate, at a similar seed average power as our mode-locked oscillator, resulted in lower peak power and B-integral, which decreases the SPM effects in the MOPA, allowing temporal pulse shaping at increased powers. Therefore, it was decided to use that source instead of my own mode-locked laser. In this chapter we report the demonstration of the temporally shaped square, stepped, multi peaks, Gaussian and a train of Gaussian pulses, amplified to an average power beyond 50 W over a total pulse width of 70 ps, alongside generation of a radially polarised doughnut-shaped beam.

7.1.1 Challenges from Home-made Mode-locked Based Laser and Initial Results with NKT Laser Source

Implementation of temporal pulse shaping after power amplifier stage running at 10 W average output power using the home-made mode-locked laser shown in Figures 6.25 and 6.26 resulted in distorted spectral profiles. A NKT ORIGAMI laser operating at 40 MHz repetition rate with an output power of 25 mW provided smoother spectrum (maximum 0.5 dB ripple depth) replaced the mode-locked laser source. Figure 7.1 (a)

shows the comparison of both laser spectra. The insert figure shows the spectral behavior just around the 3-dB bandwidth of both sources.

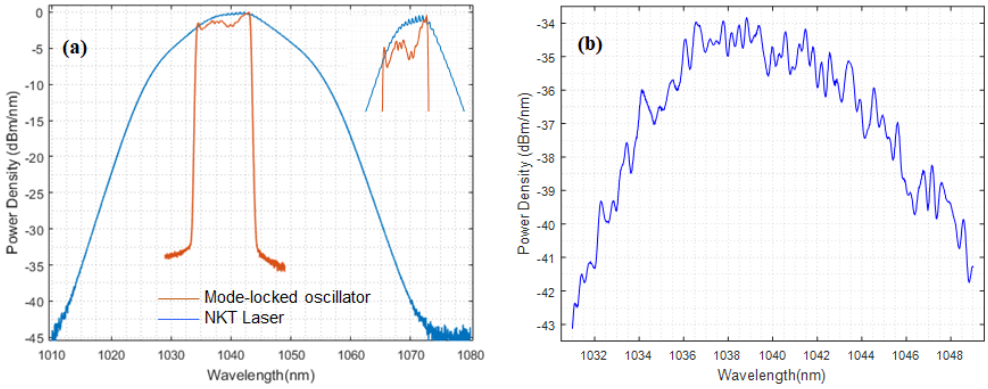

Figure 7.1: a) Comparison of the home-made mode-locked laser source optical spectra and the NKT laser. The insert shows corresponding spectra around 3-dB bandwidth, b) Amplified spectrum for the ORIGAMI laser measured at 10 W average output power.

Seeded by the NKT laser source, we tested the MOPA at 10 W average output power, which displayed <1 dB maximum ripple depth on the spectrum (Figure 7.1 (b)). Based on the much improved demonstration using the commercial laser source, it was decided to try advanced temporal shaping at higher average output powers, beyond 5 W. This required limiting the spectral bandwidth to 10.5 nm (the NKT laser source had 13 nm 3-dB spectral bandwidth), as the widest square pulse bandwidth that could be carved without excessive power loss.

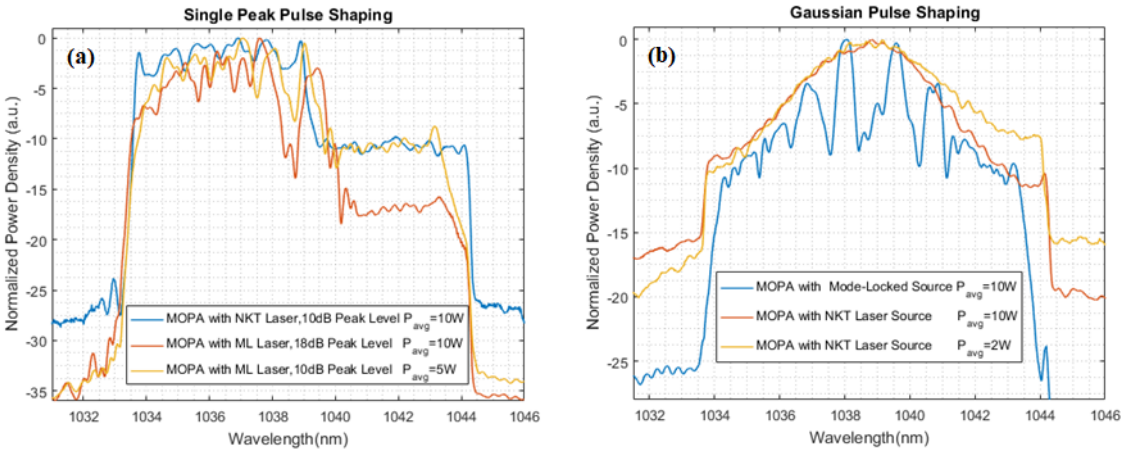

Figure 7.2: Comparison of shaping results using the home-made mode-locked laser source and the commercial one a) Direct single peak pulse shaping at 5 and 10 W and when the shaped output of the second pre-amplifier stage is pumped for 10 W power, b) Gaussian shaping with 10 dB altitude of the bell shape.

For temporal single-peak pulse shapes at 10 W average output power level (Figure 7.2 (a)- blue curve), much less modulation on the spectral profile was again observed compared with the spectra at 5 W average output power when the seed was the home-made 1039 nm mode-locked seed laser (Figure 7.2 (a)- yellow curve). The ripple is reduced

by a factor of 86% at 10 W compared to running the MOPA with the mode-locked seed laser (Figure 7.2 (a)- red curve). Similarly smoother spectra were observed for Gaussian pulse shaping with 10 dB bell-shape amplitude presented in Figure 7.2 (b). Therefore, with the improved seed, full characteristics of performance of the MOPA system for spatial and temporal pulse shaping at a power level >50 W could be pursued.

7.2 Spatio-Temporal Pulse Shaping MOPA System with Low Peak Power Femtosecond Seed

The full picosecond-pulse Yb MOPA was configured as is shown in Figure 7.3. A commercial femtosecond 1030 nm mode-locked laser oscillator running at 100MHz repetition rate seeds a three stage Yb-doped fibre amplifier. As previously, to have sufficient pulse duration for temporal pulse shaping, a length of fibre was needed to stretch the pulse to ~70 ps. A computer-controlled temporal shaping loop via a WaveShaper at the front-end, is following feedback from a verification setup for the temporal shaping using a cross-correlator after the final power amplifier. Spatial shaping is achieved using an S-waveplate placed after the Yb-fibre power amplifier stage.

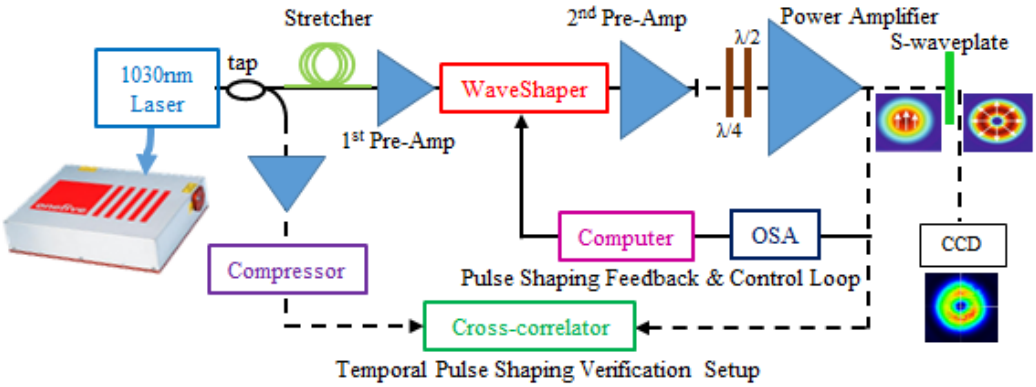

Figure 7.3: Schematic of the picosecond Yb-fibre MOPA laser system.

Except for the oscillator, the stretcher and the chain of amplifiers are the same applied in the 1039 nm mode-locked MOPA, described in previous chapter. That said, the change of the laser source required some minor modifications in the setup as explained below.

7.2.1 Laser Source Characteristics

The NKT laser in Figure 7.3 had a central wavelength of 1030 nm. It was a loan unit and the 1039 nm fiberised unit was being fixed by NKT at the time I performed these experiments. It had ~200 fs transform-limited soliton pulses with 3-dB bandwidth of 13 nm at a repetition rate of 100 MHz and total average output power of 200 mW delivering 10 kW peak power.

To operate the laser with the smoothest possible spectrum, especially after power amplification, only 35 mW of the available seed power was coupled into the PM980 patch cord fibre. The 2 m length of patch cord increased the pulse width to 1.45 ps (Figure 7.4 (a), assuming Gaussian pulse shape for an inferred pulse width of 2.05 ps). Further,

the single-peak characteristic of the laser measured by a RF spectrum analyser (Agilent E4446A), is shown in Figure 7.4 (b).

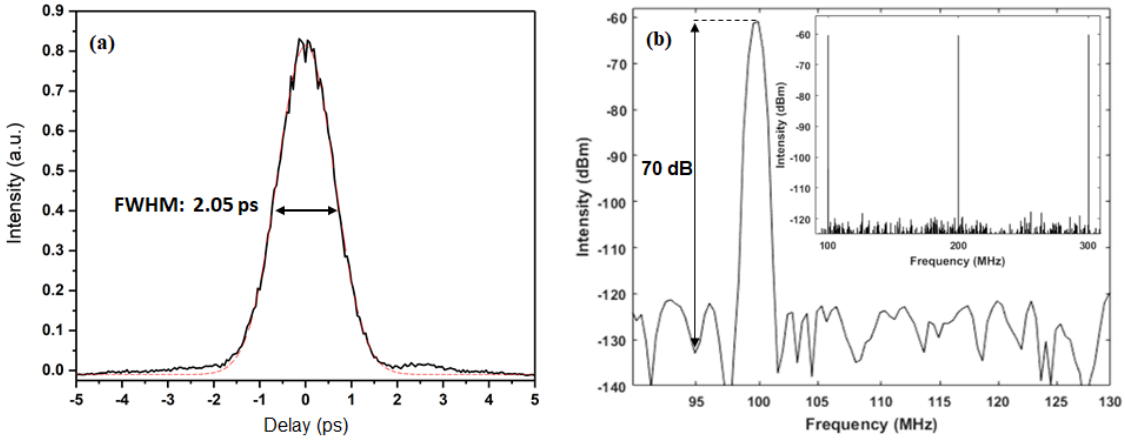

Figure 7.4: a) Seed pulse width after coupling to the 2 m PM980 patch cord fibre. b) RF spectrum at the fundamental frequency of 100 MHz. Inset: RF spectrum for 200 MHz repetition rate.

7.2.2 MOPA Chain Characteristics, Limitations for Temporal Pulse Shaping in Power Scaled Scheme and Solutions

After the first pre-amplifier stage an average power of ∼20 mW was measured, resulting in 5.2 mW average power level after the WaveShaper. It is worth mentioning that since this pre-amplifier was designed for 1039 nm central wavelength and provides a gain at longer wavelength regime the gain shifted the peak to 1036 nm (Figure 7.5), which fortunately red shift the spectrum further inside the WaveShaper transmission band, which extended down to 1019 nm.

An average output power of 140 mW was measured after the output isolator to be coupled into the final stage. To achieve higher average output powers, the final amplifier now required more pump diodes than the stage presented in chapter 6. Therefore, a chain of four fibre-coupled 975 nm 50 W IPG pump laser diodes coupled into the YDF fibre in a free-space counter-pumped configuration.

Operation of the laser at the repetition rate of 100 MHz for temporal pulse shaping only enabled us to achieve a maximum power level of 20 W before an extensive range of ripples began distorting spectral profiles. The repetition rate of the laser was then doubled through a 50:50 coupling configuration to enable temporal pulse shaping beyond 20 W average power level. Two 3-dB couplers were joined together while the fibre length in one junction point is approximately double the other one to emerge an intermediate signal amplitude, duplicating the number of pulses at the output of two couplers due to the delay, as illustrated in the dashed box in Figure 7.7. Then the laser operates at 200MHz repetition rate (Figure 7.6). A slight amplitude difference might be due to the fibre splices making not a perfect power handling to each port of the second 50:50 coupler or the couplers not having an exact 50:50 splitting ratio. Therefore, slightly more than 1 m fibre length added in one junction.

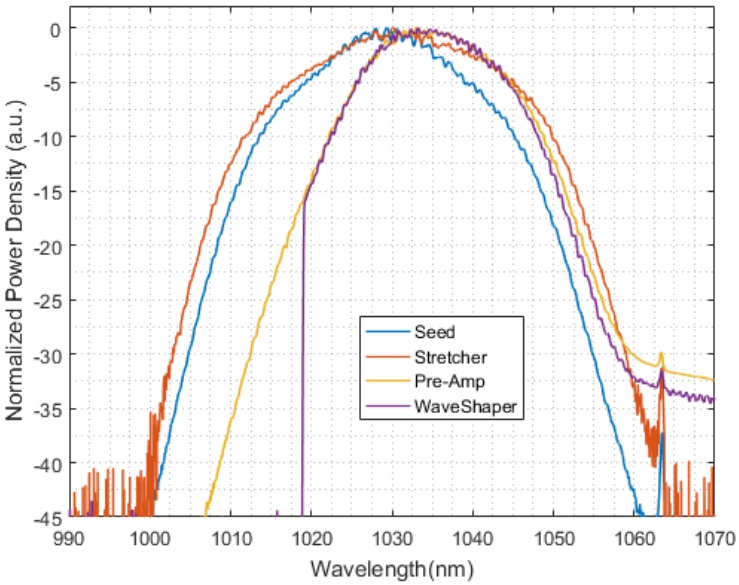

Figure 7.5: Spectral characteristics of the laser source, stretcher, core-pumped amplifier stage and WaveShaper after NKT laser source insertion.

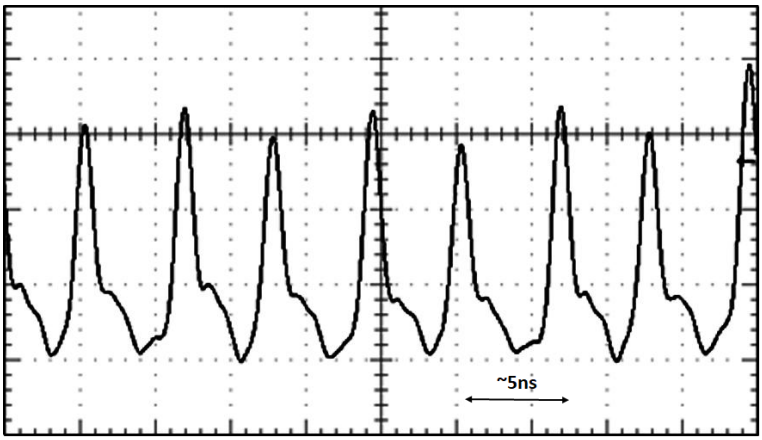

Figure 7.6: Image of the doubled repetition rate of the NKT laser source from an oscilloscope.

The final laser system configuration was altered as illustrated in Figure 7.7. This enabled a maximum average output power level of 51 W (pulse energy of 255 nJ) and 25.5 dB gain, resulting in a peak power of 3.64 kW at 70 ps pulse width to be achieved. The final amplifier had ∼54% slope efficiency in relation to launched pump power (Figure 7.8). This low power conversion efficiency is attributed to incomplete pump absorption in the short amplifier length, which was chosen to maximise gain at 1030 nm. The efficiency with respect to absorbed pump power was more respectable, 70%. The polarisation extinction ratio (PER) was 12.5 dB. Spectral characteristics of the power amplifier stage output at 1035 nm central wavelength and repetition rate of 200 MHz are demonstrated in Figure 7.9.

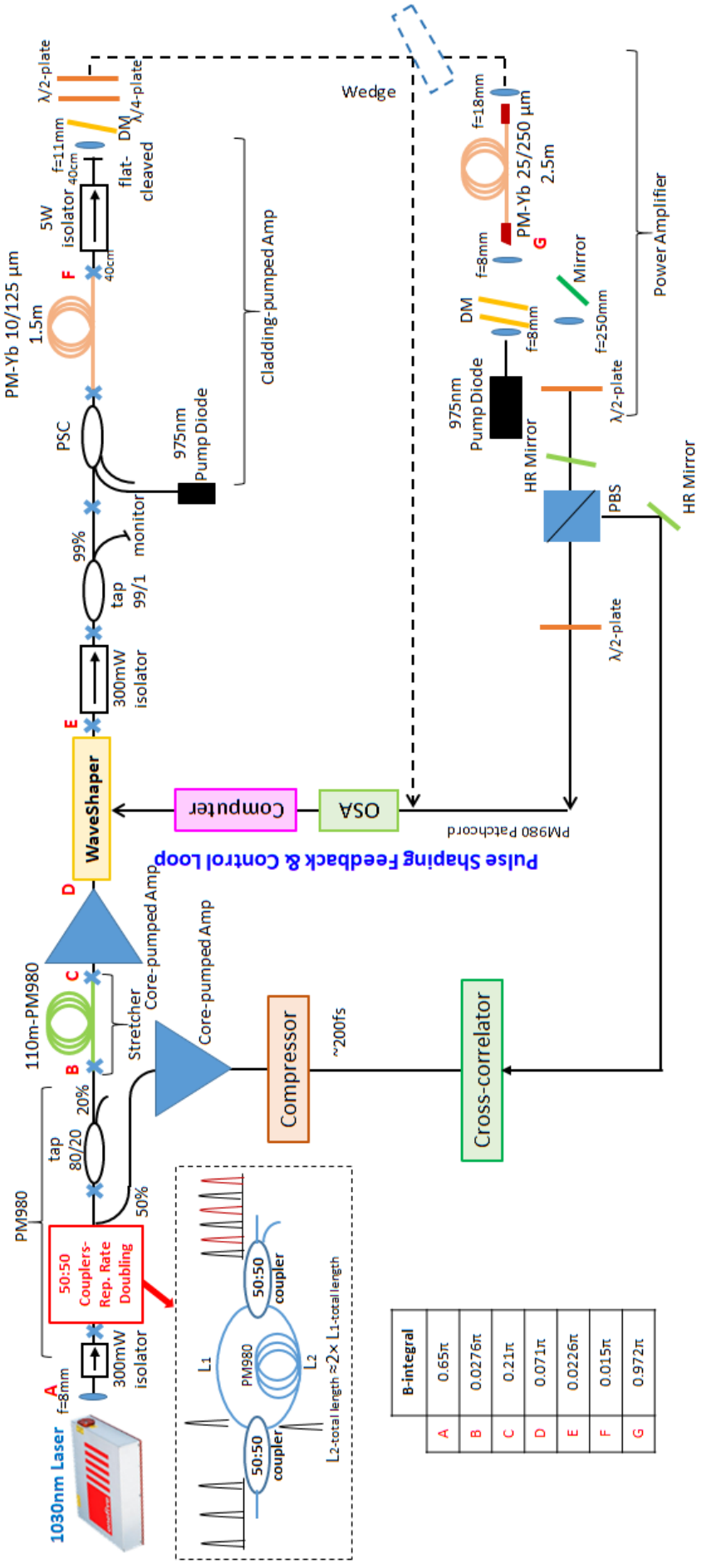

Figure 7.7: Full picosecond experimental setup including temporal diagnostics.

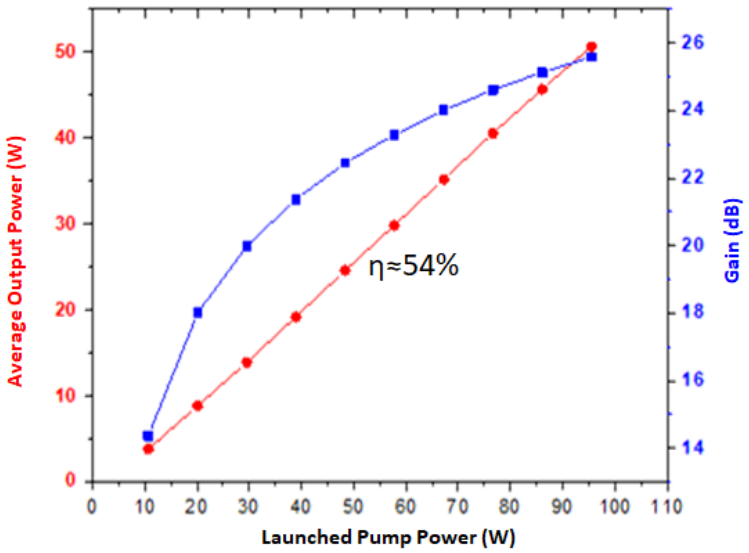

Figure 7.8: Average output power and gain of the laser after power amplifier stage versus the total launched pump power.

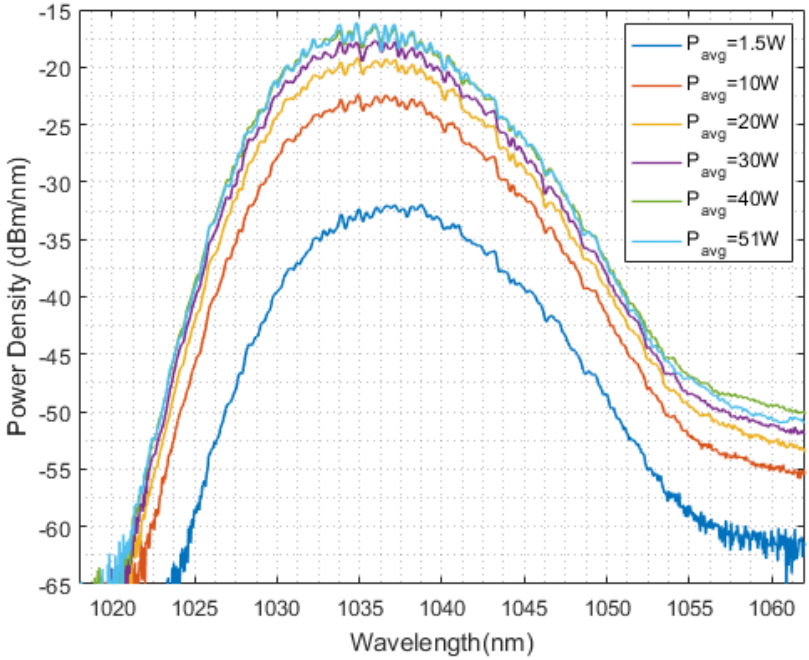

Figure 7.9: Spectral characteristics of power amplifier stage at different output power levels.

Figure 7.10 illustrates an image of the entire MOPA system including the cross-correlator. The configuration includes the mode-locked (ML) seed, first pre-amplifier stage, stretcher, WaveShaper (at top row of the image) and the second pre-amplifier stage and power amplifier in the bottom line, besides the diagnostic setup consisting of the compressor and the cross-correlator. This laser system has the feasibility to be exploited in any desired application as a compact laser source. The cross-correlator and compressor segments were constructed for the labs only as there is no requirement to include them in the portable laser.

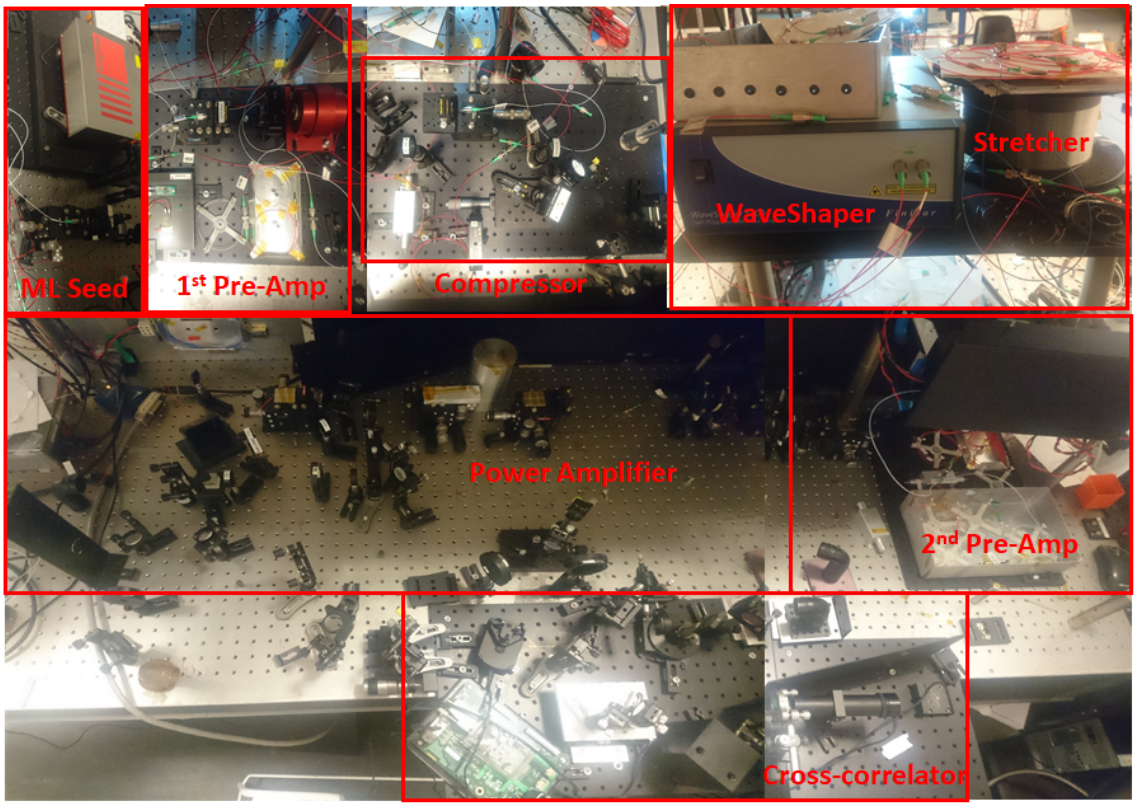

Figure 7.10: Full laser system image including the mode-locked (ML) seed, NKT laser.

7.2.3 Temporal Pulse Shaping Results

In this section we discuss the temporal shaping of the amplified output beam at 51W average output power level. First of all, two possible shaping methods were tried. One running the controlled loop for every pump power level (Figure 7.11 (a)), and the other, just one running the loop at a lower average output power and then ramp up the amplifier stage and scan the spectral behavior of the laser up to 51 W (Figure 7.11 (b)). In order to better understand the ripple range reduction on the spectra, tests were applied for square-pulse shaping at 11.5 nm spectral bandwidth. Evaluation of ripple levels with respect to a perfect flat-top squared shaped pulse, in respect to the increase of average output power levels, were measured (Figure 7.11 (c)). For powers beyond 50 W, the modulation depth exceeds 5 dB, which restricts further power scaling in temporal pulse shaping implementation. Also, trying more iterations in the shaping code showed no improvement.

With taking into account the maximum possible power scaling up to 51 W, the laser system was ready to carry out further temporal pulse shaping within the 11.5 nm spectral bandwidth with corresponding duration of ∼70 ps measured by the cross-correlation trace. Running the cross-correlation measurement for higher average powers than 20 W burned the silver mirrors in the cross-correlator system. Therefore, they were replaced by high reflectivity 1 μm dielectric mirrors (HR@1 μm). The reference compressed pulse was taken at the free output port of the repetition rate doubling section, had ∼200 fs pulse width as shown in Figure 7.12.

The effect of power scaling on the quality of the Gaussian shaped pulse was

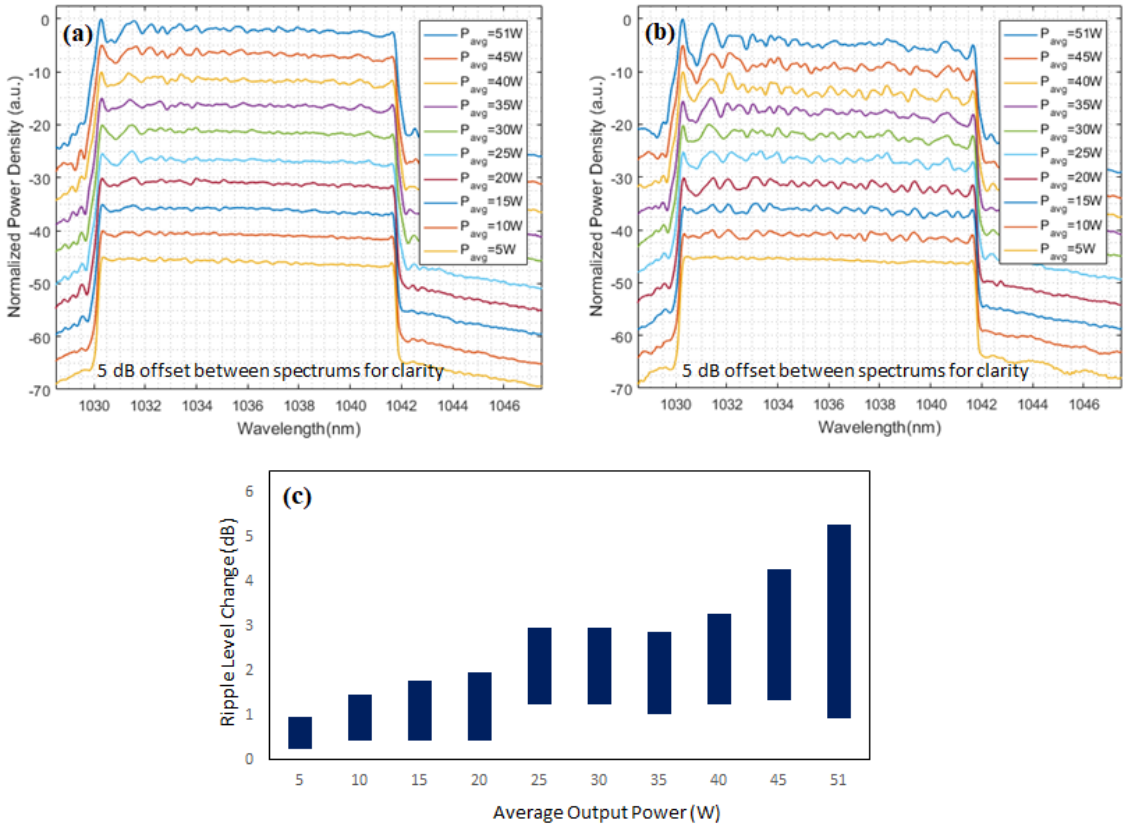

Figure 7.11: Square pulse shaping a) at different average power levels, b) after shaped laser at 5 W average power and c) comparison of ripple level changes with respect to a perfect flat-top shape in respect to the increase of average output power levels.

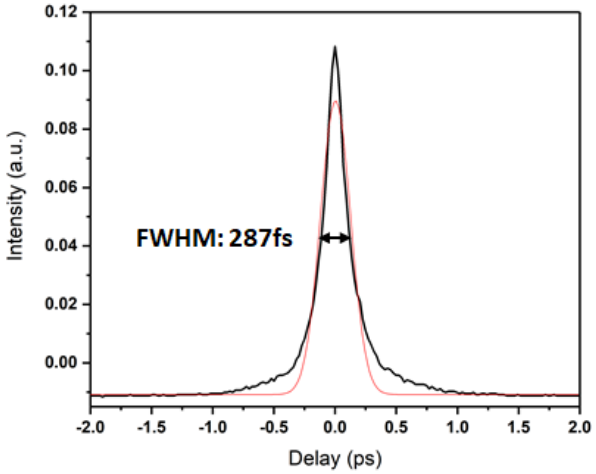

Figure 7.12: Autocorrelation trace of the compressed pulse with Gaussian fitting.

investigated. In Figure 7.13 Gaussian temporal-pulse profiles are compared at output powers of 20, 30 and 51 W. Figure 7.13 (a) shows the spectral comparison that power amplification introduces an increase in the depth of the spectral fluctuations. Calculated Fourier transform from the spectral profiles (Figure 7.13 (b)) are match well with the cross-correlator traces in Figure 7.13 (d) providing the desired Gaussian pulse

profiles. In order to have a complete comparison the log-scaled profile of the cross-correlation measurements are presented in Figure 7.13 (c). Figure 7.13 (a) and (b) include the input spectral profile to the final amplifier for a better comparison.

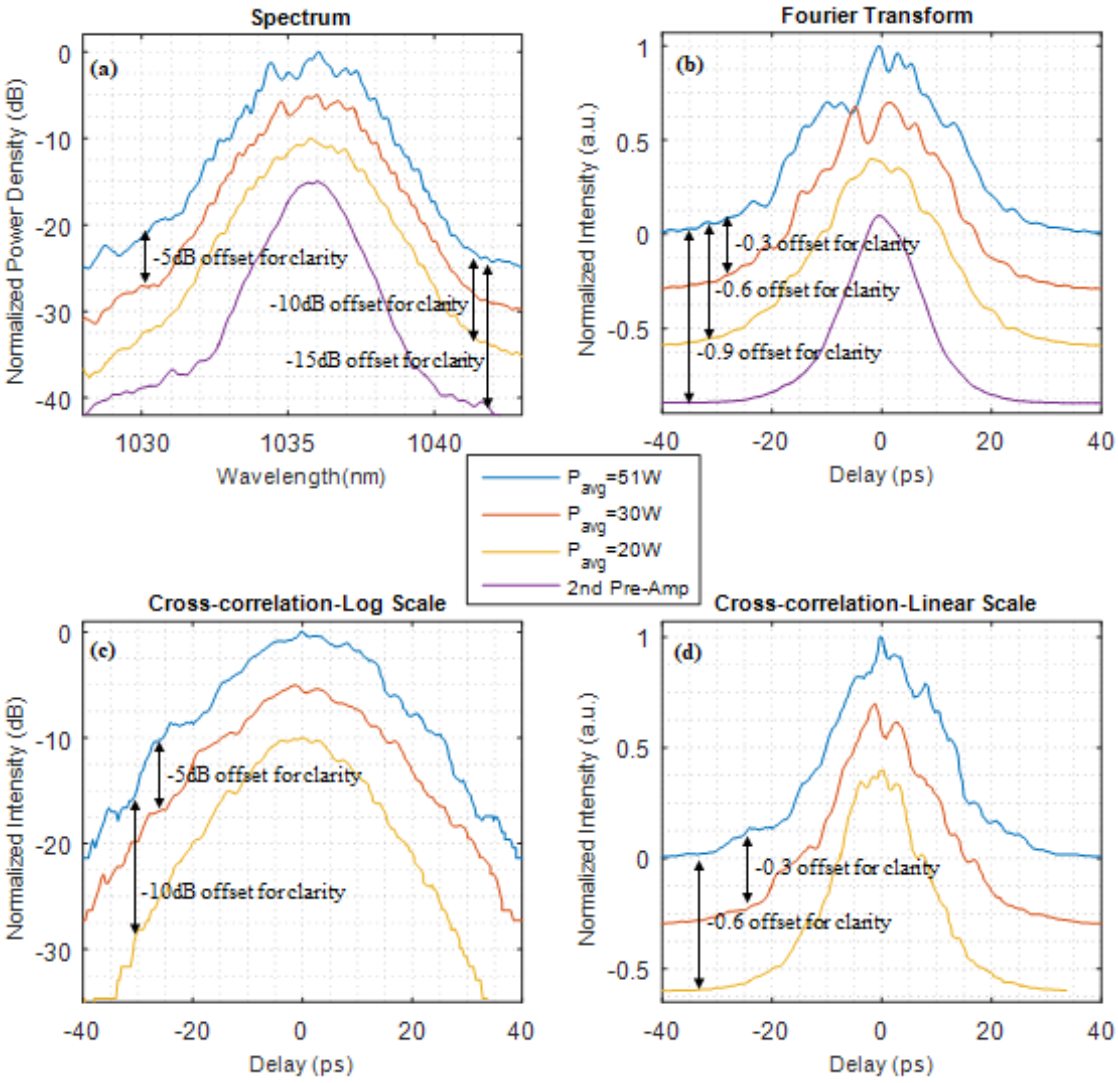

Figure 7.13: Amplification of Gaussian pulses with output powers of 20, 30 and 51W. a) spectra plotted on a log-scale; also included is the input spectral profile to the final amplifier, b) pulse profile calculated from the measured spectra and the dispersion of the fibres and shown on a linear scale, c) cross-correlation data: logarithmic scale, d) cross-correlation data (linear scale).

The shaping results of a set of different temporal pulse profiles at 51 W amplified output power beam for square pulse, single-peak pulse, double and triple peak pulses with energy bridge (DPEB and TPEB), and a quintuple Gaussian pulse are depicted in Figure 7.14. Spectral pulse profile, calculated Fourier transform and the measured cross-correlation data are presented in the first, second and third columns, respectively. Different peaks intensity levels are considered for the single-peak, double-peak and triple-peak pulses to display the capability of the temporal pulse shaping at any requested average/peak power level and pulse width. However, the limits of pulse width are investigated in order of gaining less affected spectrums by ripples and also the temporal detection by the cross-correlator. Pulse durations of less than 5% of the total

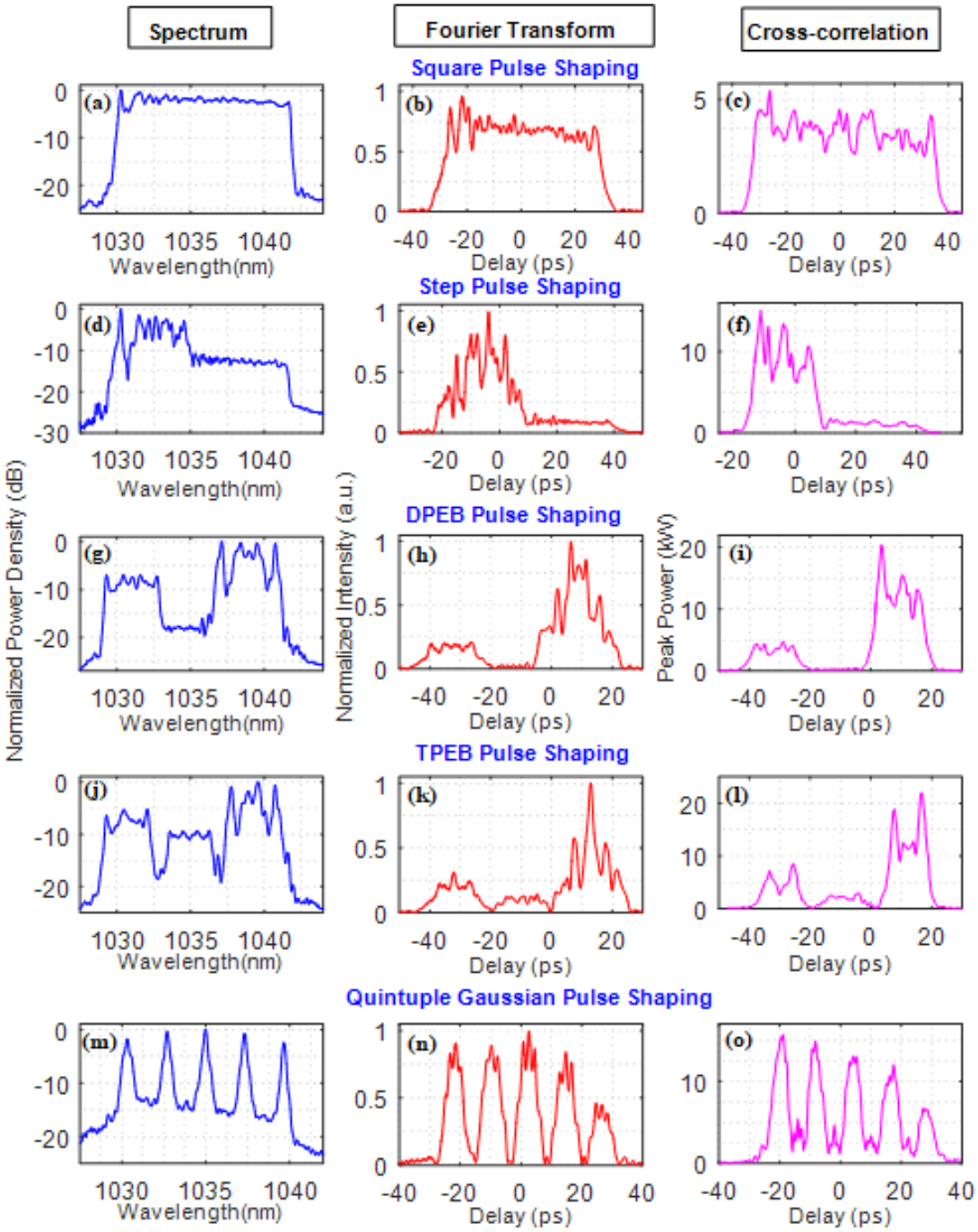

Figure 7.14: Square, square pulse, step pulse, double peak energy bridge (DPEB) pulse, triple peak energy bridge (TPEB) and a burst of 5 Gaussian pulses. All data were recorded at the maximum ∼51 W average power level. Column 1 shows spectra. Column 2 shows calculated pulse profile. Column 3 shows the measured cross-correlation traces (linear scale) for comparison.

pulse width suffer from spectral fluctuations due to higher peak power and the effect of higher nonlinear phase shift.

The spectral profile of square-shaped temporal pulse is flattened with the shaped bandwidth from 1030 nm to 1041.5 nm and a ∼2.5 dB difference between the maximum and the minimum value of ripples.The short wavelength edge of the spectrum is sitting

at the central wavelength of the seed, with higher peak power, which results in higher nonlinear phase shift. Running more iterations of the algorithm failed to minimise the modulation depth on the spectrum.

The single-peak pulse in Figure 7.14 (d) was shaped for a 25% width at 10 dB intensity of the total power density profile. For the double-and triple-peak pulses the same pulse widths considered. The former one with 10 dB difference in intensities and the latter one with 5 dB difference between the first and third peaks counting from left side. The middle peak carries 7 dB less intensity than the higher peak to afford better detection after executing the cross-correlation trace. The inequality of the shaped peaks made it easier to analyse the cross-correlation measurements and the computed Fourier transform shapes.

In order to check the nonlinear phase shift change in the shaped pulses, the B-integral was first calculated for the square and double-peak pulses presented in Figure 7.15. The intensity profile of the pulses and the related B-integral are shown in Figure 7.15 (a and c) and Figure 7.15 (b and d), respectively. All are displayed in regard to the pulse width. It can be observed that there was no spectral change in time shift for the both pulse profiles even though $B \neq 0$. However, the value of B-integral increases beyond π, which initiates high nonlinearity inside the power amplifier and limits the probability of further power scaling, even if the MOPA could be pumped at higher powers. This effect is more severe in the pulses with narrower width of peak, with respect to the total pulse width, resulting in higher spectral modulation due to the peak power rise. The total B-integral of the system was calculated to be $\sim 1.92\pi$ (0.65π, 0.21π, 0.071π, 0.015π, and 0.972π from coupled fibre, fibre stretcher, 1st pre-amplifier, 2nd pre-amplifier and power amplifier, respectively). The total system B-integral is $\sim$3 times lower than the system presented in chapter 6, due to the lower peak power in this system. It shows how the reduced peak power at the input of the MOPA chain, after the seed coupling patch cord fibre, has improved the laser performance.

7.2.4 Spatial Beam Shaping Results

Figure 7.16 (a) shows the far-field doughnut shaped beam profiles after the conversion of the fundamental Gaussian mode using the S-waveplate at the output of the fibre with power of 51 W and recorded at the focus of an f=200 mm lens using a CCD camera. As expected from a radially polarised beam, after passing through a linear polariser the intensity distribution of the output mode exhibited a symmetric two-lobe structure parallel to the transmission axis of the polariser (shown with white arrows) as illustrated in Figure 7.16 (b-e). Utterly well agreed with measured spatial profiles in 20W average power level exhibited in Figure 7.16 lower line. The far-field beam size ~ 270 μm was measured.

The stability of doughnut-shaped intensity profile can be observed in both situations and its well maintenance by increasing the power level is indicated in Figure 7.17.

7.3 Conclusion

In terms of the temporal pulse shaping, a commercial seed laser source has proven good quality of shapes at different power levels. >50 W could be achieved, tenfold

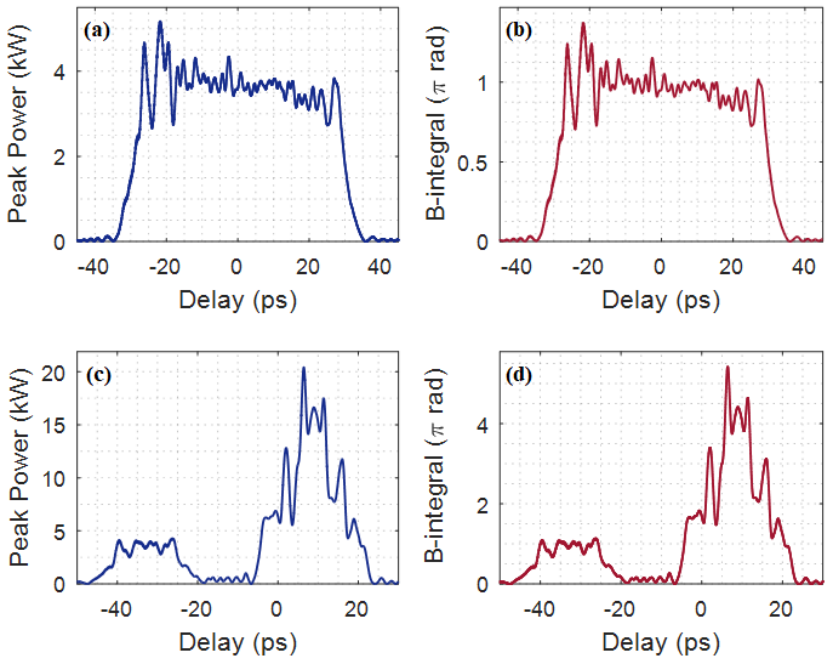

Figure 7.15: Peak power (a and c) and B-integral profiles (b and d) of the square and double peaks shaped pulses at 51 W average power level.

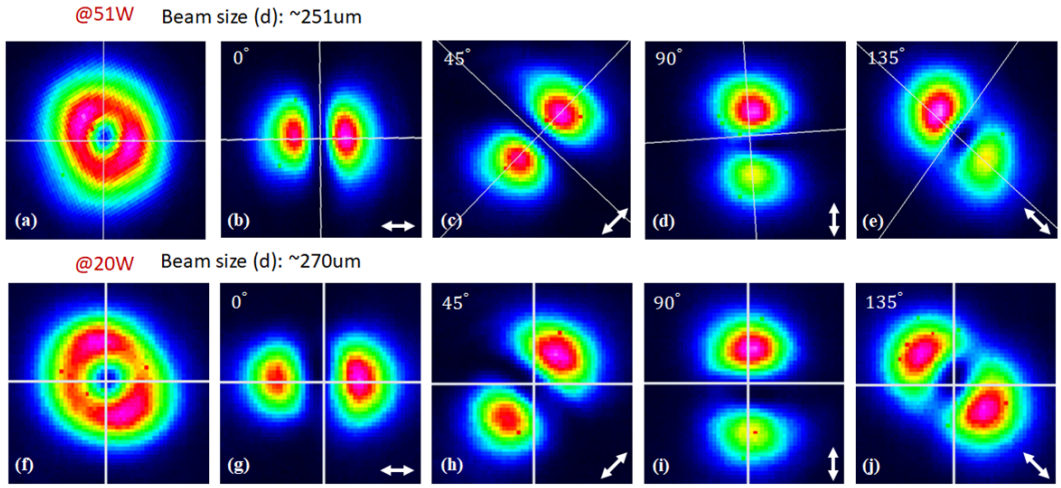

Figure 7.16: Comparison of spatial beam shaping in far field running at 20 W (a-e) and 51 W (f-j) average power levels. Ring shaped beam and its polarisations. White arrows indicate the transmission axis of the polariser.

improvement to that achieved by the mode-locked laser seed detailed in chapter 6. According to the results in Figures 6.25 to 6.26, the mode-locked based laser system shaping for square and single-peak pulses depicted a poor quality at 10 W average power level and practically not suitable for any other type of temporal shaping. The system produced 0.25 μJ pulse energy at 200 MHz repetition rate and 70 ps pulse width.

In conclusion, based on the previous work at [50], we used a similar shaping technique to build a nearly fully-fiberised picosecond MOPA system with higher and

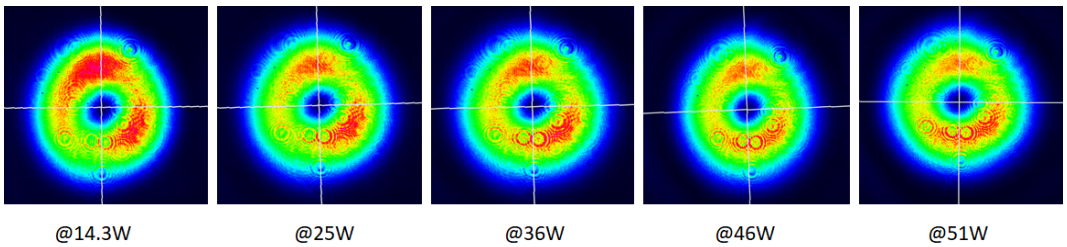

Figure 7.17: Comparison of doughnut-shaped beam profile in terms of average power elevation from left to right.

freely adjustable power. This system compared to the former published results in [50] has several differences and improvements. The mode area and fibre length as well as pulse duration in the final amplifier are all similar and hence, the pulse energy achievable is also similar in both systems. In the previous CPA with offset stretcher/compressor, the pulse duration is ∼10 times longer before the final amplifier whilst the input to the final amplifier was only ∼0.25 W (<10 W peak power) indicating nonlinear effects were confined in the final amplifier only. In the current work, there is non-negligible B-integral in the stretcher fibre and since it is placed prior to the WaveShaper, the pulse profile in the stretcher is invariant for all the subsequently shaped final temporal profiles. Hence, in the current system the total B-integral is both larger as well as a composite of the SPM process accumulated due to the propagation of untruncated Gaussian pulse shape in the stretcher and then truncated shaped pulse profiles in the power amplifier.

We have demonstrated various pulse waveforms in the temporal domain, with picosecond-duration pulses from an Yb-fibre laser system, and combined this with the conversion to a doughnut-shaped beam with radial polarisation in the spatial domain.

This first high power spatio-temporal beam tailored fibre laser system represents a highly flexible, compact architecture that can easily be employed in industrial and relevant systems to improve materials processing methods. We demonstrated significant improvement regarding the earlier published versions.

Chapter 8

Conclusions

A summary of the project work as elucidated in previous chapters of this thesis and the prospect in future work and improvement suggestions are presented here.

8.1 Summary

Two different operating pulse regimes of the fibre MOPA system were constructed and discussed, i.e. the nanosecond regime in chapter 4 and the picosecond regime in chapter 5, 6 and 7.

A directly modulated SLD seeded Yb-doped fibre MOPA system has been built for the temporal and spatial shaping of nanosecond pulses. First of all, we have examined the possibility of using a FBG stabilised SLD function, however it induces significant optical loss of ∼9 dB and some unwanted modulation of pulse in terms of appearance of multiple spikes. Therefore, spectral slicing of the SLD through the use of a 99% reflective FBG was implemented instead, and the power amplifying via a chain of three amplifiers. ASE content was reduced using an AOM and a free-space bandpass filter. Reduction of the length of passive fibres in the system suppress the appearance of SRS at higher energy levels. Temporal pulse shaping was carried out by pre-shaping the seed with direct modulation of the drive current to the SLD. The computer-controlled AWG could be used to compensate pulse distortion due to gain saturation within the MOPA system. Mode shaping was achieved by applying a S-waveplate to convert the generated linearly polarised Gaussian-shaped beam from the third pre-amplifier stage into a doughnut-shaped beam with radial or azimuthal polarisation. The system performance including determination of the minimum pulse width and repetition rate without great pulse distortion were explored before coupling into the last two amplifier stages. This was done in accordance with the desired application of this laser system for materials processing, which requires high-energy high-power sources, generally at low repetition rates.

The nanosecond results successfully proved the proposed idea of the ERM project to demonstrate the capability of spatial and temporal pulse shaping of a SLD seeded MOPA system. Enabling the study of resulting improvements in materials processing control and speed. Step by step analysis of the oscillator and each amplifier stage, allowed improvement in the system performance to a maximum average output power of 22.5 W. Pulse energies as high as ∼860 μJ where achieved in the all fibres MOPA with user-defined nanosecond output pulses with either radially or azimuthally

polarised doughnut-shaped beams. Exhibiting a spatially and temporally flexible laser source with interesting possibilities for applications in a variety of laser materials processing areas. Materials processing trials conducted by the project partner (University of Cambridge) on titanium (Ti), silicon, steel and aluminum samples demonstrated promising results. The system was assembled as a compact laser source and delivered to the project partner for continued studies.

A gain-switched diode seeded MOPA system operating in the picosecond pulse regime was then tested. The amplifier chain used for nanosecond pulse system was again used but with a self-seeding gain-switched source, generating 150 ps pulses at 87.5 MHz repetition rate (for this test). Spatial beam shaping was tried with a *q*-plate rather than the S-waveplate due to its lower insertion loss and resulted in a pulse energy of 25.8 μJ with a peak power of 230 kW in a radially polarised beam at a repetition rate of 1.367 MHz. An SRS peak was however still 40 dB below the signal peak, was observed with power scaling to 35 W average output power, which shows a good possibility for further power scaling. A high average power (100 W) result together with spatial beam shaping for radial and azimuthal polarisations was achieved at repetition rate of 5.468 MHz as published in [150]. The laser system is being used for materials processing trials at the University of Cambridge.

In order to obtain temporal shaping of picosecond pulses we initially showed good quality 5 W temporal pulse shaping implemented using a 1 μm WaveShaper in a MOPA laser system. This system was seeded by a in-house-built self-starting mode-locked laser at a repetition rate of $\sim$ 23 MHz and pulse width of $\sim$ 55 ps. Power scaling was limited by excessive spectral modulation being amplified as the B-integral increased. Finally, picosecond spatio-temporal pulse shaping carried out with a commercial femtosecond ORIGAMI laser seed source, borrowed from NKT, operating at 100 MHz repetition rate and 200 mW power level. The free-space output beam of the laser coupled into PM980 fibre up to 35 mW, leading to a fully-fiberised laser. After a chain of three amplifiers a full set of temporal pulse shapes including square, single, double-and triple-peak, Gaussian and a train of Gaussian peaks pulses were able to be generated at a power level beyond 50W. Achieved at a repetition rate of 200 MHz for 70 ps pulse duration. This is by far the highest optical power demonstrated for an arbitrary temporal-pulse-shaping picosecond fibre laser system to date. Additionally, a well preserved doughnut profile obtained with a S-waveplate after power scaling, resulted in an appropriate final achievement for the EPSRC funded ERM project.

8.2 Prospective Future Research

There is a huge demand and possible market for fiberised laser systems operating with high-pulse-energy especially in materials processing. Industrial perspective requires systems operating with high peak powers, have repetition rates in the GHz range, in the short picosecond pulse regimes, i.e. less than 10 ps. Gain saturation, ASE, nonlinear effects and pump power are the main parameters governing the maximum pulse energy that can be extracted from the fibre amplifier chain. Optimisation of each stage helps to get move closer to this ambition. Although the achievements of this project are not totally satisfying those requirements of temporal pulse shaping at a power level >100W, significant advances were demonstrated in both nanosecond and picosecond pulse regimes.

The generation of spectrally narrow picosecond optical pulses via a gain-switched laser make it as a good source to apply the mode-shaper setup (a SLM based shaper [197–199]) to not only tailor the beam profile, but also the radial and azimuthal polarised modes. Then, the laser system can be performed as a spatio-temporal beam shaping source opportunity to use higher order modes in material ablation and any other interested field.

In the in-house built mode-locked fibre laser system, the performance can be further improved with better selection of chirped FBG. Insertion of a coupler inside the cavity for investigation on the transmission spectral behavior of the CFBG will help to reduce the modulations on the seed spectrum. Moreover, using some other fibres as the stretcher, which suffers from less nonlinear phase shifts through higher input powers will allow to increase the laser output power with less effect of ripple on the spectral profile of desired temporal shaping using such stable mode-locked laser source.

Performance of picosecond all fibre 50 W MOPA with the NKT seed laser in spatial and temporal pulse shaping still leaves room for further power scaling. Ultimately, this high average power level and the capability to build it as a very compact laser system will be made it possible to may replace CPA bulk laser in most applications. Besides that, temporal shaped profile can be further recorded in green via frequency doubling with such laser system. Similar to nanosecond and gain-switched MOPA lasers, the S-waveplate can be placed before power scaling stage to convert Gaussian mode to doughnut-shaped intensity profile through the gain fibre.

These novel temporal shaping outputs at such a high average power attained by just amplitude training technique for the WaveShaper. Hence, running the shaping algorithm for both amplitude and phase might enhance the quality of the resulted temporal shapes, allow to take the advantage of high output power levels of the laser, consequently. Subsequently, progress the laser operation with an appropriated burst-mode and pulse tailoring profiles can be taken into account to not only enable high ablation rates but also surface quality.

List of Publications

[1] **N. Baktash**, D. Lin, D. Xu, S. U. Alam, J. V. Price, and D. J. Richardson, "50W arbitrarily shaped picosecond pulses with a radially polarized output beam from a Yb-doped MOPA,", Submission in Progress.

[2] D. Lin, **N. Baktash**, S. U. Alam, and D. J. Richardson, "106 W, Picosecond Yb- Doped Fiber MOPA System with a Radially Polarized Output Beam," *Optics Letters*, vol. 43, issue 20, pp. 4957-4960, October 2018.

[3] C. J. Stirling, A. L. Donko, **N. Baktash**, K. Grabska, A. L. Camacho Rosales, D. T. Clarke, J. J. Prentice, M. T. Posner, "Student-led Outreach and Public Engagement activities at The University of Southampton to Celebrate The Inaugural International Day of Light," *Optics Education and Outreach V, SPIE Optics+Photonics Conference, San Diego, USA*, 19-23 August 2018.

[4] D. Lin, **N. Baktash**, M. Berendt, M. Beresna, P. G. Kazansky, W. A. Clarkson, S. U. Alam, and D. J. Richardson, "Radially- and Azimuthally- Polarized Nanosecond Yb-Doped Fiber MOPA System Incorporating Temporal Shaping," *Optics Letters*, vol. 42, issue 9, pp. 1740-1743, April 2017.

[5] D. Lin, **N. Baktash**, S. U. Alam, and D. J. Richardson, "High Energy, Radially Polarized Picosecond Laser Pulses From a Yb-Doped Fiber MOPA," *CLEO 17 San Jose, CA*, 14-19 May 2017.

[6] D. Lin, **N. Baktash**, M. Berendt, M. Beresna, P. G. Kazansky, W. A. Clarkson, S. U. Alam, D. J. Richardson, "Radially Polarized Nanosecond Yb-Doped Fiber MOPA System Incorporating Temporal Shaping," *CLEO 16 San Jose, CA*, 5-10 June 2016.

References

[1] A. E. Siegman, *Lasers*. University Science Books Sausalito, California, 1986.

[2] G. L. Goswami and D. Kumar, "Laser materials processing," *Bull. Mater. Sci*, vol. 11, no. 2 & 3, pp. 213–224, 1988.

[3] A. Ghatak and K. Thyagarajan, *Introduction to fiber optics*. Cambridge University Press, USA, 2000.

[4] W. M. Steen; and J. Mazumder, *Laser Material Processing*. Springer, 2010.

[5] C. J. Saraceno, D. Sutter, T. Metzger, and M. Abdou Ahmed, "The amazing progress of high-power ultrafast thin-disk lasers," *Journal of the European Optical Society-Rapid Publications*, vol. 15, no. 1, 2019.

[6] K. Contag, M. Karszewski, C. Stewen, A. Giesen, and H. Hügel, "Theoretical modelling and experimental investigations of the diode-pumped thin-disk Yb:YAG laser," *Quantum Electronics*, vol. 29, no. 8, pp. 697–703, 1999.

[7] A. Giesen and J. Speiser, "Fifteen years of work on thin-disk lasers: results and scaling laws," *IEEE Journal of Selected Topics in Quantum Electronics*, vol. 13, no. 3, pp. 598–609, 2007.

[8] C. J. Saraceno, F. Emaury, C. Schriber, M. Hoffmann, M. Golling, T. Sudmeyer, and U. Keller, "Ultrafast thin-disk laser with 80 μJ pulse energy and 242 W of average power," *Optics Letters*, vol. 39, no. 1, pp. 9–12, 2014.

[9] H. Fattahi, A. Alismail, H. Wang, J. Brons, O. Pronin, T. Buberl, L. Vamos, G. Arisholm, A. M. Azzeer, and F. Krausz, "High-power, 1-ps, all-Yb:YAG thin-disk regenerative amplifier," *Optics Letters*, vol. 41, no. 6, pp. 1126–9, 2016.

[10] T. S. Rutherford, W. M. Tulloch, E. K. Gustafson, and R. L. Byer, "Edge-pumped quasi-three-level slab lasers-design and power scaling," *IEEE Journal of Quantum Electronics*, vol. 36, no. 2, 2000.

[11] Y. Liu, J. Lei, T. Li, N. Li, and X. Tang, "4.55 kW LD end-pumped Nd:YAG surface gain slab laser," *Laser Physics*, vol. 29, no. 1, p. 016101, 2019.

[12] T. Y. Fan, "Laser beam combining for high-power, high-radiance sources," *IEEE Journal of Selected Topics in Quantum Electronics*, vol. 11, no. 3, pp. 567–577, 2005.

[13] F. Chen, J. Ma, C. Wei, R. Zhu, W. Zhou, Q. Yuan, S. Pan, J. Zhang, Y. Wen, and J. Dou, "10 kW-level spectral beam combination of two high power broad-linewidth fiber lasers by means of edge filters," *Optics Express*, vol. 25, no. 26, pp. 32783–32791, 2017.

[14] Z. Liu, X. Jin, R. Su, P. Ma, and P. Zhou, "Development status of high power fiber lasers and their coherent beam combination," *Science China Information Sciences*, vol. 62, no. 4, p. 041301, 2019.

[15] D. J. Richardson, J. Nilsson, and W. A. Clarkson, "High power fiber lasers-current status and future perspectives [invited]," *J. Opt. Soc. Am. B*, vol. 27, no. 11, pp. B63–B92, 2010.

[16] C. Jauregui, J. Limpert, and A. Tünnermann, "High-power fibre lasers," *Nature Photonics*, vol. 7, pp. 861–867, 20 October 2013.

[17] A. Ferin, V. Gapontsev, V. Fomin, A. Abramov, M. Abramov, and D. Mochalov, "17 kW CW laser with 50 μm delivery," in *6th International Symposium on High-Power Fiber Lasers and Their Applications, St. Petersburg, Russia*, pp. 1–11, 28 August 2012.

[18] E. A. Shcherbakov, V. V. Fomin, A. A. Abramov, A. A. Ferin, D. V. Mochalov, and V. P. Gapontsev, "Industrial grade 100 kW power CW fiber laser," in *Advanced Solid-State Lasers Congress, Paris, France*, 27 October–1 November 2013.

[19] V. Fomin, V. Gapontsev, E. Shcherbakov, A. Abramov, A. Ferin, and D. Mochalov, "100 kW CW fiber laser for industrial applications," in *2014 International Conference Laser Optics, St. Petersburg, Russia*, pp. 1–11, 28 August 2014.

[20] R. Paschotta, J. Nilsson, A. C. Tropper, and D. C. Hanna, "Ytterbium-doped fiber amplifiers," *IEEE Journal of Quantum Electronics*, vol. 33, no. 7, pp. 1049–1056, 1997.

[21] J. Dutta Majumdar and I. Manna, "Laser material processing," *International Materials Reviews*, vol. 56, no. 5-6, pp. 341–388, 2011.

[22] M. Kraus, M. A. Ahmed, A. Michalowski, A. Voss, R. Weber, and T. Graf, "Microdrilling in steel using ultrashort pulsed laser beams with radial and azimuthal polarization," *Optics Express*, vol. 18, no. 21, pp. 22305–22313, 2010.

[23] A. Malinowski, P. Gorman, C. A. Codemard, F. Ghiringhelli, A. J. Boyland, A. Marshall, M. N. Zervas, and M. K. Durkin, "High-peak-power, high-energy, high-average-power pulsed fiber laser system with versatile pulse duration and shape," *Optics Letters*, vol. 38, no. 22, pp. 4686–9, 2013.

[24] A. G. Demir, K. Pangovski, W. O'Neill, and B. Previtali, "Laser micromachining of TiN coatings with variable pulse durations and shapes in ns regime," *Surface and Coatings Technology*, vol. 258, pp. 240–248, 2014.

[25] K. Pangovski, M. Sparkes, A. Cockburn, W. O'Neill, P. S. Teh, D. Lin, and D. Richardson, "Control of material transport through pulse shape manipulation- A development toward designer pulses," *IEEE Journal of Selected Topics in Quantum Electronics*, vol. 20, no. 5, pp. 51–63, 2014.

[26] R. Le Harzic, D. Breitling, S. Sommer, C. Föhl, K. König, F. Dausinger, and E. Audouard, "Processing of metals by double pulses with short laser pulses," *Applied Physics A*, vol. 81, no. 6, pp. 1121–1125, 2005.

[27] X. Liu, D. Du, and G. Mourou, "Laser ablation and micromachining with ultrashort laser pulses," *IEEE Journal of Quantum Electronics*, vol. 33, no. 10, pp. 1706–1716, 1997.

[28] K. Pangovski, K. Li, and W. O'Neill, "Application of picosecond lasers for surface modification and polishing," in *Photonics London, London, UK*, July 2011.

[29] P. Zhu, J. Han, H. Xie, and X. Li, "Study of ultrafast laser polishing technology," in *Proceedings of SPIE, The International Conference on Photonics and Optical Engineering, icPOE 2014*, vol. 9449, pp. 944934–1–5, 19 February 2015.

[30] K. Pangovski, M. Sparkes, and W. O'Neill, "A holographic method for optimisation of laser-based production processes," *Advanced Optical Technologies*, vol. 5, no. 2, pp. 177–186, 18 April 2016.

[31] K. T. Vu, A. Malinowski, D. J. Richardson, F. Ghiringhelli, L. M. B. Hickey, and M. N. Zervas, "Adaptive pulse shape control in a diode-seeded nanosecond fiber MOPA system," *Optics Express*, vol. 14, no. 23, pp. 10996–11001, 2006.

[32] K. T. Vu, *High Power Nanosecond Pulsed Fiber LaserAmplifiers.* Thesis, 2008.

[33] D. Lin, S. Alam, K. K. Chen, A. Malinowski, S. Norman, and D. Richardson, "100W- fully-fiberised ytterbium doped master oscillator power amplifier incorporating adaptive pulse shaping," in *CLEO/QELS 2009, Baltimore, MD*, 2-4 June 2009.

[34] A. Malinowski, K. T. Vu, K. K. Chen, J. Nilsson, Y. Jeong, S. Alam, D. Lin, and D. J. Richardson, "High power pulsed fiber MOPA system incorporating electro-optic modulator based adaptive pulse shaping," *Optics Express*, vol. 17, no. 23, 2009.

[35] W. O'Neill and L. Kun, "High-quality micromachining of silicon at 1064 nm using a high-brightness MOPA-based 20-W Yb fiber laser," *IEEE Journal of Selected Topics in Quantum Electronics*, vol. 15, no. 2, pp. 462–470, 2009.

[36] A. G. Demir, K. Pangovski, W. O'Neill, and B. Previtali, "Investigation of pulse shape characteristics on the laser ablation dynamics of TiN coatings in the ns regime," *Journal of Physics D: Applied Physics*, vol. 48, no. 23, pp. 235202–1–11, 2015.

[37] X. D. Wang, X. Yuan, S. L. Wang, J. S. Liu, A. Michalowski, and F. Dausinger, *Efficient laser drilling with double-pulse laser processing.* New Manufacturing Techniques and their Role in Improving Enterprise Performance, Springer-Verlag London Limited, 2008.

[38] X. D. Wang, A. Michalowski, D. Walter, S. Sommer, M. Kraus, J. S. Liu, and F. Dausinger, "Laser drilling of stainless steel with nanosecond double-pulse," *Optics & Laser Technology*, vol. 41, no. 2, pp. 148–153, 2009.

[39] C. Emmelmann and J. P. C. Urbina, "Analysis of the influence of burst-mode laser ablation by modern quality tools," in *Lasers in Manufacturing 2011, LiM 2011, Munich, Germany*, vol. 12, Part B, pp. 172–181, 23-26 May 2011.

[40] K. Pangovski, M. Sparkes, and W. O'Neill, "A new way to diagnose and optimise laser-material processing operations," *The Laser User*, vol. 77, pp. 26–27, 2015.

[41] A. H. Hamad, *Effects of Different Laser Pulse Regimes (Nanosecond, Picosecond and Femtosecond) on the Ablation of Materials for Production of Nanoparticles in Liquid Solution, Chapter 12*, pp. 305–326. InTech, 7 September 2016.

[42] J. Hernandez-Rueda, J. Siegel, M. Galvan-Sosa, A. Ruiz de la Cruz, and J. Solis, "Surface structuring of fused silica with asymmetric femtosecond laser pulse bursts," *Journal of the Optical Society of America B*, vol. 30, no. 5, pp. 1352–1356, 2013.

[43] C. Kerse, H. Kalaycioğlu, P. Elahi, B. Çetin, D. K. Kesim, Ö. Akçaalan, S. Yavaş, M. D. Aşik, B. Öktem, H. Hoogland, R. Holzwarth, and F. Ö. Ilday, "Ablation-cooled material removal with ultrafast bursts of pulses," *Nature*, vol. 537, no. 7618, pp. 84–88, 2016.

[44] A. Žemaitis, P. Gečys, M. Barkauskas, G. Račiukaitis, and M. Gedvilas, "Highly-efficient laser ablation of copper by bursts of ultrashort tuneable (fs-ps) pulses," *Scientific Reports*, vol. 9, no. 1, pp. 12280–1–8, 22 August 2019.

[45] P. Petropoulos, M. Ibsen, A. D. Ellis, and D. J. Richardson, "Rectangular pulse generation based on pulse reshaping using a superstructured fiber Bragg grating," *Journal of Lightwave Technology*, vol. 19, no. 5, pp. 746–752, 2001.

[46] J. Azaña, L. K. Oxenløwe, E. Palushani, R. Slavík, M. Galili, H. C. H. Mulvad, H. Hu, Y. Park, A. T. Clausen, and P. Jeppesen, "In-fiber subpicosecond pulse shaping for nonlinear optical telecommunication data processing at 640 Gbit/s," *International Journal of Optics*, vol. 2012, pp. 1–16, 2012.

[47] Y. Park, M. H. Asghari, T. J. Ahn, and J. Azaña, "Transform-limited picosecond pulse shaping based on temporal coherence synthesization," *Optics Express*, vol. 15, no. 15, pp. 9584–9599, 2007.

[48] A. M. Weiner and J. P. Heritage, "Picosecond and femtosecond Fourier pulse shape synthesis," *Revue de Physique Appliquée*, vol. 22, no. 12, pp. 1619–1628, 1987.

[49] A. M. Weiner, "Ultrafast optical pulse shaping: A tutorial review," *Optics Communications*, vol. 284, no. 15, pp. 3669–3692, 2011.

[50] B. M. Zhang, Y. Feng, D. Lin, J. H. V. Price, J. Nilsson, S. Alam, P. P. Shum, D. N. Payne, and D. J. Richardson, "Demonstration of arbitrary temporal shaping of picosecond pulses in a radially polarized Yb-fiber MOPA with $>$ 10 W average power," *Optics Express*, vol. 25, no. 13, pp. 15402–15413, 2017.

[51] V. G. Niziev and A. V. Nesterov, "Influence of beam polarization on laser cutting efficiency," *Journal of Physics D: Applied Physics*, vol. 32, pp. 1455–1461, 1999.

[52] M. Meier, V. Romano, and T. Feurer, "Material processing with pulsed radially and azimuthally polarized laser radiation," *Applied Physics A*, vol. 86, no. 3, pp. 329–334, 2006.

[53] R. Weber, A. Michalowski, M. Abdou-Ahmed, V. Onuseit, V. Rominger, M. Kraus, and T. Graf, "Effects of radial and tangential polarization in laser material processing," in *Lasers in Manufacturing 2011, LiM 2011, Munich, Germany*, vol. 12, Part A, pp. 21–30, 23-26 May 2011.

[54] A. Tünnermann, S. Nolte, and J. Limpert, "Femtosecond vs. picosecond laser material processing," *Laser Technik Journal*, vol. 7, no. 1, pp. 34–38, 2010.

[55] S. Dondieu, K. L. Wlodarczyk, P. Harrison, A. Rosowski, J. Gabzdyl, R. L. Reuben, and D. P. Hand, "High average power pulsed fibre lasers for high-quality engraving," in *6th UK Industrial Laser Applications Symposium 2019, ILAS 2019, Crewe Hall, Crewe, United Kingdom*, 20-21 March 2019.

[56] L. Li, J. Lawrence, and J. T. Spencer, "Materials processing with a high power diode laser," in *ICALEO 1996, Detroit, Michigan, USA*, vol. 1996, Journal of Laser Applications, 14-17 October 1996.

[57] J. Powell, *CO2 Laser Cutting*. Springer, 1998.

[58] W. Koechner, *Solid-State Laser Engineering*, vol. 1. Springer-Verlag New York, 2006.

[59] A. F. Lasagni, T. Roch, M. Bieda, and D. Langheinrich, "Direct fabrication of periodic structures on surfaces," *Laser Technik Journal, Wiley-VCH Verlag GmbH & Co. KGaA, Weinheim*, vol. 1, no. 3, pp. 45–48, 2011.

[60] G. C. Rodrigues, V. Vorkov, and J. R. Duflou, "Optimal laser beam configurations for laser cutting of metal sheets," in *10th CIRP Conference on Photonic Technologies, LANE 2018, Fürth, Germany*, vol. 74, pp. 714–718, 3-6 September 2018.

[61] M. Köhler, T. Tóth, A. Kreybohm, J. Hensel, and K. Dilger, "Effects of reduced ambient pressure and beam oscillation on gap bridging ability during solid-state laser beam welding," *Journal of Manufacturing and Materials Processing*, vol. 4, no. 40, pp. 1–13, 29 April 2020.

[62] D. Lin, *Doughnut-shaped beam generation in solid-state and fibre lasers*. Thesis, 2015.

[63] J. Mende, E. Schmid, J. Speiser, G. Spindler, and A. Giesen, "Thin disk laser: power scaling to the kW regime in fundamental mode operation," in *Proceeding of SPIE, Solid State Lasers XVIII: Technology and Devices*, vol. 7193, pp. 71931V–1–12, 27 February 2009.

[64] V. Rominger, M. Koitzsch, V. Kuhn, T. Gottwald, C. Stolzenburg, M. Holzer, S.-S. Schad, A. Killi, and T. Ryb, "Latest trends in high power disk laser technology," in *Lasers in Manufacturing 2015, LiM 2015, Munich, Germany*, pp. 1–6, 22-25 June 2015.

[65] G. C. Rodrigues, H. Vanhove, and J. R. Duflou, "Direct diode lasers for industrial laser cutting: a performance comparison with conventional fiber and CO2 technologies," in *8th CIRP Conference on Photonic Technologies, LANE 2014, Fürth, Germany*, vol. 56, pp. 901–908, 8-11 September 2014.

[66] K. Hirano and R. Fabbro, "A comparative experimental study of laser fusion cutting of steel with 1 μm and 10 μm laser wavelengths," in *ICALEO 2013, Miami, Florida, USA*, vol. 2013, pp. 119–124, 6-10 October 2013.

[67] W. Rath, "CO2 lasers: modern workhorses in the world of industrial manufacturing," *Laser Technik Journal, Wiley-VCH Verlag GmbH & Co. KGaA, Weinheim*, vol. 4, no. 3, pp. 34–39, 2007.

[68] F. O. Olsen and L. Alting, "Pulsed laser materials processing, ND-YAG versus CO2 lasers," in *CIRP Annals- Manufacturing Technology*, vol. 44, no.1, pp. 141–145, December 1995.

[69] K. Nowak, T. Ohta, T. Suganuma, J. Fujimoto, H. Mizoguchi, A. Sumitani, and A. Endo, "CO2 laser drives extreme ultraviolet nano-lithography - Second life of mature laser technology," *Opto-Electronics Review*, vol. 21, no. 4, pp. 52–61, December 2013.

[70] A. P. Mineev, S. M. Nefedov, P. P. Pashinin, P. A. Goncharov, and V. V. Kiselev, "Radio frequency excited planar CO2 and CO lasers," in *International Conference on Lasers, Applications, and Technologies, LAT 2010, Kazan, Russian*, vol. 7994, pp. 799402–1–10, September 2010.

[71] B. Köhler, A. Segref, P. Wolf, A. Unger, H. Kissel, and J. Biesenbach, "Multi-kW high-brightness fiber coupled diode laser," in *Proceedings of SPIE - High-Power Diode Laser Technology and Applications XI*, vol. 8605, pp. 86050B–1–8, 22 February 2013.

[72] R. K. Huang, B. Samson, B. Chann, B. Lochman, and P. Tayebati, "Recent progress on high-brightness kW-class direct diode lasers," in *2015 IEEE High Power Diode Lasers and Systems Conference (HPD), Coventry, UK*, vol. 8605, no. 86050B, pp. 29–30, 14-15 October 2015.

[73] M. Baumann, A. Balck, J. Malchus, R. V. Chacko, S. Marfels, U. Witte, D. Dinakaran, S. Ocylok, M. Weinbach, C. Bachert, A. Kösters, V. Krause, H. König, A. Lell, B. Stojetz, M. Ali, and U. Strauss, "1000 W blue fiber-coupled diode-laser emitting at 450 nm," in *Proceeding of SPIE, High-Power Diode Laser Technology XVII*, vol. 10900, pp. 1090005–1–12, 4 March 2019.

[74] S. Britten and V. Krause, "Industrial blue diode laser breaks 1 kW barrier," *Wiley Online Library, Photonics Views*, vol. 16, no.2, pp. 30–33, 12 March 2019.

[75] J. Lei, X. Yang, Y. Liu, B. Li, T. Li, and X. Tang, "Study on double end-pumped high power slab laser with laser diode arrays," in *AOPC 2017: Laser Components, Systems, and Applications, Beijing, China*, vol. 10457, no. 104571F, 24 October 2017.

[76] E. Beyer, A. Mahrle, M. Lütke, J. Standfuss, and F. Brückner, "Innovation in high power fiber laser applications," in *Proceedings of SPIE - Fiber Lasers IX: Technology, Systems, and Applications*, vol. 8237, pp. 823717–1–11, 16 February 2012.

[77] J.-P. Negel, A. Loescher, A. Voss, D. Bauer, D. Sutter, A. Killi, M. A. Ahmed, and T. Graf, "Ultrafast thin-disk multipass laser amplifier delivering 1.4 kW (4.7 mJ, 1030 nm) average power converted to 820 W at 515 nm and 234 W at 343 nm," *Optics Express*, vol. 23, no. 16, pp. 21064–21077, 10 August 2015.

[78] T. Nubbemeyer, M. Kaumanns, M. Ueffing, M. Gorjan, A. Alismail, H. Fattahi, J. Brons, O. Pronin, H. G. Barros, Z. Major, T. Metzger, D. Sutter, and F. Krausz, "1 kW, 200 mJ picosecond thin-disk laser system," *Optics Letters*, vol. 42, no. 7, pp. 1381–1384, 2017.

[79] A. Giesen, H. Hüge, A. Voss, K. Wittig, U. Brauch, and H. Opower, "Scalable concept for diode-pumped high-power solid-state lasers," *Applied Physics B*, vol. 58, pp. 365–372, 1994.

[80] P. S. Teh, *High performance pulsed fiber laser systems for scientific & industrial applications*. Thesis, 2015.

[81] J. Bovatsek and R. Patel, "Ultrashort pulse laser technology for processing of advanced electronics materials," in *18th International Symposium on Laser Precision Microfabrication, LPM 2017, Toyama, Japan*, 5-8 June 2017.

[82] K. Pangovski, O. B. Otanocha, S. Zhong, M. Sparkes, Z. Liu, W. O'Neill, and L. Li, "Investigation of plume dynamics during picosecond laser ablation of H13 steel using high-speed digital holography," *Applied Physics A*, vol. 123, pp. 114–1–6, 9 January 2017.

[83] K. Pangovski, P. S. Teh, D. Lin, S. Alam, D. J. Richardson, and W. O'Neill, "Pulse energy packing effects on material transport during laser processing of $< 1|1|1 >$ silicon," *Applied Physics A*, vol. 124, pp. 5–1–9, 2018.

[84] M. Müller, C. Aleshire, A. Klenke, E. Haddad, F. Légaré, A. Tünnermann, and J. Limpert, "10.4 kW coherently combined ultrafast fiber laser," *Optics Letters*, vol. 45, no. 11, pp. 3083–3086, 1 June 2020.

[85] M. Lenzner, F. Krausz, J. Krüger, and W. Kautek, "Photoablation with sub-10 fs laser pulses," *Applied Surface Science*, vol. 154-155, pp. 11–16, 1 February 2000.

[86] M. MacKenzie, H. Chi, M. Varma, P. Pal, A. Kar, and L. Paterson, "Femtosecond laser fabrication of silver nanostructures on glass for surface enhanced Raman spectroscopy," *Scientific Reports*, vol. 9, no. 1, no. 1, pp. 17058–1–13, 2019.

[87] P. Elahi, Ö. Akcaalan, C. Ertek, K. Eken, F. Ö. Ilday, and H. Kalaycioğlu, "High-power Yb-based all-fiber laser delivering 300 fs pulses for high-speed ablation-cooled material removal," *Optics Letters*, vol. 43, no. 3, pp. 535–538, 2018.

[88] M. Malinauskas, A. Žukauskas, S. Hasegawa, Y. Hayasaki, V. Mizeikis, R. Buividas, and S. Juodkazis, "Ultrafast laser processing of materials: from science to industry," *Light: Science & Applications*, vol. 5, no. 8, pp. e16133–1–14, 12 August 2016.

[89] S. Loganathan, S. Santhanakrishnan, R. Bathe, and M. Arunachalam, "Surface processing: an elegant way to enhance the femtosecond laser ablation rate and ablation efficiency on human teeth," *Wiley Online Library, Lasers in Surgery and Medicine*, vol. 51, no.9, pp. 797–807, 5 June 2019.

[90] P. S. Teh, S.-u. Alam, R. J. Lewis, and D. J. Richardson, "Single polarization picosecond fiber MOPA power scaled to beyond 500 W," *Laser Physics Letters*, vol. 11, no. 8, pp. 085103–1–5, 2014.

[91] K. L. Wlodarczyk, R. Carter, A. Jahanbakhsh, D. P. Hand, R. R. J. Maier, and M. M. Maroto-Valer, "Fabrication of three-dimensional micro-structures in glass by picosecond laser micro-machining and welding," in *18th International Symposium on Laser Precision Microfabrication, LPM 2017, Toyama, Japan*, 5-8 June 2017.

[92] K. L. Wlodarczyk, R. M. Carter, A. Jahanbakhsh, A. A. Lopes, M. D. Mackenzie, R. R. J. Maier, D. P. Hand, and M. M. Maroto-Valer, "Rapid laser manufacturing of microfluidic devices from glass substrates," *Micromachines*, vol. 9, pp. 409–1–14, August 2018.

[93] K. L. Wlodarczyk, R. Carter, O. Shahrokhi, R. Nhunduru, A. Jahanbakhsh, D. P. Hand, and M. M. Maroto-Valer, "Ultrafast laser manufacturing of glass microfluidic devices," in *Lasers in Manufacturing 2019, LiM 2019, Munich, Germany*, 24-27 June 2019.

[94] D. P. Hand, R. M. Carter, J. Chen, M. Troughton, I. Elder, R. Lamb, R. Thomson, and D. M. J. Esser, "Picosecond laser welding of optical to structural materials," in *9th International Conference on Photonic Technologies, LANE 2016, Fürth, Germany*, vol. 83, 19-22 September 2016.

[95] D. P. Hand, R. M. Carter, R. R. Thomson, M. J. D. Esser, M. Troughton, I. Elder, and R. Lamb, "Ultrafast laser microwelding of optical materials," in *CLEO 2018, San Jose, California, USA*, 13-18 May 2018.

[96] R. Carter, P. Morawska, D. Polyzos, S. Hann, M. J. D. Esser, and D. P. Hand, "Towards industrial application of ultrafast laser microwelding," in *19th International Symposium on Laser Precision Microfabrication, LPM 2018, Edinburgh, United Kingdom*, 25-28 June 2018.

[97] R. Carter, P. Morawska, S. Hann, M. J. D. Esser, and D. P. Hand, "High yield direct fusion welding of glass and metal," in *Lasers in Manufacturing 2019, LiM 2019, Munich, Germany*, 24-27 June 2019.

[98] A. H. Hamad, K. S. Khashan, and A. A. Hadi, *Laser Ablation in Different Environments and Generation of Nanoparticles, Chapter 8*, pp. 177–196. InTech, 21 December 2016.

[99] A. Žemaitis, M. Gaidys, M. Brikas, P. Gečys, G. Račiukaitis, and M. Gedvilas, "Advanced laser scanning for highly efficient ablation and ultrafast surface structuring: experiment and model," *Scientific Reports*, vol. 8, pp. 17376–1–14, 26 November 2018.

[100] N. Maharjan, W. Zhou, Y. Zhou, Y. Guan, and N. Wu, "Comparative study of laser surface hardening of 50CrMo4 steel using continuous-wave laser and pulsed lasers with ms, ns, ps and fs pulse duration," *Surface and Coatings Technology*, vol. 366, pp. 311–320, 2019.

[101] P. Oliveira, S. Addis, J. Gay, K. Ertel, M. Galimberti, and I. Musgrave, "Control of temporal shape of nanosecond long lasers using feedback loops," *Optics Express*, vol. 27, no. 5, pp. 6607–6617, 2019.

[102] C. J. Koester and E. Snitzer, "Amplification in a fiber laser," *Applied Optics*, vol. 3, no. 10, pp. 1182–1186, 1964.

[103] H. M. Pask, R. J. Carman, D. C. Hanna, A. C. Tropper, C. J. Mackechnie, P. R. Barber, and J. M. Dawes, "Ytterbium-doped silica fiber lasers: versatile sources for the 1-1.2 μm region," *IEEE Journal of Selected Topics in Quantum Electronics*, vol. 1, no. 1, pp. 2–13, 1995.

[104] D. Lin, S. U. Alam, A. Malinowski, K. K. Chen, J. R. Hayes, J. C. Flannagan, V. Geddes, J. Nilsson, S. Ingram, S. Norman, and D. J. Richardson, "Temporally and spatially shaped fully-fiberized ytterbium-doped pulsed MOPA," *Laser Physics Letters*, vol. 8, no. 10, pp. 747–753, 2011.

[105] S. T. Hendow and S. A. Shakir, "Structuring materials with nanosecond laser," *Optics Express*, vol. 18, no. 10, pp. 10188–10199, 2010.

[106] G. P. Agrawal, *Nonlinear Fiber Optics*. San Diego, California: Academic Press, 2001.

[107] R. H. Stolen and C. Lee, "Self-phase-modulation in silica optical fibers," *Physical Review A*, vol. 17, no. 4, pp. 1448–1453, 1978.

[108] D. N. Schimpf, E. Seise, T. Eidam, J. Limpert, and A. Tünnermann, "Control of the optical kerr effect in chirped-pulse-amplification systems using model-based phase shaping," *Optics Letters*, vol. 34, no. 24, pp. 3788–3790, 2009.

[109] R. H. Stolen, C. Lee, and R. K. Jain, "Development of the stimulated Raman spectrum in single-mode silica fibers," *Journal of the Optical Society of America B*, vol. 1, no. 4, pp. 652–657, 1984.

[110] M. Kelly, "Controlling SBS in measurements of long optical fiber paths," *Application Note -Agilent Technologies*, pp. 1–6, 2003.

[111] D. N. Schimpf, C. Ruchert, D. Nodop, J. Limpert, A. Tünnermann, and F. Salin, "Compensation of pulse-distortion in saturated laser amplifiers," *Optics Express*, vol. 16, no. 22, pp. 17637–17646, 2008.

[112] L. M. Frantz and J. S. Nodvik, "Theory of pulse propagation in a laser amplifier," *Journal of Applied Physics*, vol. 34, no. 8, pp. 2346–2349, 1963.

[113] "Finisar white paper: Waveshaper basics," 2012. `http://www.finisar.com/optical-instrumentation`.

[114] "Finisar white paper: Waveshaper short pulse shaping," 2013. `http://www.finisar.com/optical-instrumentation`.

[115] V. Yanovsky, Y. Pang, F. Wise, and B. I. Minkov, "Generation of 25-fs pulses from a self-mode-locked Cr:forsterite laser with optimized group-delay dispersion," *Optics Letters*, vol. 18, no. 18, pp. 1541–1543, 1993.

[116] V. Torres-Company, D. E. Leaird, and A. M. Weiner, "Dispersion requirements in coherent frequency-to-time mapping," *Optics Express*, vol. 19, no. 24, pp. 24718–24729, 2011.

[117] J. Azaña and M. A. Muriel, "Real-time optical spectrum analysis based on the time-space duality in chirped fiber gratings," *IEEE Journal of Quantum Electronics*, vol. 36, no. 5, pp. 517–526, 2000.

[118] V. Wong and I. A. Walmsley, "Analysis of ultrashort pulse-shape measurement using linear interferometers," *Optics Letters*, vol. 19, no. 4, pp. 287–289, 1994.

[119] I. A. Walmsley and V. Wong, "Characterization of the electric field of ultrashort optical pulses," *J. Opt. Soc. Am. B*, vol. 13, no. 11, pp. 2453–2463, 1996.

[120] Y. Jeong, J. K. Sahu, D. N. Payne, and J. Nilsson, "Ytterbium-doped large-core fiber laser with 1.36 kW continuous-wave output power," *Optics Express*, vol. 12, no. 25, pp. 6088–6092, 2004.

[121] P. S. Salter and M. J. Booth, "Adaptive optics in laser processing," *Light: Science & Applications*, vol. 8:110, pp. 1–16, 2019.

[122] J. Bures, *Guided Optics: Optical Fibers and All-fiber Components*. Wiley-VCH Verlag GmbH & Co, 2009.

[123] D. Lin, N. Baktash, M. Berendt, M. Beresna, P. G. Kazansky, W. A. Clarkson, S. U. Alam, and D. J. Richardson, "Radially polarized nanosecond Yb-doped fiber MOPA system incorporating temporal shaping," in *CLEO 2016, San Jose, California, USA*, 5-10 June 2016.

[124] D. Lin, J. M. Daniel, M. Gecevičius, M. Beresna, P. G. Kazansky, and W. A. Clarkson, "Cladding-pumped ytterbium-doped fiber laser with radially polarized output," *Optics Letters*, vol. 39, no. 18, pp. 5359–61, 2014.

[125] D. Lin and W. A. Clarkson, "Cladding-pumped Yb-doped fiber laser with vortex output beam," in *CLEO 2015, San Jose, California, USA*, 5-10 June 2015.

[126] S. K. G. Lazarev, A. Hermerschmidt and S. Osten, *Optical Imaging and Metrology: Advanced Technologies, Chapter 1: LCOS Spatial Light Modulators: Trends and Applications*, vol. First Edition. Wiley-VCH Verlag GmbH & Co. KGaA, 2012.

[127] *Phase spatial light modulator LCOS-SLM*. HAMAMATSU.

[128] M. Stalder and M. Schadt, "Linearly polarized light with axial symmetry generated by liquid-crystal polarization converters," *Optics Letters*, vol. 21, no. 23, pp. 1948–1950, 1996.

[129] L. Marrucci, C. Manzo, and D. Paparo, "Optical spin-to-orbital angular momentum conversion in inhomogeneous anisotropic media," *Physical Review Letters*, vol. 96, no. 16, p. 163905, 2006.

[130] L. Marrucci, "The q-plate and its future," *Journal of Nanophotonics*, vol. 7, pp. 078598–1–4, 2013.

[131] G. Machavariani, Y. Lumer, I. Moshe, A. Meir, and S. Jackel, "Efficient extracavity generation of radially and azimuthally polarized beams," *Optics Letters*, vol. 32, no. 11, pp. 1468–1470, 2007.

[132] M. Beresna, M. Gecevičius, and P. G. Kazansky, "Ultrafast laser direct writing and nanostructuring in transparent materials," *Advances in Optics and Photonics*, vol. 6, no. 3, p. 293, 2014.

[133] M. Sakakura, Y. Lei, L. Wang, Y. H. Yu, and P. G. Kazansky, "Ultralow-loss geometric phase and polarization shaping by ultrafast laser writing in silica glass," *Light: Science & Applications*, vol. 9, no. 15, pp. 1–10, 2020.

[134] G. Machavariani, N. Davidson, E. Hasman, S. Blit, A. A. Ishaaya, and A. A. Friesem, "Efficient conversion of a Gaussian beam to a high purity helical beam," *Optics Communications*, vol. 209, pp. 265–271, 2002.

[135] S. Quabis, R. Dorn, and G. Leuchs, "Generation of a radially polarized doughnut mode of high quality," *Applied Physics B*, vol. 81, no. 5, pp. 597–600, 2005.

[136] M. Beresna, M. Gecevičius, and P. G. Kazansky, "Polarization sensitive elements fabricated by femtosecond laser nanostructuring of glass [invited]," *Optical Materials Express*, vol. 1, no. 4, pp. 783–795, 2011.

[137] M. Beresna, *Polarization engineering with ultrafast laser writing in transparent media*. Thesis, 2012.

[138] L. Vertchenko, E. Shkondin, R. Malureanu, and C. Monken, "Laguerre-Gauss beam generation in IR and UV by subwavelength surface-relief gratings," *Optics Express*, vol. 25, no. 6, pp. 5917–5926, 2017.

[139] D. Lin, N. Baktash, M. Berendt, M. Beresna, P. G. Kazansky, W. A. Clarkson, S. U. Alam, and D. J. Richardson, "Radially and azimuthally polarized nanosecond Yb-doped fiber MOPA system incorporating temporal shaping," *Optics Letters*, vol. 42, no. 9, pp. 1740–1743, 2017.

[140] Q. Zhan, "Cylindrical vector beams: from mathematical concepts to applications," *Advances in Optics and Photonics*, vol. 1, no. 1, pp. 1–57, 2009.

[141] T. Kuga, Y. Torii, N. Shiokawa, T. Hirano, Y. Shimizu, and H. Sasada, "Novel optical trap of atoms with a doughnut beam," *Physical Review letters*, vol. 78, no. 25, 1997.

[142] A. Ashkin, "History of optical trapping and manipulation of small-neutral particle, atoms, and molecules," *IEEE Journal of Quantum Electronics*, vol. 6, no. 6, pp. 841–856, 2000.

[143] M. Gua and D. Morrish, "Three-dimensional trapping of Mie metallic particles by the use of obstructed laser beams," *Journal of Applied Physics*, vol. 91, no. 3, pp. 1606–1612, 2002.

[144] Q. Zhan, "Trapping metallic rayleigh particles with radial polarization," *Optics Express*, vol. 12, no. 15, pp. 3377–3382, 2004.

[145] L. Novotny, M. R. Beversluis, K. S. Youngworth, and T. G. Brown, "Longitudinal field modes probed by single molecules," *Phys Rev Lett*, vol. 86, no. 23, pp. 5251–5254, 2001.

[146] M. A. Ahmed, J. Schulz, A. Voss, O. Parriaux, J.-C. Pommier, and T. Graf, "Radially polarized 3 kW beam from a CO_2 laser with an intracavity resonant grating mirror," *Optics Letters*, vol. 32, no. 13, pp. 1824–1826, 2007.

[147] I. Moshe, S. Jackel, A. Meir, Y. Lumer, and E. Leibush, "2 kW, M^2<10 radially polarized beams from aberration-compensated rod-based Nd:YAG lasers," *Optics Letters*, vol. 32, no. 1, pp. 47–49, 2007.

[148] A. Loescher, J. P. Negel, T. Graf, and M. Abdou Ahmed, "Radially polarized emission with 635 W of average power and 2.1 mJ of pulse energy generated by an ultrafast thin-disk multipass amplifier," *Optics Letters*, vol. 40, no. 24, pp. 5758–61, 2015.

[149] S. Piehler, X. Delen, M. Rumpel, J. Didierjean, N. Aubry, T. Graf, F. Balembois, P. Georges, and M. A. Ahmed, "Amplification of cylindrically polarized laser beams in single crystal fiber amplifiers," *Optics Express*, vol. 21, no. 9, pp. 11376–13381, 2013.

[150] D. Lin, N. Baktash, S. U. Alam, and D. J. Richardson, "106 W, picosecond Yb-doped fiber MOPA system with a radially polarized output beam," *Optics Letters*, vol. 43, no. 20, pp. 4957–4960, 2018.

[151] H. Ito, H. Yokoyama, S. Murata, and H. Inaba, "Picosecond optical pulse generation from an r.f. modulated AlGaAs d.h. diode laser," *Electronics Letters*, vol. 15, no. 23, pp. 738–740, 1979.

[152] K. Y. Lau, "Gain switching of semiconductor injection lasers," *Applied Physics Letters*, vol. 52, no. 4, pp. 257–259, 1988.

[153] K. T. Vu, A. Malinowski, M. A. F. Roelens, and D. J. Richardson, "Detailed comparison of injection-seeded and self-seeded performance of a 1060-nm gain-switched Fabry-Pérot laser diode," *IEEE Journal of Quantum Electronics*, vol. 44, no. 7, pp. 645–651, 2008.

[154] K. T. Vu, A. Malinowski, M. A. F. Roelens, M. Ibsen, and D. J. Richardson, "Detailed comparison of injection-seeded and self-seeded performance of a gain-switched laser diode," in *CLEO/QELS 2007, Baltimore, USA*, 6-11 May.

[155] P. S. Teh, S. Alam, D. P. Shepherd, and D. J. Richardson, "Generation of mode-locked optical pulses at 1035 nm from a fiber Bragg grating stabilized semiconductor laser diode," *Optics Express*, vol. 22, no. 11, pp. 13366–73, 2014.

[156] J. S. Feehan, J. H. V. Price, T. J. Butcher, W. S. Brocklesby, J. G. Frey, and D. J. Richardson, "Efficient high-harmonic generation from a stable and compact ultrafast Yb-fiber laser producing 100 μJ, 350 fs pulses based on bendable photonic crystal fiber," *Applied Physics B*, vol. 123, no. 43, pp. 1–12, 2017.

[157] H. A. Haus, "Mode-locking of lasers," *IEEE Journal of Quantum Electronics*, vol. 6, no. 6, pp. 1173–1185, 2000.

[158] R. Paschotta and U. Keller, "Passive mode locking with slow saturable absorbers," *Applied Physics B: Lasers and Optics*, vol. 73, no. 7, pp. 653–662, 2001.

[159] A. Schlatter, S. C. Zeller, R. Grange, R. Paschotta, and U. Keller, "Pulse-energy dynamics of passively mode-locked solid-state lasers above the Q-switching threshold," *J. Opt. Soc. Am. B*, vol. 21, no. 8, pp. 1469–1478, 2004.

[160] R. Paschotta and U. Keller, *Passively mode-locked solid-state lasers.* Chapter 7 in Solid-State Lasers and Applications (ed. A. Sennaroglu), CRC Press, Boca Raton, FL, 2007.

[161] J. Liu, J. M. Yang, W. W. Wang, L. H. Zheng, L. B. Su, and J. Xu, "Passive picosecond and femtosecond mode-locking laser action of Yb3+:LuYSiO5," *Laser Physics*, vol. 21, no. 4, pp. 659–662, 2011.

[162] Z. Wei, B. Zhou, Y. Zhang, Y. Zou, X. Zhong, C. Xu, and Z. Zhang, *All Solid-State Passively Mode-Locked Ultrafast Lasers Based on Nd, Yb, and Cr Doped Media*, book 3, pp. 73–114. InTech, 2012.

[163] P. Grelu and N. Akhmediev, "Dissipative solitons for mode-locked lasers," *Nature Photonics*, vol. 6, no. 2, pp. 84–92, 2012.

[164] R. I. Woodward, "Dispersion engineering of mode-locked fibre lasers," *Journal of Optics*, vol. 20, no. 3, p. 033002, 2018.

[165] K. Jiang, C. Ouyang, P. P. Shum, K. Wu, and J. H. Wong, "High-energy dissipative soliton with MHz repetition rate from an all-fiber passively mode-locked laser," *Optics Communications*, vol. 285, no. 9, pp. 2422–2425, 2012.

[166] N. Davoudzadeh, G. Ducourthial, and B. Q. Spring, "Custom fabrication and modelocked operation of a femtosecond fber laser for multiphoton microscopy," *Scientific Reports*, vol. 9, no. 1, pp. 4233–1–12, 12 March 2019.

[167] K. Zhang, N. Davoudzadeh, G. Ducourthial, and B. Q. Spring, "Low-cost custom fabrication and mode-locked operation of an all-normal-dispersion femtosecond fiber laser for multiphoton microscopy," *Journal of Visualized Experiments (JoVE), Engineering*, vol. 153, no. e60160, 22 November 2019.

[168] R. Huber, M. Wojtkowski, and J. G. Fujimoto, "Fourier Domain Mode Locking (FDML): a new laser operating regime and applications for optical coherence tomography," *Optics Express*, vol. 14, no. 8, pp. 3225–3237, 17 April 2006.

[169] C. J. Saraceno, "Mode-locked thin-disk lasers and their potential application for high-power terahertz generation," *Journal of Optics*, vol. 20, no. 4, pp. 044010–1–14, 23 March 2018.

[170] H. Kalaycioğlu, P. Elahi, Ö. Akçaalan, and F. Ö. Ilday, "High-repetition-rate ultrafast fiber lasers for material processing," *IEEE Journal of Selected Topics in Quantum Electronics*, vol. 24, no. 3, pp. 1–12, 2018.

[171] D. G. Ouzounov, I. V. Bazarov, B. Dunham, C. Sinclair, S. Zhou, and F. W. Wise, "The laser system for the ERL electron source at Cornell University," in *PAC07, Albuquerque, New Mexico, USA*, 2007.

[172] B. Ortaç, M. Plötner, T. Schreiber, J. Limpert, and A. Tünnermann, "Experimental and numerical study of pulse dynamics in positive net-cavity dispersion mode-locked Yb-doped fiber lasers," *Optics Express*, vol. 15, no. 23, pp. 15595–15602, 2007.

[173] B. Ortaç, J. Limpert, and A. Tünnermann, "High-energy femtosecond Yb-doped fiber laser operating in the anomalous dispersion regime," *Optics Letters*, vol. 32, no. 15, 2007.

[174] B. Ortaç, M. Plötner, J. Limpert, and A. Tünnermann, "Self-starting passively mode-locked chirped pulse fiber laser," *Optics Express*, vol. 15, no. 25, pp. 16794–16799, 2007.

[175] M. Baumgartl, B. Ortaç, T. Schreiber, J. Limpert, and A. Tünnermann, "Ultrashort pulse formation and evolution in mode-locked fiber lasers," *Applied Physics B*, vol. 104, no. 3, pp. 523–536, 2011.

[176] J.-B. Lecourt, C. Duterte, F. Narbonneau, D. Kinet, Y. Hernandez, and D. Giannone, "All-normal dispersion, all-fibered PM laser mode-locked by SESAM," *Optics Express*, vol. 20, no. 11, pp. 11918–11923, 2012.

[177] O. Katz, Y. Sintov, Y. Nafcha, and Y. Glick, "Passively mode-locked ytterbium fiber laser utilizing chirped-fiber-Bragg-gratings for dispersion control," *Optics Communications*, vol. 269, no. 1, pp. 156–165, 2007.

[178] K. Kieu and F. W. Wise, "All-fiber normal-dispersion femtosecond laser," *Optics Express*, vol. 16, no. 15, pp. 11453–11458, 2008.

[179] E. P. Ippen, "Principles of passive mode locking," *Applied Physics B*, vol. 58, pp. 159–170, 1994.

[180] H. W. Mocker and R. J. Collins, "Mode competition and self-locking effects in a Q-switched ruby laser," *Applied Physics Letters*, vol. 7, no. 10, pp. 270–273, 1965.

[181] E. P. Ippen, C. V. Shank, and A. Dienes, "Passive mode locking of the CW dye laser," *Applied Physics Letters*, vol. 21, no. 8, pp. 348–350, 1972.

[182] B. K. Garside and T. K. Lim, "Laser mode locking using saturable absorbers," *Journal of Applied Physics*, vol. 44, no. 5, pp. 2335–2342, 1973.

[183] T. Ennejah and R. Attia, *Current Developments in Optical Fiber Technology, Chapter 15: Mode Locked Fiber Lasers*, pp. 405–426. Intech, 2013.

[184] J. W. Haus, M. Hayduk, W. Kaechele, K. Teegarden, G. Shaulov, and G. Wicks, "A mode-locked fiber laser with a chirped grating mirror," *Optics Communications*, vol. 174, pp. 205–214, 2000.

[185] M. Zhang, L. L. Chen, C. Zhou, Y. Cai, L. Ren, and Z. G. Zhang, "Mode-locked ytterbium-doped linear-cavity fiber laser operated at low repetition rate," *Laser Physics Letters*, vol. 6, no. 9, pp. 657–660, 2009.

[186] F. Tan, H. Shi, P. Wang, J. Liu, and P. Wang, "Chirped pulse amplification of a dissipative soliton thulium-doped fiber laser," in *Proceeding of SPIE, Fiber Lasers XIII: Technology, Systems, and Applications*, vol. 9728, pp. 97280Y–1–7, 11 March 2016.

[187] F. Zou, Z. Wang, Z. Wang, Y. Bai, Q. Li, and J. Zhou, "Widely tunable all-fiber SESAM mode-locked ytterbium laser with a linear cavity," *Optics & Laser Technology*, vol. 92, pp. 133–137, 2017.

[188] K. O. Hill, F. Bilodeau, B. Malo, T. Kitagawa, S. Thériault, D. C. Johnson, J. Albert, and K. Takiguchi, "Chirped in-fiber Bragg gratings for compensation of optical-fiber dispersion," *Optics Letters*, vol. 19, no. 17, pp. 1314–1316, 1994.

[189] K.-M. Feng, J.-X. Cai, V. Grubsky, D. S. Starodubov, M. I. Hayee, S. Lee, X. Jiang, A. E. Willner, and J. Feinberg, "Dynamic dispersion compensation in a 10/Gbs optical system using a novel voltage tuned nonlinearity chirped fiber Bragg grating," *IEEE Photonics Technology Letters*, vol. 11, no. 3, pp. 373–375, 1999.

[190] S. Lee, R. Khosravani, J. Peng, V. Grubsky, D. S. Starodubov, A. E. Willner, and J. Feinberg, "Adjustable compensation of polarization mode dispersion using a high-birefringence nonlinearity chirped fiber Bragg garting," *IEEE Photonics Technology Letters*, vol. 11, no. 10, pp. 1277–1279, 1999.

[191] J.-X. Cai, K.-M. Feng, A. E. Willner, V. Grubsky, D. S. Starodubov, and J. Feinberg, "Simultaneous tunable dispersion compensation of many WDM channels using a sampled nonlinearity chirped fiber Bragg grating," *IEEE Photonics Technology Letters*, vol. 11, no. 11, pp. 1455–1457, 1999.

[192] A. O. C. Davis, P. M. Saulnier, M. Karpinski, and B. J. Smith, "Pulsed single-photon spectrometer by frequency-to-time mapping using chirped fiber Bragg gratings," *Optics Express*, vol. 25, no. 11, pp. 12804–12811, 2017.

[193] S. Korganbayev, Y. Orazayev, S. Sovetov, A. Bazyl, E. Schena, C. Massaroni, R. Gassino, A. Vallan, G. Perrone, P. Saccomandi, M. Arturo Caponero, G. Palumbo, S. Campopiano, A. Iadicicco, and D. Tosi, "Detection of thermal gradients through fiber-optic chirped fiber Bragg grating (CFBG): Medical thermal ablation scenario," *Optical Fiber Technology*, vol. 41, pp. 48–55, 2018.

[194] D. Tosi, "Review of chirped fiber Bragg grating (CFBG) fiber-optic sensors and their applications," *Sensors (Basel)*, vol. 18, no. 7, pp. 1–32, 2018.

[195] B. Ortaç, C. Lecaplain, A. Hideur, T. Schreiber, J. Limpert, and A. Tünnermann, "Passively mode-locked single-polarization microstructure fiber laser," *Optics Express*, vol. 16, no. 3, pp. 2122–8, 2008.

[196] C. Saraceno, "White paper: Pulse stretching and compressing using grating pairs," 2017.

[197] J. Carpenter, B. J. Eggleton, and J. Schröder, "110x110 optical mode transfer matrix inversion," *Optics Express*, vol. 22, no. 1, pp. 96–101, 2013.

[198] J. Carpenter, B. J. Eggleton, and J. Schröder, "First demonstration of principal modes in a multimode fibre," in *ECOC 2014, Cannes - France*, September 2014.

[199] J. Carpenter, B. J. Eggleton, and J. Schröder, "Applications of spatial light modulators for mode-division multiplexing," in *ECOC 2014, Cannes - France*, September 2014.